TURUN
YLIOPISTO
UNIVERSITY
OF TURKU

Computational Simulations of Perovskite Solar Cell Technologies under Varying Operation Conditions

Aleksi Kamppinen

TURUN YLIOPISTON JULKAISUJA – ANNALES UNIVERSITATIS TURKUENSIS
SARJA – SER. F OSA – TOM. 86 | TECHNICA – INFORMATICA | TURKU 2026

TURUN
YLIOPISTO
UNIVERSITY
OF TURKU

COMPUTATIONAL SIMULATIONS OF PEROVSKITE SOLAR CELL TECHNOLOGIES UNDER VARYING OPERATION CONDITIONS

Aleksi Kamppinen

TURUN YLIOPISTON JULKAISUJA ANNALES UNIVERSITATIS TURKUENSIS
SARJA SER. F OSA TOM. 86 | TECHNICA INFORMATICA | TURKU 2026

University of Turku

Faculty of Technology
Department of Mechanical and Materials Engineering
Materials Engineering
Doctoral Programme in Technology

Supervised by

Professor Kati Miettunen
University of Turku

Dr. Aapo Poskela
University of Turku

Reviewed by

Assoc. Professor Nicklas Anttu
Åbo Akademi University

Professor Gerrit Boschloo
Uppsala University

Opponent

Professor Wolfgang Tress
Zurich University of Applied Sciences

ISBN 978-952-02-0699-4 (PRINT)
ISBN 978-952-02-0700-7 (PDF)
ISSN 2736-9390 (Painettu/Print)
ISSN 2736-9684 (Sähköinen/Online)
Painosalama, Turku, Finland 2026

To my wife, Veera, and our children

UNIVERSITY OF TURKU
Faculty of Technology
Department of Mechanical and Materials Engineering
Materials Engineering
KAMPPINEN, ALEKSI: Computational Simulations of Perovskite Solar Cell Technologies under Varying Operation Conditions
Doctoral dissertation, 200 pp.
Doctoral Programme in Technology
May 2026

ABSTRACT

Perovskite solar cells are promising for photovoltaic light conversion to electricity with a high power conversion efficiency. The key materials, perovskites, are a large group of materials, and their properties can be tuned by altering the composition, which makes perovskites adaptable to different applications. Perovskites may be applied in single- or multi-junction cells and in different environments, such as varying outdoor conditions or indoors. The high performance in different applications and tunability of perovskites has also inspired development of other materials, which resemble perovskites. These perovskite-inspired materials further expand the material design and application alternatives. As the perovskite technologies move closer to the commercial applications, it is important to understand the interconnected effects of material properties and varying operation conditions.

This thesis studies perovskite and perovskite-inspired material absorbers in photovoltaic applications in different operation conditions, including indoor lighting and varying outdoor weather conditions. Optical, electrical, and thermal models are applied to computationally simulate the devices and the conditions. First, optical characterization and modelling are conducted to understand the optical limits for the photogeneration and radiative limit efficiency of two emerging lead-free perovskite-inspired materials under artificial indoor lighting. The results reveal a large margin between the optical limits and the experimental state of the art, which is hoped to improve in the future, for example, with insights from optoelectronic modelling enabled by the produced optical constant data. Second, parasitic heat generation and operation temperature of perovskite solar cells and panels in realistic outdoor conditions are predicted. The band gap dependence of parasitic heat generation in planar PSCs is quantified and a perovskite panel is predicted to operate in ca. $7\,^{\circ}\mathrm{C}$ lower temperature than a comparable silicon panel in reference conditions, for example. Finally, the correlated effects of layer thicknesses are analysed for structure optimization, a topic which follows throughout the thesis. In the future, the applied methods and obtained results may enable the development of perovskite-based photovoltaics for the application specific conditions.

KEYWORDS: Perovskite solar cells, perovskite-inspired materials, photovoltaics, indoor photovoltaics, computational simulation, operation conditions

TURUN YLIOPISTO
Teknillinen tiedekunta
Kone- ja materiaalitekniikan laitos
Materiaalitekniikka
KAMPPINEN, ALEKSI: Computational Simulations of Perovskite Solar Cell Technologies under Varying Operation Conditions
Väitöskirja, 200 s.
Teknologian tohtoriohjelma
Toukokuu 2026

TIIVISTELMÄ

Perovskiittiaurinkokennot ovat lupaava ryhmä uudentyyppisiä aurinkokennoja sähkön tuottamiseksi valon energiaa hyödyntämällä. Perovskiitit ovat ryhmä samankaltaisen kristallirakenteen omaavia materiaaleja, ja niiden ominaisuuksia voi muuttaa niiden kemiallista koostumusta muuttamalla, mikä tekee perovskiiteista moneen sovellukseen mukautuvia. Perovskiitteja voidaan hyödyntää yksi- tai moniliitosaurinkokennoissa ja erilaisissa ympäristöissä, kuten vaihtelevissa ulko-olosuhteissa tai sisätiloissa. Perovskiitit ovat myös inspiroineet materiaalimuunnoksia, jotka laajentavat materiaalijoukon ominaisuuksia ja sovellusjoukkoa yhä laajemmaksi. Perovskiittien siirtyessä kohti kaupallista käyttöä, on tärkeää ymmärtää materiaalien ominaisuuksien ja ympäröivien olosuhteiden yhteisvaikutukset aurinkokennojen toiminnalle.

Tässä väitöskirjassa tutkitaan perovskiitti- ja perovskiittimuunnosten hyödyntämistä aurinkokennojen valoa absorboivana materiaalina erilaisissa olosuhteissa, mukaan lukien sisäolosuhteissa ja erilaisissa ulko-olosuhteissa. Tutkimus koostuu laskennallisista simulaatioista optisia, sähköisiä ja lämpömalleja hyödyntämällä. Ensimmäisessä osajulkaisussa raportoidaan kahden sisäaurinkokennoihin lupaavan, lyijyä sisältämättömän, perovskiittimuunnoksen optiset ominaisuudet ja niihin perustuvat optiset rajat virrantuotannolle ja hyötysuhteelle. Tulokset osoittavat optisten rajojen olevan huomattavasti nykyisiä kokeellisia tuloksia korkeammat. Mitattuja kompleksiarvoisia taitekerroinspektrejä voidaan hyödyntää optoelektronisissa malleissa, joiden toivotaan auttavan kokeellisen toiminnan ymmärryksessä ja kehityksessä. Seuraavat osajulkaisut mallintavat perovskiittiaurinkokennojen ja -paneelien lämmöntuottoa ulko-olosuhteissa tuottaen kvantitaaviset ennusteet energia-aukon vaikutuksesta lämmöntuottoon ja toimintalämpötilaan. Perovskiittipaneelin toimintalämpötilan ennustetaan olevan esimerkiksi noin $7\,^{\circ}\mathrm{C}$ vertailukelpoista piipaneelia alhaisempi viiteolosuhteissa. Viimeinen osajulkaisu tarkastelee perovskiittikennon kerrosten paksuuksien korrelaatiota rakenteen optimoimiseksi. Sovellettuja metodeja ja saatuja tuloksia voidaan tulevaisuudessa hyödyntää perovskiittipohjaisten aurinkokennojen kehityksessä olosuhdekohtaisesti.

ASIASANAT: Perovskiittiaurinkokennot, perovskiittien inspiroimat materiaalit, sisäaurinkokennot, laskennallinen mallinnus, toimintaolosuhteet

Acknowledgements

This work was funded by the University of Turku Graduate School (UTUGS), Jenny and Antti Wihuri Foundation, Finnish Foundation for Technology Promotion, Lieto Savings Bank Foundation (KesPV project), and Research Council of Finland (SUBSTAINABLE project). I thank all the funders for their support of my doctoral research directly or as part of research projects.

I thank my supervisors, Prof. Kati Miettunen, Dr. Aapo Poskela (2023-), and Dr. Heikki Palonen (2022-23), for their support during the doctoral studies. Thank you, Kati, for your trust in me. Your belief in me, from early on, keeps amazing me. Thank you also for enduring my stubbornness. Aapo actually started (although not officially) supervising me already in 2018 when I entered the field of solar cell research during my bachelor's thesis. Thank you for all the help along the way, work-related and other discussions. Thank you, Heikki, for all the discussions of physics during lunches and otherwise. I enjoyed them very much. Thank you all for the comments and suggestions to improve my work.

I thank all the collaborators and co-authors of the original papers (in addition to my supervisors): Dr. Mahboubeh Hadadian, Sirius Yli-Paavola, and Julianna Varjopuro from UTU, Dr. Murthy Grandhi, Sami Toikkonen, and Prof. Paola Vivo from TAU, Juha Karhu, and Prof. Anders Lindfors from FMI (grouped by affiliation, in order of appearance in the author lists). Your contributions greatly improved the respective papers. **Publication I** would not have been possible without the collaboration with Hybrid Solar Cells group at TAU. Julianna (first author of **Publication III** !), great work!

Apart from authors of the original papers, many supported related investigations. I thank Prof. Konstantinos Daskalakis and some current and previous members of Luminous Materials and Devices group for helpful discussions and instructions on ellipsometry: Dr. Ahmed Abdelmagid, Dr. Manish Kumar, Dr. Hassan Qureshi, and Oskar Tuomi (in alphabetical order by surnames). Thanks also to Dr. Ermei Mäkilä for SEM discussions and Dr. Mikko Salomäki and Dr. Joaquin Valdez Garcia for AFM training and discussions.

Thank you, Prof. Wolfgang Tress, for acting as my opponent and for the (at this point of time) coming discussion in the defence. I look forward to it. I thank Prof. Nicklas Anttu and Prof. Gerrit Boschloo for valuable comments on my thesis manuscript, which helped me to improve the thesis and make it more complete and

precise.

I thank Solar Energy Materials and Systems (SEMS) group (previous and current members): Vidushi Aggarwal, Elena Akulenko, Väinö Anttalainen, Maryam Esmaeilzadeh, Dr. Mahboubeh Hadadian, Teemu Hynnä, Tommi Jokikyyny, Dr. Sami Jouttijärvi, Tytti Juusti, Lauri Karttunen, Anna Knol, Dr. Alicja Ławrynowicz, Prof. Kati Miettunen, Dr. Rustem Nizamov, Mikael Nyberg, Dr. Emilia Palo, Dr. Heikki Palonen, Dr. Aapo Poskela, Dr. Kimmo Pyyhtiä, Magda Szarek, Dr. Joaquin Valdez Garcia, Julianna Varjopuro, Helmi Vuorinen, Sirius Yli-Paavola and visitors. Mahboubeh, thank you for our discussions on science and literature, from the details of perovskites to the general conduct of research, as well as other aspects of life, its ups and downs. Julianna, it has been a pleasure supervising your early steps in research. I hope I have occasionally helped your work. Thank you for helping mine. Lauri, thank you for all the discussions and the (too few, that's definitely on me) sports activities. You do great work. Thank you all for the shared moments and chats.

In addition to the aforementioned Materials Engineering unit members, I have had the pleasure of discussing various scientific topics and learn from many (previous and current) researchers in the unit including, but not limited to, Dr. Ransell D'Souza, Dr. Touko Herranen, Dr. Konstantinos Konstantinou, Michail Papachatzakis, Prof. Alberto Scacchi, Dr. Olli Siltanen, Matilda Sipilä, and Prof. Milica Todorović. Also, Prof. Pekka Laukkanen and Prof. Jyrki Piilo from UTU physics, and Dr. Pascal Henkel and Dr. Emppu Salonen from Aalto physics. Some of the referred discussions are rather far from the focus of this thesis depending on the perspective. Some topic(s), on the other hand, might affect my future work more than the past (or this) work. In any case, I appreciate your time and interest, thank you. Dr. Ulriika Mattinen, special thanks for your efforts to lift up the workplace atmosphere and our discussions over a range of topics from work to (family-)life.

In spring 2024, I also had an opportunity to spend four weeks in Forschungszentrum Jülich, Helmholtz-Institute Erlangen-Nürnberg (HI ERN). Thank you Dr. Ian Marius Peters and the group, especially Dr. Mykhailo Sytnyk, Albert These, Yanxue Wang, and Zhenni Wu, for hosting me and all the friendly and professional support during the visit. Thank you Kati and Research Council of Finland (BioEST project) for making the visit possible.

I also thank my previous research group, New Energy Technologies led by Prof. Emeritus Peter Lund at Aalto University. In addition to my B.Sc. thesis, I was subsequently given a chance to work on various topics in and around energy technologies during and between semesters. I thank Dr. Kerttu Aitola (supervisor/instructor of my B.Sc. thesis), Prof. Imran Asghar, and Dr. Janne Halme for the encouragement over the years. It's always nice to see you in a conference or other occasions.

My friends from childhood and later stages of life, Martsari, KeiKa, Manaatit, Muflonit, Aalto physics, Ristin kilta, other groups and individuals, I am lucky to

know you. Thank you mum and dad, Mikko and Kristiina, kauniit kasvinkumppalini, for your support over the years. Finally, and most importantly: kiitos Veera, Nooa ja pikkuinen, for everything.

29.4.2026
Aleksi Kamppinen

Table of Contents

List of Original Publications

This dissertation is based on the following original publications, which are referred to in the text by their Roman numerals:

I **A. Kamppinen**, G.K. Grandhi, M. Hadadian, S. Toikkonen, S. Yli-Paavola, P. Vivo, K. Miettunen. Spectroscopic Ellipsometry Characterization and Radiative Limit Modeling of Bismuth-Based Perovskite-Inspired Absorbers for Indoor Photovoltaics. Advanced Optical Materials, 2026; 14 (5): e03237.

II **A. Kamppinen**, H. Palonen, K. Miettunen. Self-Heating of Planar Perovskite Solar Cells Depending on Active Material Properties. ACS Applied Energy Materials, 2024; 7 (10): 4324-4334.

III J. Varjopuro, **A. Kamppinen**, A. Poskela, J.A. Karhu, A.V. Lindfors, K. Miettunen. Computational simulation of perovskite and silicon solar panel operating temperatures in varying ambient conditions. Solar Energy Materials and Solar Cells, 2025; 290: 113657.

IV **A. Kamppinen**, K. Miettunen. Optimization of a Planar Perovskite Solar Cell Layer Thicknesses: Optical and Electrical Effects. Proceedings of the 41st European Photovoltaic Solar Energy Conference, 2024; 020081-001 - 020081-005.

Author's Contribution

Publication I

A.K., G.K.G., M.H., P.V., and K.M. designed the study. **A.K.** conducted the characterization (ex. SEM) and simulations and wrote most parts of the initial draft. G.K.G. wrote parts of the initial draft (4.1 Materials and 4.2 Fabrication of Bi-PIM Films). S.T. prepared the samples. S.Y. took the SEM images. P.V. and K.M. supervised the work. All authors participated in review and editing.

Publication II

A.K. designed the study with contributions from H.P. and K.M. **A.K.** conducted the simulations and wrote the initial draft. H.P. and K.M. supervised the work. All authors participated in review and editing.

Publication III

A.K. conceptualized the study with other authors participating in the research design. J.V. and **A.K.** wrote the analysis scripts. J.V. conducted the simulations and wrote most parts of the initial draft. **A.K.** wrote parts of the initial draft (1. Introduction together with J.V. and 2.3. Heat generation). J.A.K. provided the experimental data. **A.K.** and K.M. supervised the work. All authors participated in review and editing.

Publication IV

A.K. designed the study, conducted the simulations and wrote the initial draft. K.M. supervised the work. Both authors participated in review and editing.

Artificial intelligence (AI) tools, if any, were applied as embedded in web browsers or typesetting softwares, for example. AI tools were not used to develop research concepts, analyse data, or draw conclusions.

Other Publications by the Author

The author has also contributed to the following publications within the field of photovoltaics, which are not part of this thesis:

V **A. Kamppinen**, K. Aitola, A. Poskela, K. Miettunen, P.D. Lund. Stability of cobalt complex based dye solar cells with PEDOT and Pt catalysts and different electrolyte concentrations. Electrochimica Acta, 2020; 335: 135652.

VI M. Liu, S. Dahlström, C. Ahläng, S. Wilken, A. Degterev, A. Matuhina, M. Hadadian, M. Markkanen, K. Aitola, **A. Kamppinen**, J. Deska, O. Mangs, M. Nyman, P.D. Lund, J.-H. Smått, R. Österbacka, P. Vivo. Beyond hydrophobicity: how F4-TCNQ doping of the hole transport material improves stability of mesoporous triple-cation perovskite solar cells. Journal of Materials Chemistry A, 2022; 10 (21): 11721-11731.

VII S. Jouttijärvi, G. Lobaccaro, **A. Kamppinen**, K. Miettunen. Benefits of bifacial solar cells combined with low voltage power grids at high latitudes. Renewable and Sustainable Energy Reviews, 2022; 161: 112354.

VIII J.J. Kaschuk, Y. Al Haj, J. Valdez Garcia, **A. Kamppinen**, O.J. Rojas, T. Abitbol, K. Miettunen, J. Vapaavuori. Processing factors affecting roughness, optical and mechanical properties of nanocellulose films for optoelectronics. Carbohydrate polymers, 2024; 332: 121877.

IX A. Poskela, J. Varjopuro, T. Jokikyyny, **A. Kamppinen**, H. Palonen, K. Miettunen. Impact of Textured Surfaces and Cleaning on Solar Panel Glass Transmittance. Proceedings of the 41st European Photovoltaic Solar Energy Conference, 2024; 020152-001 - 020152-004.

X J. Varjopuro, **A. Kamppinen**, A. Poskela, A.V. Lindfors, S. Wang, S. Ranta, K. Miettunen. Evaluation of the panel temperature modeling parameters for bifacial photovoltaics with open-rack and vertical installations. Solar Energy, 2026; 311: 114529.

Symbols and Abbreviations

α	Absorption coefficient
α_{tot}	Total absorption factor
$\alpha_{\lambda<\lambda_{\mathrm{g}}}, \alpha_{\lambda\geq\lambda_{\mathrm{g}}}$	Effective spectral absorption constants above and below the band gap
β	Temperature coefficient
Δ	Phase difference
ΔE_{g}	Band gap shift
δ	Phase shift
ϵ	(Electric) permittivity, dielectric constant
ϵ_0	Vacuum permittivity
ϵ_{r}	Relative permittivity
ϵ_{s}	Surface emissivity
η_{e}	Electrical conversion factor
θ	Propagation (or incidence) angle of light
κ	Thermal conductivity
λ	Wavelength
μ	(Magnetic) permeability
μ_0	Vacuum permeability
μ_{r}	Relative permeability
$\mu_{n/p}, \mu_n, \mu_p$	Carrier mobility (ambipolar, electron, or hole)
ν	Frequency
ρ	Complex amplitude ratio of reflectance
σ	Stefan-Boltzmann constant
$\langle\sigma\rangle$	Average capture cross-section of carriers
τ	Complex amplitude ratio of transmittance
$\tau_{n/p}, \tau_n, \tau_p$	Carrier lifetime (ambipolar, electron, or hole)
χ	Electron affinity
Ψ	Amplitude ratio
ω	Angular frequency
A	Absorption
A_{cell}	Cell area (active area)
A_{s}	Spectral absorption factor

$\vec{B}$	Magnetic flux density
c_0	Speed of light in vacuum
$\vec{D}$	(Electric) displacement field
D, D_n, D_p	Diffusion coefficient (ambipolar, electron, or hole)
$D_{n,\mathrm{th}}, D_{p,\mathrm{th}}$	Thermal diffusion coefficients of electrons and holes
d	Layer thickness
$\vec{E}$	Electric field
E	Energy
$E_\mathrm{c}, E_\mathrm{v}$	Conduction and valence band energy levels
$E_{\mathrm{F}n}, E_{\mathrm{F}p}$	Quasi-Fermi levels of electrons and holes
E_g	Band gap (energy)
$E_{\mathrm{i/r/t}}$	Electric field amplitude of the incident, reflected or transmitted component
E'	Normalized electric field amplitude
e_Ω	Etendue
f	Volume fraction
$f_{n/k}$	Scaling factor of an n or k spectrum
G	Irradiance
G_ph	Photogeneration
$\vec{H}$	Magnetic field
H_conv	Convection (heat flux)
H_rad	Radiation (heat flux)
h	Planck's constant
h_c	Convection coefficient
I	Current
I_E	(Light) intensity
I_MPP	Current at MPP
I_SC,J_SC	Short circuit current (density)
Int. J_ph	Integrated photocurrent density (over a spectrum)
i	Imaginary unit
$J, \vec{J}$	Current density (scalar for circuit, vector in general)
J_n, J_p	Electron and hole current densities
$\vec{k}$	Wave vector
k_B	Boltzmann constant
L_D	Diffusion length
$\mathbf{M}_\mathrm{S}$	System matrix
$N_\mathrm{d}, N_\mathrm{a}$	Donor and acceptor density
N_t	Trap density
$\tilde{n}$	Complex index of refraction
n, k	Real and imaginary part of the complex index of refraction
$n_\mathrm{e}, p_\mathrm{h}$	Electron and hole density

n_{if}	Ideality factor
$\mathbf{P}$	Propagation matrix
P	Power
P_{in}	Input (or incident) power (of irradiance)
P_{max}	Maximum power
Q	Heat
Q_{H}	Heterostructure heating
Q_{J}	Joule heating
Q_{P}	Peltier heat
Q_{pAbs}	Parasitic absorption (heat)
Q_{R}	Recombination (heat)
Q_{T}	Thermalization
q	Elementary charge
R	Recombination
R_{rad}	Radiative recombination
$\vec{r}$	Position vector
$\mathbf{T}$	Transmission matrix
T	Temperature
t	Time
V	Voltage
V_{MPP}	Voltage at MPP
V_{OC}	Open circuit voltage
v_{th}	Thermal velocity of carriers
v_{w}	Wind speed
x, y, z	Positions along spatial dimensions
$\circ$	Degree
$\parallel$	Parallel
$\perp$	Perpendicular
1D	One-dimensional
2D	Two-dimensional
3D	Three-dimensional
AFM	Atomic force microscopy
AM1.5G	Air mass 1.5 global
amb	Ambient
CABI	Copper silver bismuth iodide ($\mathrm{Cu_2AgBiI_6}$)
CBI	Cesium bismuth iodide/bromide ($\mathrm{Cs_3Bi_2I_6Br_3}$)
EDS	Energy-dispersive X-ray spectroscopy
EMA	Effective medium approximation
EQE	External quantum efficiency

ETL	Electron transport layer
EVA	Ethylene vinyl acetate
FEM	Finite element method
FF	Fill factor
FMI	Finnish Meteorological Institute
FTO	Fluorine-doped tin oxide
g	Gap (referring to the band gap)
HTL	Hole transport layer
IPV	Indoor photovoltaic
ITO	Indium-doped tin oxide
MAPC	Maximum achievable photocurrent
MAPI	Methylammonium lead tri-iodide ($CH_3NH_3PbI_3$ or $MAPbI_3$)
MPP	Maximum power point
MSE	Mean square error
NIR	Near infrared (irradiance or photons with a wavelength beyond visible spectrum, ca. 0.8-$2.5\,\mu\mathrm{m}$)
OC	Open circuit
PCE	Power conversion efficiency
PERC	Passivated emitter and rear contact
PIM	Perovskite-inspired material
PSC	Perovskite solar cell
PV	Photovoltaic
PVK	Perovskite
ref	Reference
SC	Short circuit
SE	Spectroscopic ellipsometry
SEM	Scanning electron microscopy
SHJ	Silicon heterojunction
Spiro-OMeTAD	2,2',7,7'-Tetrakis[N,N-di(4-methoxyphenyl)amino]-9,9'-spirobifluorene
SRH	Shockley-Read-Hall (recombination)
STC	Standard testing conditions
TMM	Transfer matrix method
TOPCon	Tunnel oxide passivated contact
tot	Total
WLED	White light-emitting diode

1 Introduction

1.1 Motivation

Global energy system needs to shift from fossil fuels to carbon-free and renewable energy sources. The need is urgent because of the global warming [1], and ultimately, it is almost inevitable because of the limited resources on Earth [2]. Solar energy holds great potential to meet the need for renewable and fossil fuel free energy production. The Sun provides two to three orders of magnitude more recoverable energy on Earth than any other primary energy source in use [3]. In addition, it is the ultimate energy source on Earth in the cosmic scale.

Photovoltaic (PV) solar cells convert irradiation directly to electricity [4]. Direct electricity generation is beneficial considering the prominent role of electricity in the predicted future energy system [5]. At the moment, the global energy demand increases, and of the different forms of energy which are used, electricity demand increases the fastest (2.7% per year on average from 2010 to 2023, which is double than that of the total energy demand growth rate) [6].

Perovskite solar cells (PSCs) [7–11] are a promising group of emerging thin film solar cells. PSCs posses many desired properties including high efficiency, tunability and potential for low-cost manufacturing [10–12]. In addition to the PSCs being interesting because of their technological and potentially commercial applications, the key materials, perovskites, offer an intriguing scientific challenge with their versatility and complexity [12–15].

Currently, most of the manufactured PV panels consist of monocrystalline silicon solar cells [16]. Power conversion efficiency (PCE) of silicon solar panels has increased driven by, for example, innovations in the cell architecture, including passivated emitter and rear contact (PERC) [17; 18], tunnel oxide passivated contact (TOPCon) [19; 20], and silicon heterojunction (SHJ) [21; 22] technologies. The price of silicon cells has also decreased especially during the last decade [23], which has together with the technological development made the solar PV a commercially competitive option for electricity generation [24]. Despite the remarkable development of silicon solar panels, the efficiency development will saturate due to the theoretical limit of single junction solar cells [25; 26].

There exists different applications of PV, in addition to the most common rooftop or field installations of the traditional PV panels. Colourful, flexible, and/or lightweight solar cells are interesting for the integration of PVs into buildings [27–29]

or vehicles [30–32], for example. Solar cells can also power various devices in very different environments, such as satellites in space [33; 34] or small home appliances indoors [35; 36].

Both aspects, that is, the saturation of silicon solar cell PCE and the different applications, suggest research on new cell technologies and materials. New materials provide alternatives and may also allow entirely new functionalities and applications. For example, different thin film technologies enable flexible [37] and colourful options [32; 38; 39]. Multi-junction solar cells make possible to surpass the theoretical limit of an arbitrary single-junction cell by combining several absorber materials with suitable band gaps [40]. Overall, materials are at the heart of technology innovations because the properties of the applied materials fundamentally define the performance of any device.

This thesis focuses on the computational modelling and simulations of PSC technologies. Computational modelling is a powerful tool to support experiments because it works as a link between the theory and observations. Modelling improves the understanding of experimental observations by suggesting and revealing correlations and causalities between the constituents and results of experiments. Further, simulations enable making predictions on yet unrealized experiments. Models can also be used to optimize devices of interest.

1.2 Objectives and Scope

The conventional application of solar cells is to harvest the sunlight to produce electricity. Interestingly, ambient lighting provides an alternative source of energy to be utilized by photovoltaics [36; 41–44]. The primary objective of indoor lighting certainly is to illuminate a space for work, convenience, or otherwise. However, indoor photovoltaics (IPVs) enable to improve the energy efficiency of buildings by ”recycling” the energy, which is applied for lighting, back into use. Many small appliances could be powered by IPVs from their power requirement point of view [35; 41]. IPVs may also reduce the need for electricity transmission and storage because they facilitate the production of electricity on the device that consumes it.

Ambient lighting is a rather different radiation source compared with the solar irradiation. The radiation spectrum is narrower than that of the solar spectrum. A typical white light-emitting diode (WLED) spectrum spans over a wavelength range of $400\text{-}800\,\mathrm{nm}$ whereas solar spectrum continues well beyond $1\,\mu\mathrm{m}$ [35; 45]. As a consequence, a wider band gap compared with the typical solar cell absorbers is preferred for indoor conditions [42; 45; 46]. The narrower spectrum also means much higher theoretical PCE limits than the Shockley–Queisser limit under the solar spectrum [36]. Promising results for IPV applications have been obtained with emerging technologies, including organic photovoltaics [47], dye-sensitized solar cells [48], and perovskite solar cells [36; 49]. Notably, PSCs have demonstrated a PCE over

40% under indoor illumination [49].

Despite the outstanding record efficiency of perovskite IPVs, the best efficiencies have been obtained with lead-based perovskites. The lead toxicity continues to question the real sustainability of PSCs. Bismuth provides a less toxic alternative compared with lead [50], and Bi-based perovskite-inspired material (PIM) absorbers have demonstrated interesting potential in IPV applications.

Publication I characterizes and models two promising Bi-based PIMs, namely Cu_2AgBiI_6 (CABI) and $Cs_3Bi_2I_6Br_3$ (CBI), for IPV applications. The optical constant spectra of CABI and CBI, measured by spectroscopic ellipsometry (SE), are presented. The measured data enable the detailed optical modelling of solar cells consisting of these Bi-based PIM absorbers to study their optical limits of photogeneration and PCE at the radiative limit. The obtained results motivate efforts to improve the charge extraction, which was identified as the limiting factor for improved operation.

In addition to the efficiency and power production modelling, which were conducted in the thesis, one research interest was the temperature of PSCs under varying outdoor operation conditions. On the one hand, temperature affects the efficiency and stability of PSCs (all PV, in general), and high temperature is detrimental from both aspects [51–55]. On the other hand, heat generation within a cell is unavoidable to a certain degree, that is, it cannot be avoided entirely: various loss mechanisms convert the absorbed energy to heat [56–59]. Therefore, the cell itself produces heat during the operation, which results in an increased operation temperature. Accurate estimation of the operation temperature and the effect of the operation temperature on the cell performance enable more accurate power production predictions, as higlighted in the literature [60; 61].

Heat generation mechanisms of PSCs are presented in the literature [56–59]. So is the general dependency of heat generation on the band gap [62]. Some outdoor measurements have also been already reported [60; 63]. **Publication II** provides quantitative analysis on the effects of absorber properties on the heat generation and operation temperature of planar PSCs with strictly defined and realistic material properties. The studied absorber properties include the band gap, diffusion length, and layer thickness of the perovskite absorber. The results show that especially the band gap affects the heat generation and operation temperature of the ”optimized” PSCs. Quantitative predictions with realistic material properties are provided based on opto-electro-thermal modelling. The diffusion length and layer thickness, on the other hand, affect the device optimization: diffusion length determines which layer thickness should be applied to optimize the power production. Further, band gap also affects the temperature coefficients, that is, the dependence of PCE and other parameters on the temperature.

Publication III continues the thermal modelling of PSCs by comparing the operation temperatures of a typical band gap (ca. 1.6 eV) perovskite panel with those of a

comparable (by panel geometry and reference PCE) silicon panel in varying weather conditions. Operation temperature of Si-panels is extensively covered, although constantly developed, in the literature [64] due to its importance for the power production prediction and the related effects on the economical estimation of PV systems. From a solar system engineering point of view, the application of semi-empirical panel temperature models is a common practice [65–71]. These models predict the operation temperature based on weather input parameters and empirical model parameters, which, in general, are system specific [65; 72]. **Publication III** predicts the first set of perovskite-specific panel temperature model parameters for common panel temperature models.

Finally, **Publication IV** considers the structure optimization of PSCs. There are different PSC device architectures [73], which include, for example, mesoporous and planar structures, so-called regular and inverted configurations, and some more complex suggestions, such as graded heterojunction [74] and localized [75] or point contacts [76]. Among the different architectures, planar structure has been a common choice due to the high efficiency and commercial potential that the structure provides. **Publication IV** studies the correlated effects of the thicknesses of different layers in a planar PSC with the regular configuration and discusses the generalization of the results to the inverted configuration.

Thickness optimization of the absorber layer is an important and a common practice for PSCs and other solar cells, especially thin film solar cells. The aim is to maximize PCE by maximizing two separate factors: absorption induced photogeneration on the one hand and charge extraction on the other hand. Typically, the effect of the absorber thickness on the two factors is opposite. Absorption increases while charge extraction decreases due to increasing recombination with the thicker layer.

The focus of the **Publication IV** is on the correlation between the thicknesses of different layers, whose individual effects on device operation are rather well-known as described above for the absorber. The optically optimal layer thicknesses have been noticed to depend on each other [77]. **Publication IV** extends the consideration to the electrical effects in addition to the optical ones.

The overarching objective of the thesis was to better understand different PSC technologies in varying realistic operation conditions by computational device simulations. Each article focused on a related topic with a specific research question:

I What are the optical performance limits of the studied bismuth-based absorbers under indoor illumination based on measured optical properties?

II How do the absorber properties affect the parasitic heat generation and the operation temperature of planar PSCs?

III How does the operation temperature of a perovskite solar panel compare to that of a comparable silicon panel in varying outdoor conditions?

IV What are the optimal layer thicknesses of different PSC materials in a planar device configuration and do they depend on each other?

1.3 Structure

Chapter 2 introduces the theoretical background for the considered topics and the computational methods, which were applied to study them. The few experimental methods that were applied are briefly described in Chapter 3. Chapters 4-6 present the obtained results of the original publications, included in the thesis. These chapters also discuss some strengths and weaknesses of the publications, and suggest further research in the specific topics. Chapter 7 concludes the thesis with a wider perspective.

2 Theoretical Background and Computational Methods

2.1 Basics of Photovoltaics

Photovoltaic solar cells are devices which convert light to electricity. Three steps are necessary in every solar cell regardless of the specific type of cell: 1. light absorption, 2. charge separation, and 3. connection to an external circuit (see Figure 1 for an illustration). Light excites electrons in the active material. Positively charged quasi-particles, called holes, are simultaneously created. The creation of electron-hole pairs is commonly known as photogeneration. The generated electrons and holes need to be spatially separated to create voltage difference between (at least) two areas. When the cell is connected to an external circuit by electrical contacts at the two areas, it can drive current in the circuit and make useful work.

The current, which a cell is able to produce into an external circuit, depends on the load, that is, the voltage bias. The maximum produced current is achieved when the cell is in short circuit. However, the produced power ($P = VI$, where V is the voltage and I is the current) is zero if the applied voltage is zero. When the load increases, the current decreases until it does not flow any more when the cell is in the open circuit. In general, the current-voltage (*IV*) curve describes the current as a function of the (arbitrary) applied voltage bias, see Figure 2 for an example.

Typical performance metrics, sometimes called *IV* parameters, include short cir-

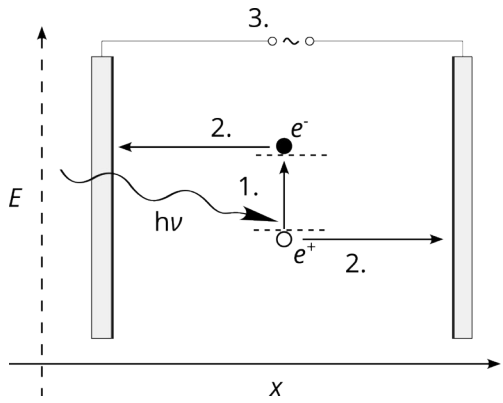

Figure 1. An illustration of general operation steps in a PV solar cell.

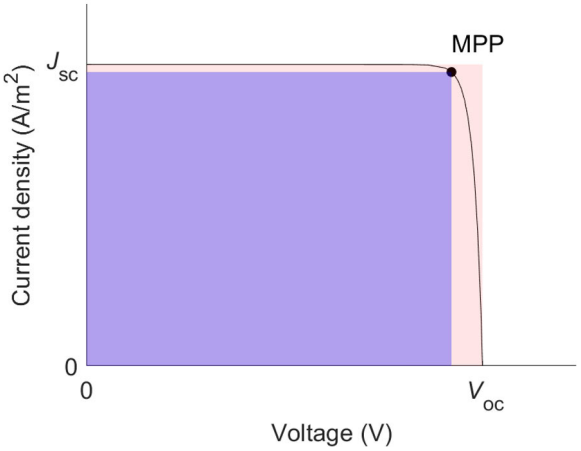

Figure 2. An illustration of a JV curve.

cuit current (I_{SC}), open circuit voltage (V_{OC}), fill factor (FF), maximum power point (MPP), and power conversion efficiency. These values can be extracted from the *IV* curve (Figure 2). Instead of I_{SC}, short circuit current density ($J_{\mathrm{SC}} = I_{\mathrm{SC}}/A_{\mathrm{cell}}$) is frequently applied because, in an ideal case, the current scales in proportion to the cell area (A_{cell}), which makes J_{SC} more comparable than I_{SC} between cells of different sizes. In general, the theoretical limits of J_{SC} and V_{OC} depend on the active material properties, and one typically decreases if the other increases when the change relates to a change of active material, which needs to be considered if comparing different cell types. MPP is the point where the maximum power (P_{max}) is produced. FF describes the ratio between $P_{\mathrm{max}} = I_{\mathrm{MPP}}V_{\mathrm{MPP}}$ and the theoretical maximum power $I_{\mathrm{SC}}V_{\mathrm{OC}}$, which are illustrated in Figure 2 as coloured areas. PCE is the ratio between P_{max} and the input power of the irradiance $P_{\mathrm{in}} = GA_{\mathrm{cell}}$, where G is the total irradiance.

Solar cells are typically characterized under standard testing conditions (STC), which refer to the cell temperature of $25°\mathrm{C}$ and irradiance of $1000\,\mathrm{W/m^2}$ with an air mass (AM) 1.5 solar spectrum (see Figure 3a) [78]. Air mass refers to the propagation length of light through the atmosphere. The actual air mass depends on the solar elevation angle with respect to the ground surface, and in general, it affects both the spectral shape and intensity of irradiance. STC characterization is beneficial for the comparability of results between different PV devices. However, solar cells are subject to varying ambient conditions in the outdoor operation. In addition, there are different applications of solar cells, for example, indoor photovoltaics (IPVs) powering small devices indoors, which is a very different environment compared with STC or the typical outdoor operation under sunlight (for example, due to the different irradiance, see Figure 3b). This thesis mainly focuses on simulating solar cells in

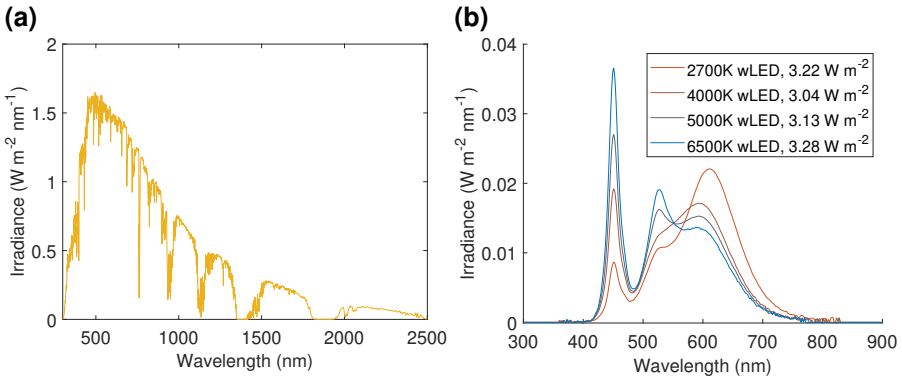

Figure 3. Irradiance spectra. (a) Solar spectrum (AM1.5G) and (b) indoor WLED spectra of constant 1000 lx illuminance and varying colour temperatures (total irradiance levels are given in the legend). Adapted from **Publication I** under CC-BY 4.0 licence.

conditions other than the STC, that is, realistic indoor or outdoor conditions.

Individual cells may also be (and for commercial products, they are) connected in series and in parallel to construct solar panels (or solar modules). When connecting cells in series, the output voltage of the string of cells increases, and when connecting cells or strings of cells in parallel, the output current increases as stated by the Kirchhoff's laws. However, individual cells instead of panels are mainly considered in this thesis because the focus is on the cell materials, especially the absorber, and their properties.

2.2 Perovskite Solar Cells

Perovskite solar cells are photovoltaics with a perovskite (PVK) as the light absorbing material (or absorber for short). Perovskites are a group of materials which share the ABX_3 structure of the first discovered perovskite —calcium titanate ($CaTiO_3$), see Figure 4. Within the ABX_3 structure, perovskites adopt different crystal structures (lattice systems), such as cubic, tetragonal, or orthorhombic. The exact crystal structure depends on internal and external factors, for example, the composition [79; 80] and temperature [80–82].

Perovskites vary in composition, that is, they can be composed of different elements. By varying the composition, material properties can be altered [86]. The possibility to tune the properties makes perovskites a versatile group of materials, and they can be designed and applied for many applications, including solar cells [87] but also light emitting diodes [88] and memristors [89], for example. Not all perovskites are even suitable for solar cells, but the focus of this thesis is on the solar application. Therefore, the term 'perovskite' is hereafter used to describe the subset

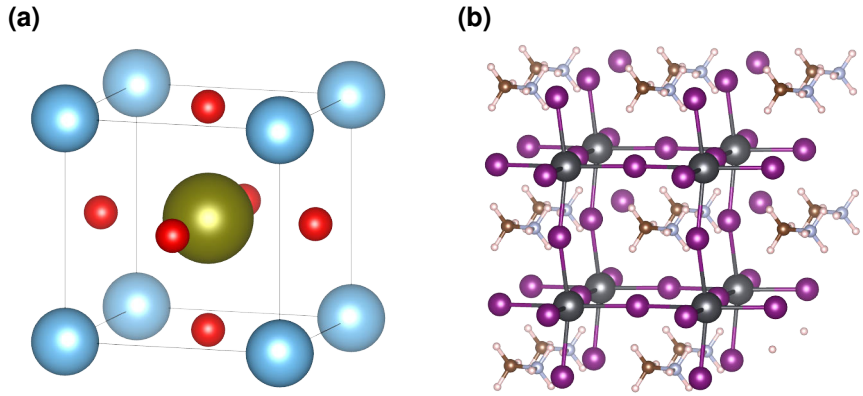

Figure 4. Perovskite crystal structure. (a) Illustration of a cubic unit cell of perovskite ABX_3 structure based on $CaTiO_3$ [83]. (b) Illustration of MAPI crystal structure: a $(2 \times 2 \times 2)$ supercell of MAPI based on a computationally optimized unit cell (crystallographic information file obtained under GPL-2.0 licence [84]). Drawings produced by VESTA [85].

of perovskites which are applied in solar cells or show promise for the PV application otherwise.

The arguably most commonly known perovskite in solar cells is methylammonium lead tri-iodide ($CH_3NH_3PbI_3$, MAPI). It was the first perovskite to provide high power conversion efficiency [7], and it has been broadly studied since. Nowadays, state of the art efficiency and stability are typically obtained with formamidinium (FA) and/or mixed cation based perovskites [10; 90].

In general, perovskites are semiconductors with a small exciton binding energy, high absorption coefficient, and (relatively) long diffusion length [10]. Small exciton binding energy means that the transport of the excited charge carriers occurs in the conduction band (valence band) of a semiconductor by free-moving electrons (holes) [91], as opposed to excitons, that is, spatially localized states where the excited carriers are bound to each other. High absorption coefficient enables a thin layer (a few hundred nanometres in the order of magnitude in the case of perovskites) to absorb nearly all light penetrating into the material. In addition, the long diffusion length relates to the fact that the excited carriers may travel distances longer than the required film thickness before being recombined. The diffusion length depends on the density of trap states, which is also affected by extensive properties, for example, the grain size in a polycrystalline film in addition to the intensive material properties. Therefore, the diffusion length is not a material property in the same sense as, for example, the binding energy and absorption coefficient. Monocrystalline (or single-crystal) perovskites can also be fabricated, but polycrystalline thin films are typically applied in practice.

PSCs are heterojunction solar cells, which means that the charge separation is

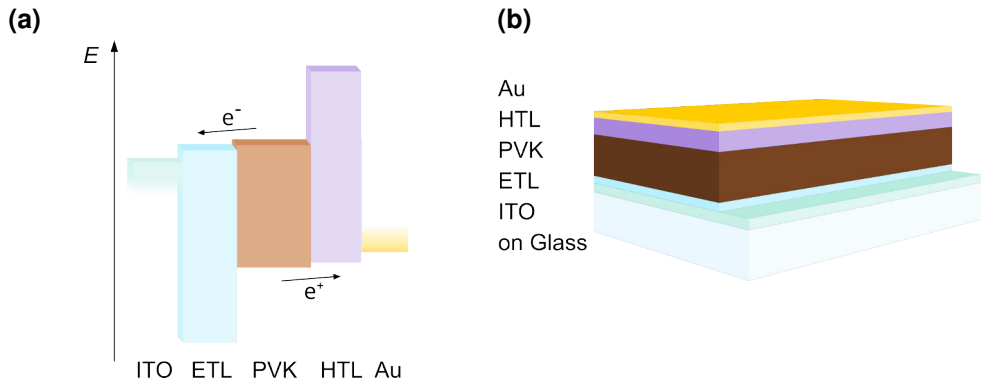

Figure 5. Example of a perovskite solar cell. (a) Energy level diagram. (b) Device structure. Figure is not to scale. Adapted from **Publication II** under CC-BY 4.0 licence.

realized by adding specific layers on top of and below the absorber. These layers are called electron and hole transport layers (ETL and HTL, respectively), and the purpose is to allow (or block) electron and hole currents into different directions by applying materials with suitable energy levels, as illustrated in Figure 5a. A transparent conducting oxide, such as indium-doped tin oxide (ITO) or fluorine-doped tin oxide (FTO), coating on glass or another substrate on the front side and a metallic back electrode, for example, gold, are applied for the external circuit connection. One typical device structure is presented in Figure 5b.

Heterojunction structure is a modest difference to silicon solar cells which rely on differently doped regions and p-n junction to separate the charges. Otherwise, the operation principle of PSCs is rather similar to that of the silicon cells and other more traditional PVs instead of, for example, dye solar cells despite the history of the technology [7; 9]. However, perovskites as materials possess some rather distinctive features compared with silicon and other PV semiconductors. These features include, for example, dynamic local structure, molecules within the lattice, ion mobility, defect tolerance, and band gap temperature dependence.

As so often in nature, many of the material properties arise from the (micro-) structure itself (the ABX_3 crystal structure in the case of perovskites). Octahedral tilting has been known to enable different crystal symmetries, phase transitions and polarizability already long before the study of perovskites in solar cells [92]. Further, perovskites are ionic crystals. The A-site cation does not form covalent bonds with the octahedral BX_6 chains [93]. Organic molecules can easily rotate within the lattice [93; 94], which results in the possibility of local rotational (dis)order and polarizability [94; 95]. On the other hand, the dynamic local order of not just the molecules, but the PbX_6 octahedra [96], has been reported to affect macroscopic properties [97; 98]. In contrast, silicon is a monatomic crystal, which forms four covalent bonds with neighbouring Si atoms in the diamond lattice.

In addition to the molecular and octahedral rotations at the lattice sites and charge transport over the device, ions are also moving in perovskites [99]. Perovskites are electronic-ionic conductors [100–102]. Mobile ions (typically halide vacancies [100; 101]) move across the perovskite layer under voltage bias, accumulate at the interfaces and screen the built-in field in the perovskite layer. Ion migration affects both the short-term and long-term operation of PSCs [103]. For example, ion migration causes hysteresis (although ion migration occurs in devices with small hysteresis as well [104]) and relates to the device degradation [103; 105].

Considering the ion migration, perovskites have fortunately been found to be (electronically) defect tolerant [106; 107]. Electronic defect tolerance refers here to the fact that point defects (ion vacancies or interstitials) tend to induce states within or close to the valence or conduction band (so-called shallow trap states), instead of deep trap states, which induce nonradiative recombination [106]. Such defect tolerance is rare. For example, metal impurity concentration in crystalline silicon cells should be less than $10^{14}\,\mathrm{cm}^{-3}$ (depending on the impurity atom) for high efficiency (ca. 20%) [108; 109]. That is, purity in Si cells needs to be in the order of one per billion impurity atoms whereas even macroscopic changes in I/Pb ratio seems to preserve the electronic structure of MAPI [107]. The high open circuit voltages of PSCs and relatively low trap densities in polycrystalline perovskite films [110] despite solution processing provide further phenomenological evidence for the defect tolerance. Indeed, defect tolerance is one of the main factors explaining the high efficiency of PSCs.

Related to the PV operation in varying temperatures, one unique property of perovskites compared with other PV semiconductors is the temperature dependence of the band gap. While the band gap of other PV semiconductors decreases with the increasing temperature, the band gaps of perovskites tend to increase with the temperature [53]. The unusual band gap temperature dependence is based on the large temperature coefficient of lattice expansion, which overcomes the counteracting electron-phonon coupling component in perovskites unlike in most semiconductors [111]. The positive temperature coefficient of the band gap contributes to the lower temperature coefficients of V_{OC} and PCE reported for PSCs despite the opposing reductions of the photogeneration and current production in elevated operation temperatures.

2.2.1 Perovskite inspired materials

Perovskites are a large group of materials, as mentioned. In addition to the typical lead-halide perovskites (LHPs), there are other subgroups of perovskites, such as Sn-based, Ge-based, and chalcogenide perovskites, which are interesting for solar applications [112]. Sn- and Ge-based PVKs share many structural properties with LHPs owing to the same number of valence electrons in Pb, Sn, and Ge atoms (all

belong to the carbon group of the periodic table). As the name suggests, chalcogenide perovskites differ from LHPs by the more negative X-site anion (-2 charge of chalcogens versus -1 of halides), which also enables larger oxidation numbers in B-site cations. However, all the mentioned are (ABX_3) perovskites.

Inspired by the material properties and motivated by the remaining issues of perovskites, namely stability and lead-toxicity (in the case of LHPs), other resembling (that is, perovskite-inspired) materials have been studied [112]. These include, for example, double perovskites ($A_2B^{'}B^{"}X_6$), $A_3B_2X_9$ and ABZ_2 materials. Despite some similarities, PIMs are not a homogeneous group of materials by any specific property. Structures vary from subgroup to another and to some extent even between the individual materials of a specific subgroup. Different PIMs form, for example, layered and low dimensional (0D, 1D, 2D) structures in addition to the "standard" 3D. Besides the structural dimensionality, also electronic dimensionality varies and is significant for the operation of PIMs [113]. Altogether, wide ranges of different electronic properties, which affect the performance in PV applications, such as wide ranges of band gaps and charge carrier mobilities, have been observed for different PIMs. Compared to LHPs, some PIMs tend to possess larger band gaps and/or may suffer from lower mobilities. For example, layered and low dimensional structures may cause low and/or anisotropic mobility. One factor affecting low mobility is the exciton binding energy, which tend to be larger in low-dimensional perovskites and PIMs compared with LHPs. Experimentally, there are differences in preparation techniques due to the differences between the various materials. Some (computationally and/or theoretically) promising PIMs face challenges in experimental realization, that is, processing and/or fabrication of high quality films, for example.

2.3 Optics

Considering the objective of solar cells, to convert light to electricity, light and its interaction with materials are of interest. At least two aspects need to be considered, when modelling light in the context of solar cells: 1) how light travels in a medium, including how it is absorbed, that is, attenuation of light intensity due to conversion to another form of energy and 2) what happens at interfaces when light is moving from a material to another.

In classical physics, light is considered a propagating electromagnetic wave. As such, light is a fundamental property of the classical electromagnetism—the wave equation directly emerges from the Maxwell's equations. Therefore, the general rules of electric and magnetic fields hold for light. For example, the continuity equations [114] state that (for negligible surface charge density and current)

$$\vec{E}_{\parallel,1} = \vec{E}_{\parallel,2}, \vec{H}_{\parallel,1} = \vec{H}_{\parallel,2} \tag{1}$$

$$\vec{D}_{\perp,1} = \vec{D}_{\perp,2}, \vec{B}_{\perp,1} = \vec{B}_{\perp,2}, \tag{2}$$

where $\vec{E}$ is the electric field, $\vec{H}$ is the magnetic field, $\vec{D} = \epsilon\vec{E}$ (assuming an isotropic medium, that is, the permittivity is a scalar number $\overline{\overline{\epsilon}} = \epsilon$) is the (electric) displacement field, $\vec{B} = \mu\vec{H}$ (similarly assume the permeability $\overline{\overline{\mu}} = \mu$) is the magnetic flux density, $\parallel$ and $\perp$ mark the parallel and perpendicular components of a field in reference to an interface, and 1 and 2 mark the media before and after the interface, respectively. In addition to the isotropic media, local and time-harmonic material response is assumed. So, the parallel components of $\vec{E}$ and $\vec{H}$ and the perpendicular components of $\vec{D}$ and $\vec{B}$ are continuous across any interface between two media.

From the continuity equations, one can derive other useful equations, such as the Snell's law, which describes the refraction of light that transmits an interface [114]. Other highly useful formula, namely Fresnel equations, arise as well [114]

$$\tau_\perp = \frac{E_\mathrm{t}}{E_\mathrm{i}} = \frac{2\tilde{n}_1\cos(\theta_\mathrm{i})}{\tilde{n}_1\cos(\theta_\mathrm{i}) + \tilde{n}_2\cos(\theta_\mathrm{t})} \tag{3}$$

$$\rho_\perp = \frac{E_\mathrm{r}}{E_\mathrm{i}} = \frac{\tilde{n}_1\cos(\theta_\mathrm{i}) - \tilde{n}_2\cos(\theta_\mathrm{t})}{\tilde{n}_1\cos(\theta_\mathrm{i}) + \tilde{n}_2\cos(\theta_\mathrm{t})} \tag{4}$$

$$\tau_\parallel = \frac{E_\mathrm{t}}{E_\mathrm{i}} = \frac{2\tilde{n}_1\cos(\theta_\mathrm{i})}{\tilde{n}_1\cos(\theta_\mathrm{t}) + \tilde{n}_2\cos(\theta_\mathrm{i})} \tag{5}$$

$$\rho_\parallel = \frac{E_\mathrm{r}}{E_\mathrm{i}} = \frac{\tilde{n}_1\cos(\theta_\mathrm{t}) - \tilde{n}_2\cos(\theta_\mathrm{i})}{\tilde{n}_1\cos(\theta_\mathrm{t}) + \tilde{n}_2\cos(\theta_\mathrm{i})}, \tag{6}$$

where τ and ρ are the complex amplitude ratios of transmittance and reflectance, E_i, E_r and E_t are the amplitudes of the incident, reflected and transmitted electric fields, θ_x (x=i,r,t) are the angles of propagation with respect to the surface normal, respectively, and $\tilde{n}_1$ and $\tilde{n}_2$ are the complex index of refractions of the two media. Fresnel equations thus describe the behaviour of light at material boundaries, which is needed for modelling solar cells because all solar cells contain material boundaries and/or interfaces.

On the other hand, light intensity attenuates when travelling in an absorbing medium. Absorption (A) is proportional to the light intensity ($I_E \propto |\vec{E}|^2$) and to the absorption coefficient ($\alpha(\lambda)$), which describes how effectively a material absorbs the light of a specific wavelength (λ, or a frequency ν the two being interconvertible),

$$A(\vec{r},\lambda) = dI_E(\vec{r},\lambda) = -\alpha(\lambda)I_E(\vec{r},\lambda), \tag{7}$$

where $\vec{r}$ is the position vector, leading to the Beer-Lambert law by integration [115]

$$I_E(z,\lambda) = I_{E0}(\lambda)e^{-\alpha(\lambda)z}, \tag{8}$$

where $I_{E0}(\lambda) = I_E(z=0,\lambda)$ is the initial intensity and z is the depth in the material.

Most of the underlaying physics presented here is not unique for the plane wave solution of the wave equation which was applied here

$$\vec{E} = \vec{E}_0 e^{\mathrm{i}(\vec{k}\cdot\vec{r}-\omega t)}, \tag{9}$$

where $|\vec{E}_0|$ is the amplitude, i is the imaginary unit, $\vec{k}$ is the wave vector, $\omega = 2\pi\nu$ is the angular frequency, and t is time. In any case, the plane wave is a good choice for many situations and applications, including solar cells. It means that light is considered as a wavefront propagating into one direction, which is a good approximation when the modelled object is far from the radiation source.

In addition to the general rules and properties of light itself, material properties affect the interaction of light with matter. The key optical property, which describes the light-matter interaction, is the complex index of refraction

$$\tilde{n} = n - \mathrm{i}k, \tag{10}$$

where n and k are the real and imaginary part of $\tilde{n}$, respectively. The real part (n) is commonly referred to as the refractive index, and it typically determines the refraction because it is usually much larger than k. However, $\tilde{n}$ is the "correct" index of refraction, and k affects (and can even dominate) refraction and reflection of some materials with large k, like many metals. Importantly for all materials, k describes absorption, and it is interconvertible with α:

$$\alpha = \frac{4\pi k}{\lambda}. \tag{11}$$

$\tilde{n}$ also relates to ϵ:

$$\tilde{n} = \sqrt{\epsilon_\mathrm{r}\mu_\mathrm{r}}, \tag{12}$$

where $\epsilon_\mathrm{r} = \epsilon/\epsilon_0$ and $\mu_\mathrm{r} = \mu/\mu_0$ are the relative permittivity and permeability. Typically, $\mu_\mathrm{r} \approx 1$ at optical frequencies. Thus, $\tilde{n}$ and $\epsilon = \epsilon_1 + \mathrm{i}\epsilon_2$ carry the same information, and the term, optical constants, is frequently applied to refer to either or both n, k and ϵ_1, ϵ_2.

2.3.1 Transfer Matrix Method

Transfer matrix method (TMM) [114; 116–119] is a computationally efficient method to solve the reflection and transmission of a multilayer structure. TMM also provides a way to calculate the local optical electric field within the layer stack, which is very useful for modelling solar cells. The method assumes a plane wave solution of Maxwell's equations and solves the optical electric field at different points of a one-dimensional (1D) structure, like illustrated in Figure 6.

TMM consists of a product of matrices of two types, called a transmission matrix ($\mathbf{T}$) and a propagation matrix ($\mathbf{P}$). $\mathbf{T}$ describes the reflection and transmittance of light at an interface and $\mathbf{P}$ describes the propagation of light within a layer. In general, a forward propagating field component after an interface (for example, $E_{\mathrm{j,d}}$ in Figure 6) is a sum of the transmitted component of the forward propagating field

before the interface ($E_{\mathrm{j,a}}$) and the reflected component of a back propagating component ($E_{\mathrm{j,c}}$) [116], which results in a scattering matrix equation

$$\begin{bmatrix} E_{\mathrm{j,d}} \\ E_{\mathrm{j,b}} \end{bmatrix} = \begin{bmatrix} \tau_{\mathrm{j-1,j}} & \rho_{j,j-1} \\ \rho_{j-1,j} & \tau_{\mathrm{j,j-1}} \end{bmatrix} \begin{bmatrix} E_{\mathrm{j,a}} \\ E_{\mathrm{j,c}} \end{bmatrix}, \tag{13}$$

where $\tau_{j-1,j}$ and $\rho_{j-1,j}$ are the complex transmittance and reflectance coefficients between adjacent layers $j-1$ and j, given by the Fresnel equations (3)-(6). The symmetry relations of the Fresnel coefficients [120]

$$\rho_{j-1,j} = -\rho_{j,j-1} \tag{14}$$

$$\tau_{j-1,j}\tau_{j,j-1} - \rho_{j-1,j}\rho_{j-1,j} = 1 \tag{15}$$

allow to formulate $\mathbf{T}$ so that the optical electric fields on one side can be calculated based on those on the other side [116; 117]

$$\begin{bmatrix} E_{\mathrm{j,a}} \\ E_{\mathrm{j,b}} \end{bmatrix} = \mathbf{T} \begin{bmatrix} E_{\mathrm{j,d}} \\ E_{\mathrm{j,c}} \end{bmatrix}, \tag{16}$$

$$\mathbf{T} = \frac{1}{\tau_{j-1,j}} \begin{bmatrix} 1 & \rho_{j-1,j} \\ \rho_{j-1,j} & 1 \end{bmatrix}. \tag{17}$$

Propagation of light involves a phase shift and potential attenuation in an absorbing medium, and it is defined by [117]

$$E_{\mathrm{j,a}} = E_{\mathrm{j-1,d}}\, e^{-i\delta_j}, \tag{18}$$

where $\delta_j = 2\pi\tilde{n}_j d_j/\lambda$ and d_j is the thickness of layer j (and similarly for back propagation). Propagation matrix is also formulated to couple electric fields at different

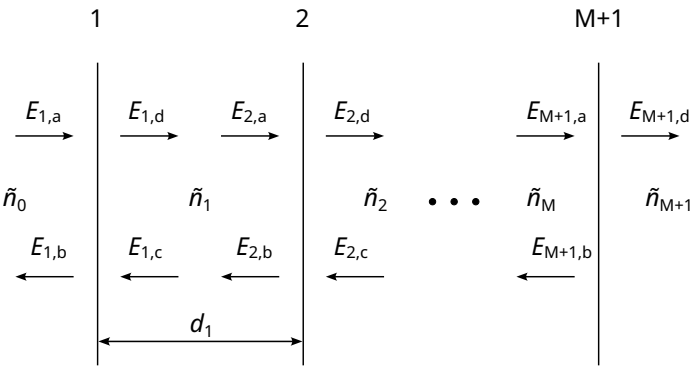

Figure 6. Illustration of a multilayer structure of M layers and the propagation of optical electric field with reflections within the multilayer stack.

interfaces [116; 117]

$$\begin{bmatrix} E_{\mathrm{j,d}} \\ E_{\mathrm{j,c}} \end{bmatrix} = \mathbf{P} \begin{bmatrix} E_{\mathrm{j+1,a}} \\ E_{\mathrm{j+1,b}} \end{bmatrix}, \tag{19}$$

$$\mathbf{P} = \begin{bmatrix} e^{i\delta_j} & 0 \\ 0 & e^{-i\delta_j} \end{bmatrix}. \tag{20}$$

One transmission matrix for each interface and one propagation matrix for each layer are formed and the matrix multiplication of all these matrices $\mathbf{T}_1\mathbf{P}_1\mathbf{T}_2...\mathbf{P}_{\mathrm{M}}\mathbf{T}_{\mathrm{M+1}}$ provides the result for the whole stack of M layers [116; 117].

TMM inherently considers light as coherent, so multiple reflections within the structure are accounted for automatically. On the other hand, the layers should be thin (relative to the coherence length of light), smooth and homogeneous for the method to be accurate. Scattering and thick layers cause visibility (a metric for light coherence) to decrease. However, there are methods to adjust TMM for partially coherent or incoherent light [117; 119; 121].

Here, the (partial) coherence was considered by introducing three different equidistant phase-shifts (0, $2\pi/3$, and $4\pi/3$) in δ_j for each "incoherent layer" and averaging over the solutions of different phase-shifts [119]. Partial coherence could be considered by giving more weight to the solution without artificial phase-shift (that, the phase-shift of 0). Equidistant, instead of random, phase-shifts have been shown computationally more efficient [119].

In practice, a modification of TMM was applied [119]. Instead of many 2×2 matrices, the equations were gathered in one large (system or stack) matrix $\mathbf{M}_{\mathrm{S}}$ combining the set of linear equations

$$\begin{cases} E_{j,a} = e^{-i\delta_{j-1}} E_{j-1,d} \\ E_{j,b} = \dfrac{1}{\tau_{j-1,j}} (E_{j,c} + \rho_{j-1,j} E_{j,d}) \\ E_{j,c} = e^{-i\delta_j} E_{j+1,b} \\ E_{j,d} = \tau_{j-1,j} E_{j,a} - \rho_{j-1,j} E_{j,c} \end{cases}, \tag{21}$$

and thus describing all the relationships between the forward and backward propagating fields in the multilayer structure at once. Considering boundaries, $E_{1,a} = E_{\mathrm{in}}$ because $E_{1,a}$ represents the incident light, and $E_{M+1,c} = 0$ because there is no back side illumination. Solving the matrix equation $\mathbf{M}_{\mathrm{S}}\mathbf{E} = \mathbf{y}$, where $\mathbf{E} = [E_{1,a}, E_{1,b}, ..., E_{M,c}, E_{M,d}]^{\mathbf{T}}$ and $\mathbf{y} = [1, 0, ..., 0]^{\mathbf{T}}$ resulted in the normalized electric field amplitudes at each interface. Normalization was done with respect to the input power ($P_{\mathrm{in}}(\lambda)$) allowing to solve the matrix equation only once for each wavelength, and scale the absolute values by the irradiance. See Supporting Information of **Publication II** for more information on the normalization.

Local normalized electric field ($E'(z,\lambda)$) was further calculated as a sum of the forward and backward propagating waves for each layer separately. Local electric field is especially useful for the absorber layer because it allows the calculation of local absorption [116]

$$A_j(z,\lambda) = P_{\mathrm{in}}(\lambda)\alpha_j(\lambda)\tilde{n}_j(\lambda)|E'(z,\lambda)|^2. \tag{22}$$

and further photogeneration

$$G_{\mathrm{ph}}(z) = \int_0^{\lambda_g} \frac{A_{\mathrm{PVK}}(z,\lambda)}{hc_0/\lambda}\, d\lambda, \tag{23}$$

where $\lambda_g = hc_0/E_{\mathrm{g}}$ corresponds to the band gap (E_{g}), and h and c_0 are the Planck's constant and the speed of light in vacuum, respectively. Strictly speaking, the sharp cut-off at E_{g} means that below band gap photogeneration (Urbach tail) is left out of consideration.

The choice of the practical implementation with the large system matrix $\mathbf{M}_{\mathrm{S}}$ was based on the numerical stability of the system matrix and the possibility to vary the level of coherence. Thus, thick layers like the glass substrate could be modelled in the stack. Partial coherence could also be set layer by layer. TMM is known for the so-called Ωd problem [122], that is, numerical instability due to large frequency (Ω) - thickness (d) products. In the context of solar cells, strong absorption is part of the potential problem in thick layers because the instability arises from the δ_j-term in the exponential of light propagation (see equation (18)). The system matrix relates to global transfer matrix, which is one of the methods to avoid the numerical instability [122]. Other possibilities include, for example, scattering matrix method and stiffness matrix method [122]. The drawbacks of the large system matrix were the slower computation time and larger memory consumption, but they could be afforded in this case.

2.3.2 Optical Constant Shift

Temperature affects the electronic structure of materials, which makes, for example, the band gap of semiconductors depend on the lattice temperature. Like the band gap, the optical constants (n,k) fundamentally relate to the electronic structure so they depend on the temperature as well. In **Publication II**, n and k were shifted in energy as a function of temperature by assigning a new energy value to each $(n(E),k(E))$ data point:

$$E_{\mathrm{new}} = E_{\mathrm{reference}} + \Delta E_{\mathrm{g}}, \tag{24}$$

where ΔE_{g} is the band gap change. So, n and k were essentially considered constant, apart from the shift in energy equal to the band gap change. The assumption

seems reasonable because the material stays basically the same. The changes in electronic structure mainly relate to the increased lattice constants when the temperature increases. Other optical constant shift functions, which share the same philosophy, have been applied in the literature [123].

Considering the validity of the approximation, it is hard to estimate an exact temperature range of validity. It is hypothesized that the approximation is valid as long as the effect of the temperature on the lattice is "small", for example, only lattice constants are affected. Notably, MAPI undergoes a lattice phase transition around 330 K [81]. Indeed, a discontinuity in the optical properties of MAPI over a phase transition has been observed (although, tetragonal and orthorhombic phases over the temperature range of 77 to 297 K were studied in that case) [124]. However, the differences in the optical constants spectra were still rather small overall [124]. In general, the validity of any approximation depends on the required accuracy.

A bolder assumption was made when the exact same optical constant shift function was applied to approximate the optical constants of different perovskites (**Publication II**). The concept was to take a reference perovskite material, MAPI, and model the general implications of the band gap change on the optical constants, as reported in the literature as well [125]. The band gap of perovskites is typically altered by varying the composition, that is, changing the atoms (or ions) at the different lattice sites, for example, by anion mixing. So, the crystal structure is still the same to a large degree, even though minor changes occur. However, atoms (/ions) differ from the reference material causing more significant changes in the electronic structure. Therefore, the approximation was definitely less accurate. Still, the method managed to capture the most important characteristics for the purpose and be accurate enough based on the comparison with experimental results [126; 127] (**Publication II** Supporting Information).

2.3.3 Spectral Absorption Factor

Generalized approximation for the absorption modelling can be useful in some cases. For example, some detailed material or device structure parameters may be left out of consideration on purpose to describe a general behaviour or there may be a need to find an approximative solution despite unavailable parameter values. Spectral absorption factor [128]

$$A_{\mathrm{s}} = \frac{\int A(\lambda) G(\lambda)\, d\lambda}{\int G(\lambda)\, d\lambda}, \tag{25}$$

where $G(\lambda)$ is the spectral irradiance, is a parameter describing the weighted average of absorption with respect to the irradiance spectrum. A_{s} itself is a general metric, and it could be estimated with TMM, for example, but approximations can also be introduced.

In **Publication III**, A_s was approximated with a total absorption factor

$$A_\mathrm{s} \approx \alpha_\mathrm{tot}(T_\mathrm{cell}) = \frac{\int_{300\,\mathrm{nm}}^{\lambda_\mathrm{g}(T_\mathrm{cell})} \alpha_{\lambda<\lambda_\mathrm{g}}\, G(\lambda)\, d\lambda + \int_{\lambda_\mathrm{g}(T_\mathrm{cell})}^{4000\,\mathrm{nm}} \alpha_{\lambda\geq\lambda_\mathrm{g}}\, G(\lambda)\, d\lambda}{\int_{300\,\mathrm{nm}}^{4000\,\mathrm{nm}} G(\lambda)\, d\lambda} \tag{26}$$

where T_cell is the cell temperature, λ_g is the wavelength corresponding to the band gap, and $\alpha_{\lambda<\lambda_\mathrm{g}}$ and $\alpha_{\lambda\geq\lambda_\mathrm{g}}$ are the effective spectral absorption constants above and below the band gap, respectively. Essentially, α_tot is the ideal step function approximation of absorption with the additional parameters $\alpha_{\lambda<\lambda_\mathrm{g}}$ and $\alpha_{\lambda\geq\lambda_\mathrm{g}}$ to consider non-idealities. The typical ideal absorption is found when $\alpha_{\lambda<\lambda_\mathrm{g}} = 1$ and $\alpha_{\lambda\geq\lambda_\mathrm{g}} = 0$. $\alpha_{\lambda<\lambda_\mathrm{g}} < 1$ describes practical absorption due to reflection. $\alpha_{\lambda\geq\lambda_\mathrm{g}} > 0$ was included because below band gap absorption affects cell heating even though it does not directly affect PCE.

2.4 Electrics

Upon photogeneration of the charge carriers, the dynamics of the carriers determine the solar cell operation. Ideally, the excited electrons and holes move to different areas (charge separation) and further into the external circuit via contacts. However, there are losses, in practice: the carriers may recombine, and generate light (radiative recombination) or heat (non-radiative recombination), before reaching the external circuit. Different models with varying levels of detail were applied to estimate the electrical operation of solar cells for different purposes.

2.4.1 Radiative Limit Model

Publication I applied a radiative limit model to estimate the optical PCE limits of the two proposed Bi-based absorbers for IPVs. Voltage dependent current production

$$J_\mathrm{rad,lim}(V) = q(G_\mathrm{ph} - R_\mathrm{rad}(V)), \tag{27}$$

where q is the elementary charge and R_rad is the radiative recombination, was calculated to produce JV curves. G_ph from the optical model was applied, see equation (23). Thermal radiative recombination was calculated according to the generalized Planck's law [129; 130]:

$$R_\mathrm{rad}(V) = \frac{2e_\Omega q^3}{h^3 c_0^2} \int_{E_\mathrm{g}}^{\infty} E^2 \left[\exp\left(q\frac{E-V}{k_\mathrm{B}T}\right) - 1\right]^{-1} dE, \tag{28}$$

where e_Ω is etendue (π for the emission of a black body into the air and into a hemisphere [130]), k_B is the Boltzmann constant, $T = 25\,^\circ\mathrm{C}$ is the cell temperature, and the integration was conducted over energies (in eV for the presented formula) larger than E_g applying the same cut-off at E_g as with the photogeneration in equation (23).

Emission according to equation (28) considers all angles to a half-space and (implicitly) different polarization states. Apart from the thermal radiation, perfect extraction of the generated charge carriers was assumed. PCEs for the different absorber materials under different irradiance conditions were extracted from JV curves.

The applied radiative limit model closely resembles the detailed balance model, which was arguably the first rigorous theoretical tool to estimate the solar cell performance limits. It was first applied to calculate the fundamental PCE limits of single-junction solar cells of varying band gaps, the so-called Shockley–Queisser limit [25]. The essence of the detailed balance method is to calculate IV curves by subtracting the radiative recombination from the photogeneration. However, perfect absorption above the band gap is commonly assumed for the (fundamental) theoretical limit. The difference of the applied method was to apply G_{ph} from the optical simulations based on measured material properties to provide more realistic optical limits.

Absorption is commonly considered independent of voltage (as also assumed in **Publication I**). The assumption is accurate in most cases although not exactly true. The applied voltage, for example, affects the cell temperature which in turn affects the material properties, including band gap, thus slightly changing the optics [123]. However, the effect is small within the typical PV operation temperature range (see, for example, **Publication II**).

2.4.2 Charge Transport by Drift Diffusion Equations

In **Publication II**, charge transport in the semiconducting layers, that is, the absorber and carrier selective layers, was modelled by the drift-diffusion equations. In practice, COMSOL Multiphysics (a commercial numerical simulation software) was applied. (Partial) differential equations (that is, the drift-diffusion equations) were solved as defined in the Semiconductor module of COMSOL. The key equations to construct and solve the problem are reviewed here.

The Poisson equation, in accordance with the Maxwell's equations, states that [131]

$$\nabla^2 \varphi = -\rho_{\mathrm{c}}/\epsilon, \tag{29}$$

where φ is the electric potential ($\vec{E} = -\nabla\varphi$) and ρ_{c} is the charge density. The equation took the form [132]

$$\frac{d^2V}{dz^2} = -\frac{q}{\epsilon_0 \epsilon_{\mathrm{r}}}(p_{\mathrm{h}} - n_{\mathrm{e}} + N_{\mathrm{d}} - N_{\mathrm{a}}) \tag{30}$$

for semiconductors in 1D, where n_{e} and p_{h} are the free-moving electron and hole densities, and N_{d} and N_{a} are the donor and acceptor doping densities, respectively. Fermi-Dirac statistics was applied for the carrier densities. The equation (30) was numerically solved for φ, n_{e}, and p_{h} constrained by the boundary conditions and carrier dynamics.

Voltage difference between the boundaries (electrodes) served as the boundary condition. Ideal Ohmic contacts between the transport layers and the electrodes were applied. In practice, the work functions of the contact and transport materials, for example, affect the type of interface (Ohmic or Schottky) that forms in between the layers. However, any specific interface was not the focus of the study, and the Ohmic contact is desired in solar cells due to the lower resistance.

The carrier dynamics were defined by the current-densities of electrons (J_n) and holes (J_p) [131; 132]

$$J_n = qn_{\mathrm{e}}\mu_n\nabla E_{\mathrm{c}} + qD_n\nabla n_{\mathrm{e}} - qn_{\mathrm{e}}D_n\nabla\ln(N_{\mathrm{c}}) + qn_{\mathrm{e}}D_{n,\mathrm{th}}\nabla\ln(T) \tag{31}$$

$$J_p = qp_{\mathrm{h}}\mu_p\nabla E_{\mathrm{v}} - qD_p\nabla p_{\mathrm{h}} + qp_{\mathrm{h}}D_p\nabla\ln(N_{\mathrm{v}}) - qp_{\mathrm{h}}D_{p,\mathrm{th}}\nabla\ln(T), \tag{32}$$

where μ_n and μ_p are the electron and hole mobilities, E_{c} and E_{v} are the conduction and valence band energy levels, N_{c} and N_{v} are the effective densities of states for the conduction and valence band, D_n and D_p are the diffusion coefficients of electrons and holes, and $D_{n,\mathrm{th}}$ and $D_{p,\mathrm{th}}$ are the thermal diffusion coefficients of electrons and holes, respectively. The first term on the right hand side describes the drift of charge carriers driven by the electric field. The second term describes the diffusion of carriers from high density area toward lower density area(s), and the third and fourth terms relate to the diffusion due to the temperature dependent occupancy of the bands. The latter terms were insignificant, in practice, that is, they were basically zero.

The source of electron and hole currents (J_n and J_p) is the photogeneration G_{ph} and the sink is the recombination (R)

$$-\frac{dJ_n}{dz} = \frac{dJ_p}{dz} = q(G_{\mathrm{ph}}(z) - R(z)). \tag{33}$$

Notably, the total current $J = J_n + J_p$ is constant throughout the device as stated by the current continuity. Local $G_{\mathrm{ph}}(z)$ was defined by the device optics as described above. Trap-assisted recombination according to the Shockley-Read-Hall (SRH) model was applied as the recombination term.

SRH recombination model determines the recombination rate as a function of carrier lifetimes of electrons (τ_n) and holes (τ_p). Carrier lifetimes of electrons and holes were considered equal ($\tau_n = \tau_p = \tau_{n/p}$), and it was calculated according to the (local) trap density ($N_{\mathrm{t}}(z)$). Local $N_{\mathrm{t}}(z)$ increases towards the interfaces [110]. As a consequence of the higher trap density at interfaces, interface recombination is typically larger than the bulk recombination, which was modelled by defining the local carrier lifetime [131]

$$\tau_{n/p}(z) = \frac{1}{N_{\mathrm{t}}(z)v_{\mathrm{th}}\langle\sigma\rangle}, \tag{34}$$

where $v_{\mathrm{th}} = 1.0 \times 10^7\,\mathrm{cm/s}$ is the thermal velocity of carriers and $\langle\sigma\rangle = 1.0 \times 10^{-15}\,\mathrm{cm}^2$ is the average capture cross-section of carriers.

The bulk trap density of the perovskite absorber was varied to study the effect on the device performance and heat generation. The subsequent changes in the diffusion length (L_d) were quantified by well-known relation [131]

$$L_\mathrm{d} = \sqrt{D\tau_{n/p}}, \tag{35}$$

where $D = \mu_{n/p} k_\mathrm{B} T/q$ is the ambipolar diffusion constant, $\mu_{n/p}$ is the ambipolar carrier mobility, k_B is the Boltzmann constant, and T is the temperature.

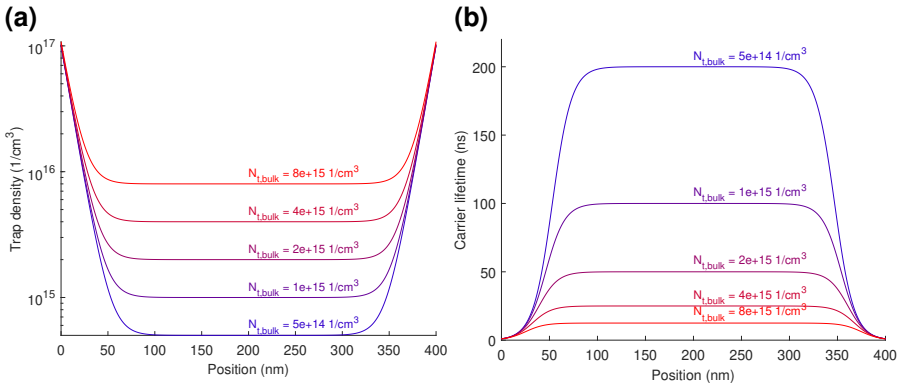

Figure 7. Material properties defining SRH recombination rate. Examples of local (a) trap density and (b) carrier lifetime as a function of position within a 400 nm thick perovskite absorber. Adapted from **Publication II** under CC-BY 4.0 licence.

2.4.3 Parametrized Performance Model

Publication III applied a temperature and irradiance dependent PCE formula to calculate the performance in varying conditions. The efficiency model was defined as

$$\mathrm{PCE}\,(G, T_\mathrm{cell}) = \mathrm{PCE}_\mathrm{ref}\left[1 + \frac{n_\mathrm{if} k_\mathrm{B} T_\mathrm{ref}}{V_\mathrm{OC,ref}\, q} \ln\left(\frac{G}{G_\mathrm{ref}}\right)\right](1 + \beta_\mathrm{PCE}(T_\mathrm{cell} - T_\mathrm{ref})), \tag{36}$$

where $\mathrm{PCE}_\mathrm{ref}$ is the reference PCE in $T = 25\,^\circ\mathrm{C}$ and $G_\mathrm{ref} = 1000\,\mathrm{W/m^2}$, n_if is the ideality factor of the cell, k_B is the Boltzmann constant, $V_\mathrm{OC,ref}$ is the open circuit voltage of the cell in reference temperature and irradiance, q is the elementary charge, and β_PCE is the temperature coefficient of PCE. The parametrized model provided a practical tool to compare perovskite and silicon panels under varying outdoor conditions focusing on the heat generation difference between the two panel types without defining cell level details.

2.5 Heat

Temperature affects the operation of solar cells. In general, material properties depend on temperature. Temperature also affects the thermal excitation of electrons to the conduction band. Therefore, higher temperature leads to higher carrier densities in the conduction (and valence) band, which accelerates recombination. Heat generation and heat transfer were modelled to study the outdoor operation temperature and performance of PSCs.

2.5.1 Heat Generation Mechanisms in Perovskite Solar Cells

Heat generation mechanisms in PSCs include [56–59]: 1) parasitic absorption (Q_{pAbs}), 2) thermalization (Q_{T}), 3) recombination (Q_{R}), 4) Joule heating (Q_{J}), 5) Peltier heat separately for electrons and holes ($Q_{\mathrm{P},n/p}$), and 6) heterostructure heat ($Q_{\mathrm{H},n/p}$ for electrons/holes). The common feature for the most heat generation mechanisms is, that the potential energy of the free-moving carriers converts to heat. The loss of the potential energy of the free-moving electrons relates to their decline in the energy level diagram (and vice versa for holes), as illustrated in Figure 8.

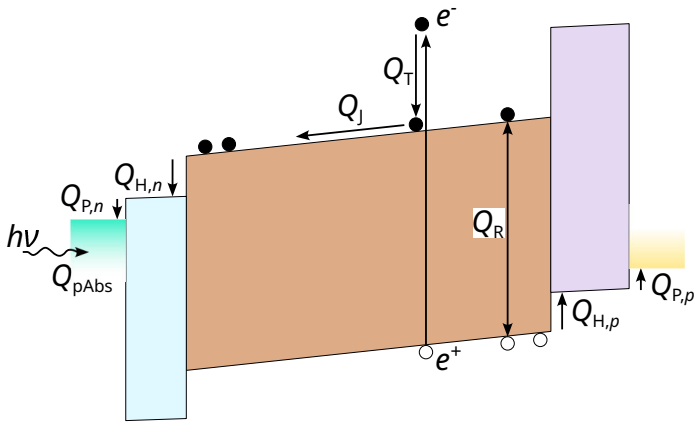

Figure 8. Heat generation mechanisms in heterostructure solar cells. The mechanisms are illustrated by the example of a PSC consisting of ITO/ ETL/ PVK/ HTL/ Au layers. Figure is not to scale.

Parasitic absorption is absorption that does not generate free-moving charge carriers. It occurs mainly in the layers other than the absorber, especially in the contact and charge transport layers, due to the free-moving electron absorption, for example. For each layer j, it was defined based on the local absorption

$$Q_{\mathrm{pAbs},j}(z) = \int_0^\infty A_j(z,\lambda)\, d\lambda. \tag{37}$$

Thermalization is the process of electrons (and holes) relaxing to the bottom (top)

of the conduction (valence) band from higher energy states. The excess energy of the carriers originates from the absorption of photons which carry more energy than the band gap. The relaxation occurs via carrier-carrier scattering, carrier-impurity scattering and carrier-phonon scattering [133–135]. The heat from thermalization [58]

$$\begin{aligned} Q_{\mathrm{T}}(z) &= \int_0^{\lambda_g} A(z,\lambda)\left(1 - \frac{E_{\mathrm{g}} + 3k_{\mathrm{B}}T}{hc_0/\lambda}\right) d\lambda \\ &= \int_0^{\lambda_g} G_{\mathrm{ph}}(z,\lambda)(hc_0/\lambda - (E_{\mathrm{g}} + 3k_{\mathrm{B}}T))\, d\lambda. \end{aligned} \tag{38}$$

Recombination is the elimination of free-moving carriers, that is, the transition of electrons from the conduction band to the valence band, and vice versa for holes. Non-radiative recombination includes, by definition, the recombination mechanisms that produce heat instead of emitting photons (radiative recombination). Trap-assisted recombination was considered the dominating recombination mechanism in **Publication II**, as discussed above.

$$Q_{\mathrm{R}}(z) = R(z)\,(E_{\mathrm{c}} - E_{\mathrm{v}} + 3k_{\mathrm{B}}T), \tag{39}$$

where the additional $3k_{\mathrm{B}}T$ relates to the mean thermal energy of both electrons and holes ($3/2\,k_{\mathrm{B}}T$) in the conduction and valence bands [57].

Joule heating (or Ohmic heating) is the heat generated when driving current through a resistive medium. The resistivity causes a potential gradient, which relates to an electric field. Thus, Joule heating can be calculated as a product of the current and the electric field [57; 58]:

$$Q_{\mathrm{J}} = \int \vec{J} \cdot \vec{E}\, dz. \tag{40}$$

Peltier heating originates from an electrical current over an energy level difference at a material interface. Here, the term 'Peltier heat' (Q_{P}) was applied to concern only semiconductor-metal interfaces whereas Peltier heating at semiconductor-semiconductor interfaces was called 'heterostructure heat' (Q_{H}). The terminology highlights the origin of Q_{H}, which only concerns heterostructure solar cells like PSCs, while contacts to an external circuit and Q_{P} is present in all solar cells. The Peltier and heterostructure heats were separately defined for each carrier type and each interface before summation [57–59]:

$$Q_{\mathrm{P},n} = J_n\,(E_{\mathrm{c}} + 1.5k_{\mathrm{B}}T - E_{\mathrm{F}n}) \tag{41}$$

$$Q_{\mathrm{P},p} = J_p\,(E_{\mathrm{F}p} - E_{\mathrm{v}} + 1.5k_{\mathrm{B}}T) \tag{42}$$

$$Q_{\mathrm{H},n} = -\Sigma_j J_{n,j} \Delta\chi_j \tag{43}$$

$$Q_{\mathrm{H},p} = -\Sigma_j J_{p,j} \Delta\big(\chi + E_{\mathrm{g}}\big)_j, \tag{44}$$

where $E_{\mathrm{F}n}$ and $E_{\mathrm{F}p}$ are the quasi-Fermi levels of electrons and holes, respectively, Δ refers to a local and discrete change in energy level, and χ is the electron affinity, which is defined as the potential difference between the bottom of the conduction band and the reference vacuum level. Notably, either type of Peltier heating at a specific interface may also be negative. That is, current over an energy level difference could also cool down the lattice, if the carriers are driven from a lower energy level to a higher one. However, such a shift in energy level would act as a barrier for charge extraction.

2.5.2 Heat Generation Based on the Energy Balance

Calculation of the specific heat generation mechanisms requires detailed charge transport modelling and the related material parameters. On the other hand, energy balance states that the absorbed energy which is not converted to electricity becomes heat, that is, energy must be conserved. Therefore, exact processes need not be modelled if only total heat generation is of interest and the optical and electrical characteristics can otherwise be defined to a satisfactory level of accuracy. Total heat generation model was formulated accordingly based on the energy balance:

$$Q(G, T_{\mathrm{cell}}) = (1 - \eta_{\mathrm{e}}(G, T_{\mathrm{cell}}))\, \alpha_{\mathrm{tot}}(T_{\mathrm{cell}})\, G, \tag{45}$$

where η_{e} is the so-called electrical conversion factor defined as

$$\eta_{\mathrm{e}}(G, T_{\mathrm{cell}}) = \frac{\mathrm{PCE}\,(G, T_{\mathrm{cell}})}{\alpha_{\mathrm{tot}}(T_{\mathrm{cell}})}, \tag{46}$$

where $\mathrm{PCE}\,(G, T_{\mathrm{cell}})$ and $\alpha_{\mathrm{tot}}(T_{\mathrm{cell}})$ were defined according to equations (36) and (26), respectively. So, η_{e} is the share of absorbed energy that is converted to electricity.

2.5.3 Heat Transfer

The three modes of heat transfer are conduction, convection, and radiation. Within the modelled cells or panels, heat transfer was modelled by the conduction[136], which typically dominates the heat transfer in solids. In steady-state,

$$-\kappa\, \nabla^2 T = Q, \tag{47}$$

where κ is the material-specific thermal conductivity and Q is the total heat generation. The total heat generation was calculated as a sum of the individual heat generation mechanisms (section 2.5.1) or obtained by the total heat generation model (section 2.5.2) presented above. For the heat exchange with the environment, convection [136]

$$H_{\mathrm{conv}} = h_{\mathrm{c}}(T_{\mathrm{b}} - T_{\mathrm{amb}}) \tag{48}$$

and radiation [136]

$$H_{\mathrm{rad}} = \epsilon_{\mathrm{s}}\sigma(T_{\mathrm{b}}^4 - T_{\mathrm{amb}}^4) \tag{49}$$

were considered, where h_{c} is the convection coefficient, ϵ_{s} is the emissivity of the surface material, σ is the Stefan-Boltzmann constant, T_{amb} is the ambient temperature, and T_{b} is the device temperature at the (front or rear) boundary.

The temperature distributions in cells (**Publication II**) and modules (**Publication III**) were numerically solved with COMSOL as defined in its Heat Transfer module and presented above. Heat generation mechanisms were inserted (for **Publication II**) as presented in section 2.5.1, apart from the Joule heating and non-radiative recombination heating, which had been readily implemented in the Heat Transfer module. Because the added heat generation methods can be directly calculated from the optical and electrical inputs, no additional (partial) differential equations had to be inserted for solving the temperature. Instead, iterative approach was used to couple the models.

2.6 Material Properties

Material properties and other model parameters are of key importance for computational PSC (or any other) modelling because the properties essentially define what is modelled. "The output is as good as the input" for any model. **Publication I** produced the optical constants for two IPV absorber candidates, which were then applied in the optical modelling. In addition to these data, vast amount of literature parameters was utilized in different calculations. The applied literature data include the optical constants of different cell and panel materials [125; 137–142], electrical properties of semiconductor materials [110; 111; 125; 143–156] applied in **Publications I**, **II**, and **IV**, parametrized performance model inputs [60; 111; 157–163] applied in **Publication III**, and thermal material properties [144; 164–170] applied in **Publications II** and **III** (see original publications for tabular data).

2.7 Numerical Considerations

MATLAB and COMSOL Multiphysics were used for the performed computations. It is assumed that mostly minor numerical errors have occurred. A few points are still interesting to note.

The irradiance and optical property spectra of different materials were discrete datasets of varying wavelength step size. Cubic spline interpolation was applied when necessary. Integration over different spectra were performed by the direct summation multiplied by the step size or by application of the trapezoidal rule. Insignificant differences have been observed so far.

The inclusion of an arbitrary phase change in TMM to account for the (partial) incoherence did not strictly conserve energy. However, the relative error was in the

order of 1% at maximum. The error also varied from wavelength to another, so some errors cancelled each other to some extent when integrating over a spectrum.

In **Publication I**, Critical Point fitting was performed on the second derivatives of ϵ. Explicit numerical differentiation was avoided by utilizing the coefficients of the smoothing polynomials fitted into the raw data. [171]

Optical, electrical, and thermal models were coupled to each other in **Publication II**. Electrical and thermal models were coupled within COMSOL. Iteration until a change of below 0.1 K was performed to converge the cell operation temperature under temperature dependent optical calculations in MATLAB. The effect of mesh size, that is, spatial discretization for the accuracy of the drift-diffusion model was studied, as shown in Figure 9. Maximum element size of 1 nm was concluded appropriate considering the accuracy and computational cost, and it was applied in the presented simulations of **Publication II**.

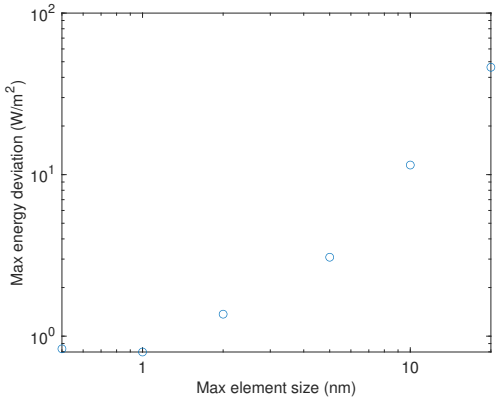

Figure 9. Energy conservation convergence in the drift-diffusion model as a function of maximum element size. Maximum energy deviation was taken over all voltage points, band gaps $1.2\,\mathrm{eV}, 1.57\,\mathrm{eV}, 2.2\,\mathrm{eV}$, PVK thicknesses $200 - 1000\,\mathrm{nm}$ by $20\,\mathrm{nm}$ steps, and cell temperatures $15 - 55\,^{\circ}\mathrm{C}$ by $10\,^{\circ}\mathrm{C}$ steps. Adapted from **Publication II** under CC-BY 4.0 licence.

2.8 Thermal Model Validation with Experimental Data

Publication III applied experimental data [172] from an outdoor measurement setup of the Finnish Meteorological Institute [173] to validate the applied thermal model and the simulated panel temperatures. A subset of the experimental data was chosen as the validation dataset to limit the computational cost. The experimental datapoints closest to the following conditions (by the Euclidian norm) were included in the validation set: ambient temperatures from $5\,^{\circ}\mathrm{C}$ to $30\,^{\circ}\mathrm{C}$ with steps of $5\,^{\circ}\mathrm{C}$, wind speeds from $1\,\mathrm{m/s}$ to $10\,\mathrm{m/s}$ with steps of $1\,\mathrm{m/s}$, and irradiances from $100\,\mathrm{W/m^2}$ to $1000\,\mathrm{W/m^2}$ with steps of $100\,\mathrm{W/m^2}$ (Figure 10a). For the model validation, model parameters (that is, $\mathrm{PCE_{ref}}$ and β_{PCE}) were set according to the values reported by

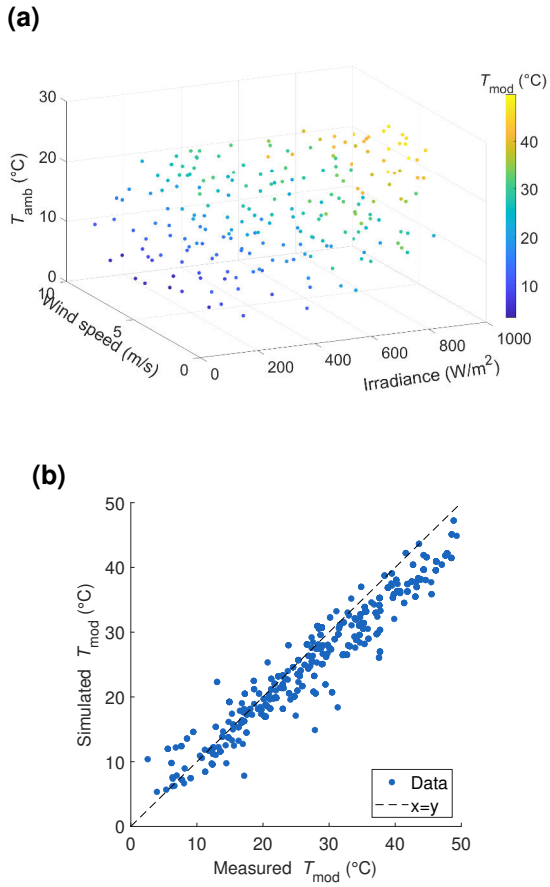

Figure 10. Validation of the thermal model. (a) Validation dataset of the experimental silicon module temperatures in varying uotdoor conditions. (b) Comparison of the simulated silicon module temperature with the measured one. Adapted from **Publication III** under CC-BY 4.0 licence.

the manufacturer, and the simulated temperatures were compared with the measured ones.

Good correlation between the measured and simulated module temperatures was obtained (Figure 10b). The observed variance may arise from inaccuracies in experimental input values (T_{amb}, G, v_{w}) or model parameters, but also from model characteristics. The model simulates steady-state temperatures, so fast changes in weather conditions, for example, due to the start of a rain, was not included. Operation under exceptional conditions, such as partial shading, was out of the scope as well. The small deviation of the slope from the perfect correlation (Figure 10b) was probably due to the unoptimized convection coefficients for the specific location and installation (**Publication III**).

3 Experimental Methods

Publication I was the only publication, which produced experimental data. The optical constants of novel absorber materials for IPVs were measured by spectroscopic ellipsometry. The samples were prepared on single-side polished Si substrates as described in **Publication I**. The essential characterization methods, that is, ellipsometry and atomic force microscopy (AFM), are briefly described here.

3.1 Spectroscopic Ellipsometry

Spectroscopic ellipsometry is an optical measurement technique to measure sample structure, for example, film thickness and/or surface morphology, and material properties, such as the optical constants. It is based on the measurement of the change of light polarization caused by interaction with a sample, see Figure 11. Reflectance (and transmittance) of light at a material interface depends on the polarization of light at a finite incidence angle ($\theta \neq 0$), as described by the Fresnel equations (3)-(6). It means that, in general, the polarization state of light may change upon reflection, and the change depends on the optical properties of the sample, which is utilized in SE to characterize the optical properties of materials.

The polarization change is commonly represented by the amplitude ratio Ψ and the phase difference Δ between $\parallel$ and $\perp$ polarizations, which are defined by the

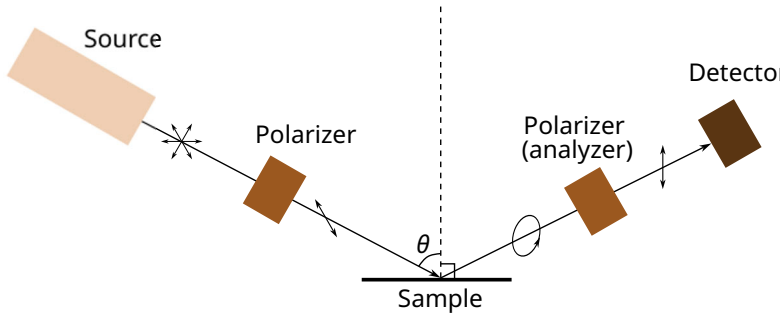

Figure 11. An illustration of a general ellipsometry measurement set-up. Concept of the change of the polarization state upon reflection is visualized; it does not necessarily relate to any conducted measurements.

complex reflection coefficients of the Fresnel equations [174]:

$$\tan(\Psi)\exp(\mathrm{i}\Delta) = \frac{\rho_{\parallel}}{\rho_{\perp}} = \frac{E_{\mathrm{r},\parallel}/E_{\mathrm{i},\parallel}}{E_{\mathrm{r},\perp}/E_{\mathrm{i},\perp}}. \tag{50}$$

Source beam of a known polarization is directed at the sample and the polarization of the reflected beam is measured. In SE, a spectrum of wavelengths/energies is applied. Typically, a set of a few different incident angles is also applied to obtain more data. The optical properties are extracted by fitting an optical model.

In **Publication I**, J.A. Woollam VASE ellipsometer and WVASE software were utilized for SE measurements and analysis. Wavelengths from 300 to $2500\,\mathrm{nm}$ and incidence angles of $55\,^{\circ}$, $65\,^{\circ}$, and $75\,^{\circ}$ were applied. Tauc-Lorentz oscillator model and point-by-point fitting were both applied for the optical constant modelling. Structurally, the fitted optical model consisted of a thick Si substrate with a thin natural oxide layer and the sample layer, which was modelled with the graded Bruggeman effective medium approximation (EMA) to account for sample roughness [175]. The Si substrate was single-side polished so the back-side was rough and reflection from the back-side of the substrate was considered insignificant.

Ellipsometry has two advantages over typical transmittance and/or reflectance measurements: 1) both n and k are determined simultaneously as a function of wavelength and 2) relative amplitudes (and phase differences) of different polarizations are applied in ellipsometry [176]. In absolute light intensity based transmittance/reflectance measurements, one has to make assumption(s) on n to determine k (and α). In addition, absolute intensity based measurements are prone to sample imperfections, such as scattering. Considering scattering may not be straightforward in ellipsometry either, but it can and should be included in ellipsometry analysis. The arguable complexity and the involved decisions in ellipsometry analysis can be counted as disadvantage for ellipsometry. It is an indirect measurement technique (n, k are obtained via a model fitting) where the modelling choices affect the result, which makes it somewhat vulnerable to human errors. Therefore, it is important to carefully consider an appropriate model for each sample.

The structural characterization of a sample by SE is based on the sensitivity of Ψ and Δ to the sample structure. However, for the characterization of the optical constants of a material, as in **Publication I**, the structure sensitivity of SE requires studying the sample structure as well. The sample structure was obtained by fitting the optical model to the SE data, and it was further validated by AFM.

3.2 Atomic Force Microscopy

Atomic force microscopy is a versatile surface characterization and imaging technique [177]. Versatility refers to the wide range of samples across materials and length scales and different properties that can be measured with AFM. AFM is based

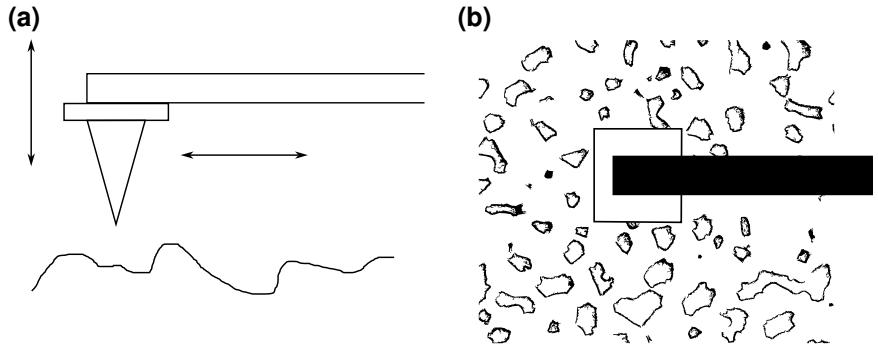

Figure 12. Illustration of an AFM scan on a sample. Two-dimensional (a) side view and (b) top view.

on the measurement of the interaction between a probe ('tip') and the sample surface. The tip is scanned over an area (see Figure 12), while measuring the 'height' (a force at the tip) of the sample across that area, thus, enabling to create a three-dimensional image of the sample. The height can refer to the actual physical height of the sample but also to different properties depending on the measurement mode, that is, which interaction is measured.

In **Publication I**, AFM (Park Systems NX10) was applied to measure the height distributions of the samples for the validation of the ellipsometry fitted sample structures (film thicknesses and roughnesses). The AFM images were processed using Gwyddion (version 2.68) [178; 179]. The AFM data were interpreted to provide the film thickness distributions of the samples, in addition to the surface roughness data, because the complementary scanning electron microscope (SEM) and energy-dispersive X-ray spectroscope (EDS) images revealed partial sample coverage, that is, the Si substrate acted as the height reference point (see **Publication I** Supporting Information).

Initially, cross-section SEM was considered to determine the layer thicknesses of the samples. However, cross-section SEM provides two-dimensional data. AFM scans an area providing more and three-dimensional data, and in this specific case, it was also able to provide thickness data in addition to the roughness data (as discussed above), which was a key factor in favour of AFM for the specific study.

4 Optical Characterization and Simulation of Perovskite-Inspired Materials for Indoor Photovoltaics

As discussed in the Introduction section, indoor photovoltaics present an unusual, yet promising application for PSCs and related technologies. Due to the difference in the irradiance spectrum, a wider band gap is preferred compared with the typical optimal band gap under the solar irradiance. Further, lead-free alternatives are likely to enhance the sustainability of solar cells themselves. **Publication I** characterized and modelled two lead-free perovskite-inspired materials, called CABI and CBI, to study their optical performance limits for IPV applications.

4.1 Characterization

Spectroscopic ellipsometry was applied to find the optical constant spectra of CABI and CBI. SE is known for its sensitivity to structural properties, such as film thickness and surface morphology. Therefore, the sample structure was first studied by AFM and SEM to characterize the surface roughness, film thickness, and sample coverage.

4.1.1 Sample Structure

SEM and AFM showed the sample thickness vary with the precursor concentration, as intended (Figure 13). Samples of different thicknesses were prepared to consider and limit the possible effect of external properties (thickness and surface morphology) on the measurement of the optical constants. In addition to the different sample thicknesses, AFM also showed the samples to be rough, as shown by the line height profiles (Figure 13c) and wide height distributions (Figure 13d). The CABI samples with the median heights of $60\,\mathrm{nm}$, $112\,\mathrm{nm}$, and $281\,\mathrm{nm}$ varied from zero up to $275\,\mathrm{nm}$, $882\,\mathrm{nm}$, and $893\,\mathrm{nm}$, respectively, although the height values over $150\,\mathrm{nm}$, $250\,\mathrm{nm}$, and $500\,\mathrm{nm}$, respectively, were extremely rare (Figure 13d). The data were interpreted as actual height data instead of only surface morphology because SEM revealed partial sample coverage, that is, the reference height was the substrate surface (see **Publication I** Supporting Information). CBI samples seemed to grow larger grains based on their visual appearance in SEM and AFM, which led to more flat ar-

eas in the line height profiles (**Publication I** Supporting Information). Otherwise, the CBI samples were similar in nature to the CABI samples. They were also rough, and the sample thicknesses were of the same order of magnitude.

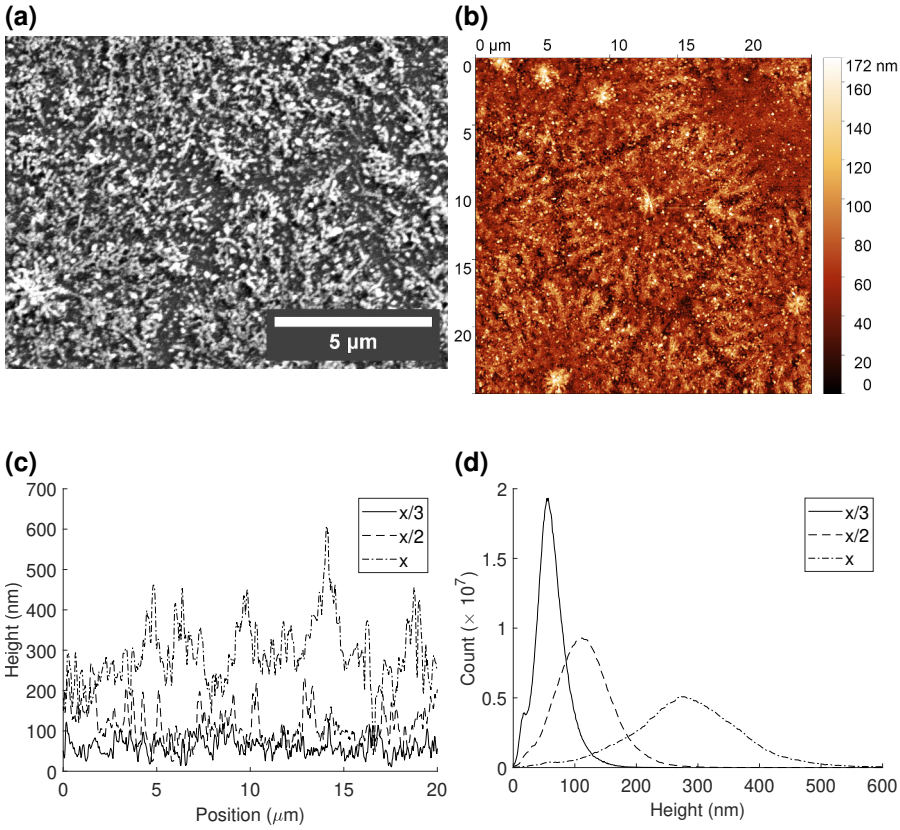

Figure 13. Sample structure characterization. (a) SEM image of an example sample called $\mathrm{CABI}_{50\mathrm{nm}^*}$ after the fitted median layer thickness. (b) AFM image of $\mathrm{CABI}_{50\mathrm{nm}^*}$ sample. (c) Example AFM line height profiles of different thickness samples labelled after the precursor concentration (defined as x), which was further diluted to concentrations x/2 and x/3 to fabricate the different thickness samples. The labels correspond to the samples $\mathrm{CABI}_{50\mathrm{nm}^*}$ (x/3), $\mathrm{CABI}_{78\mathrm{nm}}$ (x/2), and $\mathrm{CABI}_{273\mathrm{nm}}$ (x). (d) Height distributions of $\mathrm{CABI}_{50\mathrm{nm}^*}$ (x/3), $\mathrm{CABI}_{78\mathrm{nm}}$ (x/2), and $\mathrm{CABI}_{273\mathrm{nm}}$ (x) samples. Adapted from **Publication I** under CC-BY 4.0 licence.

Because of the sample roughness, graded effective medium approximation (EMA) model was applied in ellipsometry, Figure 14a. That is, the sample films were modelled as 21 sublayers of film/air EMA layers with a quasi-continuous decrease (increase) of the sample (air) content from the substrate-film interface to the top of the film ”surface”. The choice of using exactly 21 sublayers for the EMA layer was based on the sensitivity analysis of results when varying the number of sublayers (see **Publication I** and related Supporting Information Figures S14-S16). The prin-

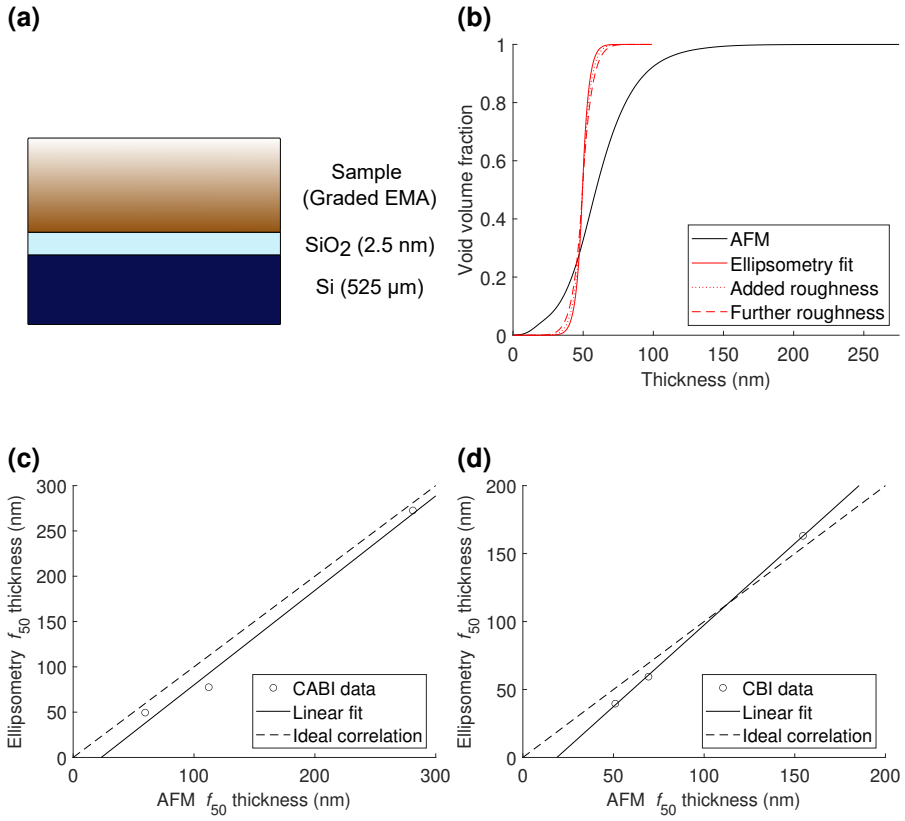

Figure 14. Sample structure validation. (a) Illustration of the applied sample structure model in ellipsometry analysis. (b) Normalized cumulative void volume fraction of the graded EMA layer, example sample $\mathrm{CABI}_{50\mathrm{nm}^*}$. (c,d) Comparison of the median thicknesses based on ellipsometry fits and AFM characterization of different thickness CABI (panel c) and CBI (d) samples. Adapted from **Publication I** under CC-BY 4.0 licence.

ciple is that more sublayers can model the roughness more accurately. On the other hand, the complexity of the model increases with the increasing number of sublayers. 21 was considered necessary and adequate number of sublayers based on the analysis. The potential issue, which was tackled with the graded EMA model, is that an oversimplified roughness model can overestimate the absorption coefficient [180]. Graded EMA model has previously been successfully applied to model rough samples in the literature [175]. Another point to be aware of is the potential depolarization, which would require more complicated Stokes vector-Mueller matrix calculus [181]. Surprisingly, depolarization was measured to be small despite the roughness (**Publication I** Supporting Information) enabling the application of the regular Jones vector.

The layer thicknesses and sample volume fractions (f) of the graded EMA model were fitted to the ellipsometry data, and the fitted structures were compared with the AFM data (see Figure 14b for an example). Ellipsometry fits underestimated the variance in sample height, as shown by the sharper step in the void volume fraction of ellipsometry fit compared with AFM data in Figure 14b. However, good quantitative agreement between f_{50} values (the film thickness corresponding to the 50% sample volume fraction) from AFM measurement and ellipsometry fitting for both CABI and CBI was observed, see Figures 14c and 14d. Therefore, the graded EMA model with the ellipsometry fitted film thicknesses was concluded realistic.

Together with the structure parameters, a coarse estimation of the optical constants was found. Tauc-Lorentz oscillator model (with three oscillators) was applied to model the optical constants. To find more accurate optical constants and improve the ellipsometry data fits, the sample structure parameters were fixed and point-by-point fitting was applied for the optical constant spectra.

4.1.2 Optical Properties

Good ellipsometry fits were obtained, that is, the simulated amplitude ratio (Ψ) and phase difference (Δ) matched the measurement (Figure 15). However, the mean square error (MSE) of the fits increased with the film thickness (**Publication I** Supporting Information). Thinner films have been reported to provide better results in the literature as well. Some variation in the fitted optical constant spectra was observed: relative changes were ca. $10\,\%$ for CABI and ca. $30\,\%$ for CBI right above the band gap (**Publication I** Supporting Information).

The found optical constants of CABI and CBI are presented in Figure 16 as the complex refractive index and complex dielectric constant, which are mathematically interconvertible representations of the optical properties. Considering the variance in optical constants between the samples (**Publication I** Supporting Information), pointwise mean values with standard deviations were reported. Strong absorption for both materials was observed: $\alpha(\mathrm{CABI}) \approx 1.7 \times 10^5\,\mathrm{cm}^{-1}$ and $\alpha(\mathrm{CBI}) \approx 2.2 \times 10^5\,\mathrm{cm}^{-1}$ right above the respective band gaps. The band gaps were extracted from the optical constants (especially, the imaginary parts) via three different methods, namely Tauc plot, Elliot's model and Critical Point fitting (Table 1, see **Publication I** Supporting Information for the fits). Tauc plot produced slightly smaller values than the other two methods, but overall, good agreement between the methods was observed.

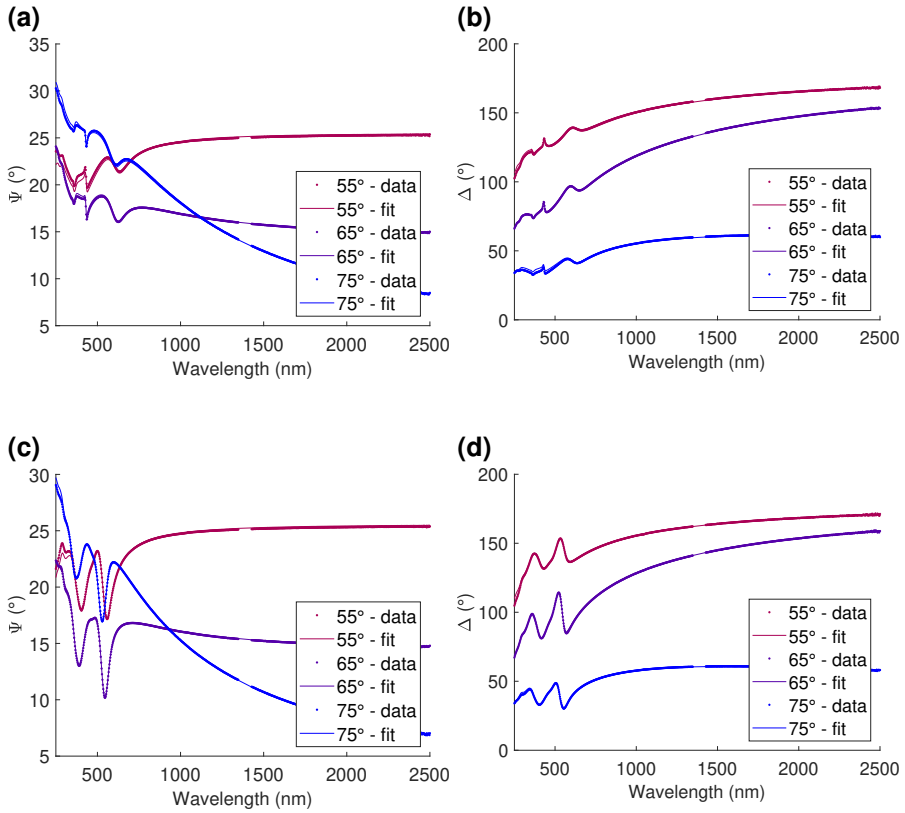

Figure 15. Ellipsometry fits. (a) Amplitude ratio Ψ and (b) phase difference Δ for $\mathrm{CABI}_{50\mathrm{nm}}$. (c) Ψ and (d) Δ for $\mathrm{CBI}_{40\mathrm{nm}}$. Measured Ψ and Δ (symbols) and model fits (solid lines) for the three applied incidence angles. Adapted from **Publication I** under CC-BY 4.0 licence.

Table 1. Band gap energies of the two Bi-PIMs obtained by different methods. Adapted from **Publication I** under CC-BY 4.0 licence.

	Tauc plot (direct, allowed)	Elliott's model	Critical Point
CABI	1.98 eV	2.03 eV	2.09 eV
CBI	2.33 eV	2.43 eV	2.39 eV

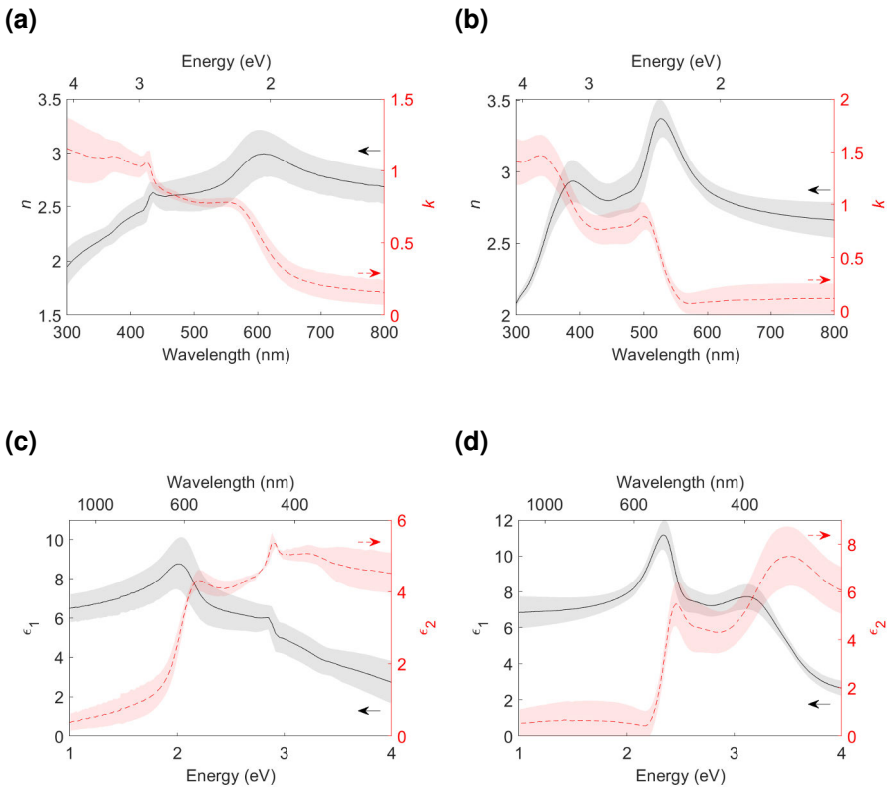

Figure 16. Optical constants of CABI and CBI. (a,b) The complex refractive index spectra of CABI (panel a) and CBI (b). (c,d) The complex dielectric constant spectra of CABI (c) and CBI (d). The spectral ranges were chosen to focus on the application relevant range, see **Publication I** Supporting Information for the full range of $300\text{-}2500\,\mathrm{nm}$ and the related public repository upload for the tabulated data. Adapted from **Publication I** under CC-BY 4.0 licence.

4.2 Optical Efficiency Limits

Having found the optical constant spectra of the two materials, optical device modelling was applied to study solar cells with CABI and CBI as the absorber, respectively (Figure 17a). A typical reference device of SiO_2 / FTO / compact TiO_2 (c-TiO_2) / CABI or CBI / 2,2',7,7'-Tetrakis[N,N-di(4-methoxyphenyl)amino]-9,9'-spirobifluorene (Spiro-OMeTAD) / Au stack with the planar structure was applied. Same materials have been applied in state of the art experiments of these devices [182].

Absorption sets an optical limit for the external quantum efficiency (EQE) of solar cells. That limit for the simulated CABI solar cell was found to oscillate between ca. $84\,\%$ and ca. $92\,\%$ under the wavelength range of $400 - 635\,\mathrm{nm}$ (Figure 17b). The oscillation was due to interference in the thin layers of the device, which are located above the absorber, that is, FTO and c-$\mathrm{TiO_2}$. Similar absorption limit was observed with CBI absorber as well, except the difference due to the wider band gap (**Publication I** Supporting Information).

Optical losses include reflection and parasitic absorption. Reflection varied between ca. $5 - 20\%$ over the simulated range. Parasitic absorption was strong for the higher energy range ($< 400\,\mathrm{nm}$), which is typical because many materials tend to absorb high energy photons, including the wide band gap $\mathrm{TiO_2}$. Otherwise, parasitic absorption remained at or below ca. 5%.

Strong below band gap absorption in CABI ($> 635\,\mathrm{nm}$) remains a question. The simulated absorption at the long wavelengths (Figure 17b) originates from the non-zero imaginary part of the refractive index at the corresponding range (Figure 16a). However, the reason for the non-zero extinction coefficient ($k(E < E_\mathrm{g}) > 0$) is uncertain. It could be a scattering related artefact, but emphasis was put on the appropriate roughness modelling. Possible tail states could induce absorption. On the other hand, atomistic simulations have suggested states to occur at smaller energies (in reference to the valence band maximum) compared with the band gap. The existence and effect on device operation of any states within the gap could be of interest for future research.

The normalized absorption (Figure 17b) can straightforwardly be multiplied by an irradiance spectrum to estimate the photogeneration and subsequently the maximum achievable photocurrent in the absorber, which was done with the indoor spectra of different colour temperatures (Figures 17c and 17d) and the solar spectrum (**Publication I** Supporting Information). The calculation produced an integrated maximum achievable photocurrent (Int. J_ph) of $91.1\,\mu\mathrm{A\,cm^{-2}}$ under the indoor irradiance with a colour temperature of 4000 K and an illuminance of 1000 lx (a power density of ca. $3\,\mathrm{Wm^{-2}}$) and Int. J_ph of $12.9\,\mathrm{mA\,cm^{-2}}$ under the solar irradiance (AM1.5G, $1000\,\mathrm{Wm^{-2}}$ power density) for the simulated CABI device. Corresponding limits of $32\,\mu\mathrm{A\,cm^{-2}}$ and $7.2\,\mathrm{mAcm^{-2}}$ under the 4000 K, 1000 lx indoor and so-

lar irradiances, respectively, were similarly obtained for the CBI device (**Publication I** Supporting Information). The lower photocurrent generations in CBI solar cell compared with CABI device were due to the wider band gap.

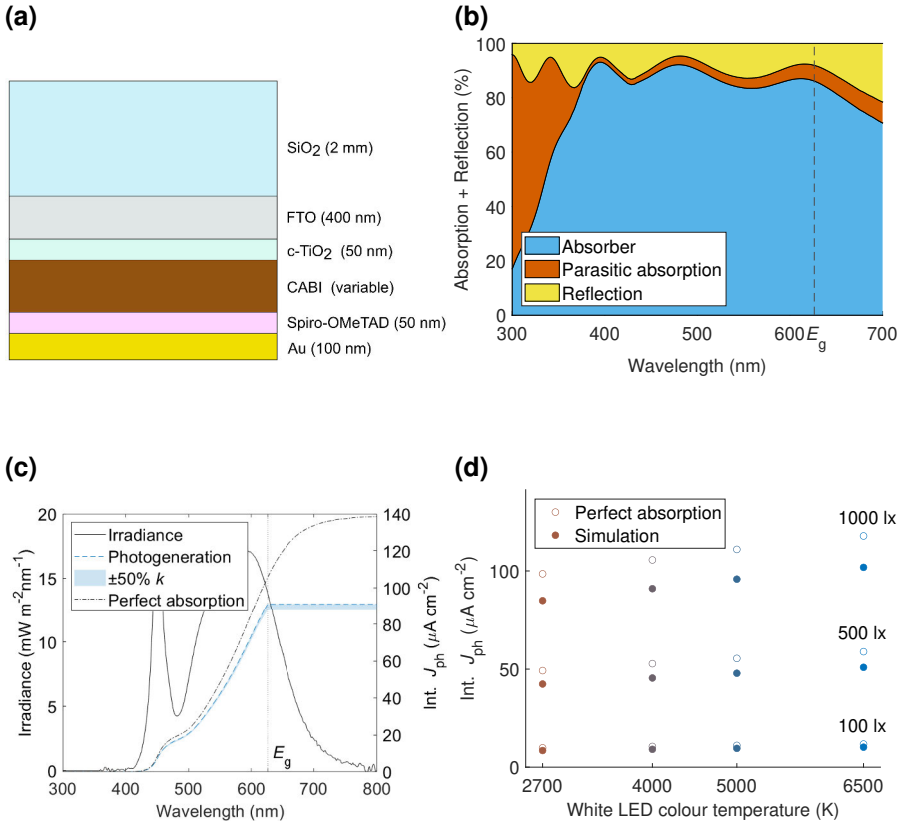

Figure 17. Optical simulation of the CABI device. (a) Illustration of the modelled planar device structure. Figure is not to scale. (b) Simulated, normalized absorption and reflection. CABI thickness of $220\,\mathrm{nm}$ was applied for these data. (c) Simulated $\mathrm{Int.}\,J_{\mathrm{ph}}$ under 4000 K, 1000 lx WLED irradiance. The shaded are represents the sensitivity analysis with linearly scaled k spectra. (d) $\mathrm{Int.}\,J_{\mathrm{ph}}$ for varied indoor spectra of different colour temperatures and illumination levels. Adapted from **Publication I** under CC-BY 4.0 licence.

Colour temperature is a metric of indoor lighting that describes the perceived colour of the irradiance compared with the colour of a thermal source of certain temperature. The higher the colour temperature, the more high energy photons are emitted and vice versa. Because the indoor spectrum changes with the colour temperature, it also affects the current generation. $\mathrm{Int.}\,J_{\mathrm{ph}}$ of CABI device varied from $85\,\mu\mathrm{A\,cm^{-2}}$ at 2700 K to $102\,\mu\mathrm{A\,cm^{-2}}$ at 6500 K with the constant illuminance of 1000 lx (Figure 17d). In CBI device the change was more significant due to the wider band gap and narrower absorption band: $\mathrm{Int.}\,J_{\mathrm{ph}}$s from 21 to $50\,\mu\mathrm{A\,cm^{-2}}$,

respectively, under different colour temperatures from 2700 K to 6500 K with the constant illuminance of 1000 lx were observed (**Publication I** Supporting Information). The effect of illuminance level on Int. J_{ph} is linear for each colour temperature separately, as also appears in Figure 17d.

The predicted photocurrent generation limits proved to be robust even to large extinction coefficient variance (Figure 17c and **Publication I** Supporting Information). k spectra of CABI and CBI were linearly scaled by a factor (f_k), which varied from 0.5 to 1.5, as a sensitivity analysis due to the observed variance between different samples. The relative changes in Int. J_{ph}s were less than 5% for both CABI and CBI devices. However, the optimal absorber thickness varied with f_k (**Publication I** Supporting Information), which highlights the importance of accurate optical constants for the device design.

n spectra were also varied similarly to k spectra for completeness (**Publication I** Supporting Information). Scaling factor f_n varied from 0.9 to 1.1. Minor and straightforward effect on Int. J_{ph}s was noticed. Larger n increased reflectance and decreased Int. J_{ph}.

Purely optical simulations provide information mainly on the absorption and photogeneration. To understand and quantify the meaning of the optics for the device efficiency (limits), radiative limit PCEs were calculated. The radiative-limited PCEs of ca. 42% and 18% for CABI and CBI devices under 4000 K, 1000 lx indoor illumination were obtained with realistic absorber layer thicknesses of $220\,\mathrm{nm}$ and $210\,\mathrm{nm}$, respectively (Figure 18). These limits were notably higher than the corresponding limits of 20% and 13% for CABI and CBI devices under the reference solar irradiance as expected. The absorber layer thickness dependence of the radiative limit PCEs followed directly from the absorber thickness dependence of G_{ph}s. The effect of the increasing film thickness on the recombination rates was not considered because radiative-limited behaviour was studied. The effect of the realistic optics based on the measured optical constants and optical simulation compared with the perfect absorption assumption was approximately 15%, which agrees well with a previous estimation in the literature [183].

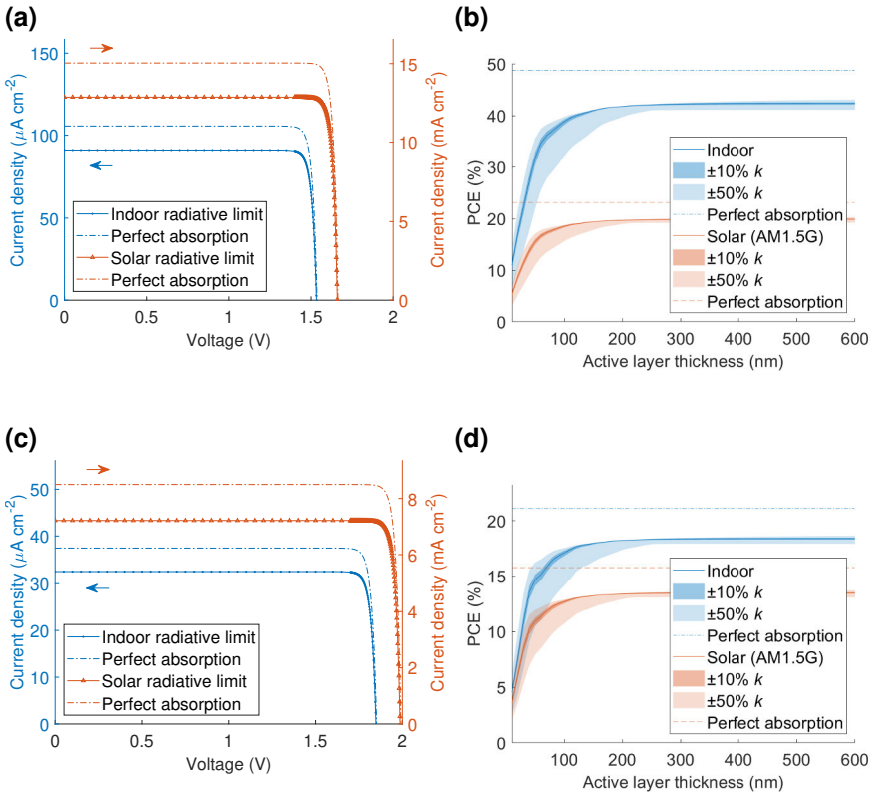

Figure 18. Radiative limit PCEs. (a,c) JV curves and (b,d) PCE limits of CABI (panels a and b) and CBI (c,d) devices under 4000 K, 1000 lx indoor and solar irradiances. Realistic optics (solid lines) and perfect absorption (dotted lines) were applied for photogeneration calculation. Adapted from **Publication I** under CC-BY 4.0 licence.

4.3 Discussion on the Optical Properties

The measured optical constant spectra represent fundamental material properties governing the interaction of the materials with light. As such, they are of interest for the fundamental understanding of the material characteristics and the possible utilization of these materials in optoelectronic applications. The conducted simulations, which applied the two materials as absorbers in a reference solar cell, demonstrate one promising application.

Perpendicular irradiance was considered in the calculations. In practice, angular dependence of the device operation in the IPV applications is expected to be significant considering the high likelihood of diffuse light indoors. However, the main motivation for **Publication I** was to understand the fundamental optical properties of the studied lead-free PIMs and produce insights on the factors, which limit the experimental device performance at the moment. The experiments are commonly conducted in the perpendicular setting at this point of technology development, which guided the modelling choice for the study.

The observed sample roughness presents a possible source of inaccuracies in the determined spectra. Surface roughness has been reported to overestimate the absorption coefficient [184]. Appropriate roughness modelling was emphasized to alleviate the issue, and sensitivity analysis was conducted to quantify the effect of the uncertainty on the simulation results. It should be noted that surface roughness is rather common for this type of solar cell materials [180; 185]. In the future, computational simulation of the optical constants themselves based on first principles methods could also be conducted to compare with the experimental results and gain deeper understanding of the origins of the absorption properties [186]. Increased confidence level in the optical constants would further allow more detailed layer thickness optimization.

Maybe more importantly, more precise values of the band gaps would increase the accuracy of the predictions, as shown by the band gap sensitivity analysis of the radiative limit calculations. PCEs of both CABI and CBI devices varied over 10%-points under the studied band gap ranges of 1.9 to $2.1\,\mathrm{eV}$ and 2.2 to $2.45\,\mathrm{eV}$, respectively (**Publication I** Supporting Information). Three different methods, Tauc plot, Elliott's model, and Critical Point fitting, were applied to determine the band gaps and the obtained values were compared with each other. The methods were chosen based on the literature: they have previously been applied for similar materials [187–194]. Band gap of CABI has previously been determined to be $1.95\,\mathrm{eV}$ [193] based on Tauc plot and $2.06\,\mathrm{eV}$ [191] (and larger increasing with the decreasing temperature [192]) based on Elliott's model fit, which agreed well with our results including the difference between the methods. Unfortunately, we could not gain more information on the below band gap absorption of CABI, which is arguably the most important question related to the band gap.

In the simulations, sharp step function at the optical band gap of CABI and CBI, respectively, obtained via Tauc plot was applied. The choice was a compromise between the electrical band gap and the absorption onset, and it reflects the uncertainty related to the exact band gap and the nature of the below band gap absorption. The electrical band gap can be speculated to be larger than the optical absorption onset if below band gap absorption would be a result of, for example, shallow trap states close to the conduction band. However, this is not known. If the below band gap absorption would contribute to the photocurrent generation, higher than predicted photocurrents (if the current case underestimates absorption) and/or open circuit voltages (if the current case underestimates the band gap) could be possible, but it is uncertain if this is the case. On the other hand, it is also uncertain how exactly would such states affect, for example, recombination and open circuit voltage, but the effect would likely be negative. Overall, the sharp step function at the optical band gap was considered the most consistent choice based on the current (limited) understanding.

Different computational methods, for example, atomistic and device scale simulations, could further provide insights on the electronic operation of the materials and devices. Firstly, one open question is the origin of the apparent below band gap absorption. Considering the reported atomistic simulations on CABI, which show a considerable partial density of states below the ca. $2\,\mathrm{eV}$ energy level [191; 195], further research on the possible mid-gap and/or tail states and their origin could be interesting. Acknowledging the infamous issue of predicting the band gaps with standard Kohn–Sham density-functional theory [196], application of higher-level theory, for example, hybrid functionals, is considered necessary. Understanding the electronic structure of a material is of key importance in optoelectronic applications. Secondly, device simulations provide a tool to understand and develop the device operation of solar cells [197], among others. Estimation of the loss mechanisms in the reference device would be a natural starting point. For example, transport layer energy levels might be suboptimal considering the wide band gap of the proposed absorbers compared with the typical perovskite absorbers for which the same ETL and HTL are frequently used. Overall, the optical device simulations revealed a large margin between the experimental results (ca. $5-6\%$ PCE) and the obtained optical limit (over 40% PCE) for CABI device under indoor light, which motivates further research on the electronic operation. Optimizing the band offsets may provide a way to significantly improve V_{OC} and the device performance.

5 Heat Generation and Operation Temperature of Perovskite Solar Cells

Solar cells produce heat as a side product in addition to the electricity. Heat generation occurs via different mechanisms as described in Chapter 2. The parasitic heat generation cannot be avoided entirely, at least not in practice, but it is not constant either. Material properties are key factors, which determine the power conversion processes. This chapter starts from the small scale, that is, individual PSCs and the effect of absorber properties (**Publication II**), and continues toward panel scale temperature modelling in varying environmental conditions (**Publication III**). The key questions are, first, how does the perovskite properties affect the heat generation and operation temperature of PSCs, and second, how does the operation temperature of a perovskite panel compare to that of a silicon panel.

5.1 Individual Cells

Publication II studied the self-heating, that is, parasitic heat generation within a cell, of planar PSCs depending on absorber properties, most notably the band gap. The modelled device consisted of a thin-film layer stack of ITO/ETL/perovskite (PVK)/HTL/Au on a glass substrate. The material properties of SnO_2, MAPI, and Spiro-OMeTAD were applied for the ETL, PVK, and HTL layers, respectively. The material properties were artificially varied to study the effect on the heat generation and operation temperature, see **Publication II** Supporting Information. Heat generation mechanisms were explicitly modelled according to the equations (37) - (44) to study the origins of heat production and PCE losses in PSCs. Optics and electrics were modelled as described in Sections 2.3.1 and 2.4.2, respectively.

5.1.1 Perovskite Solar Cell Operation in Varying Temperature

Device operation was first simulated in and around the reference temperature ($25\,^{\circ}\mathrm{C}$) and under the irradiance of $1000\,\mathrm{W/m^2}$ with standard AM1.5G solar spectrum according to the standard testing conditions. The obtained *IV* curves showed typical behaviour under the varying cell temperature (Figure 19a). The most significant change was the decrease of V_{OC} with the increasing cell temperature. MPP shifted to smaller voltages following V_{OC}. J_{SC} and FF also declined, but the changes were

smaller compared with the voltage related values of V_{OC} and MPP. Power-voltage (*PV*) curves contain essentially the same information (Figure 19b).

Voltage dependence of the heat generation in solar cells is less-known (Figure 19c), although it has been previously reported. *QV* curve closely resembled the difference between the maximum heat production and the *PV* curve. The maximum heat production equals to the absorbed irradiance, and it occurred both at $0\,\mathrm{V}$ and at V_{OC} (although, the total heat generation should be lower at V_{OC} due to radiative recombination, which was not included, see discussion below). Remembering the energy balance, which must hold also for different electrical states of a cell, the voltage dependence of the total heat generation is very logical. Still, it is rarely considered.

The most significant changes in the detailed heat generation mechanisms under the voltage scan occurred for the Joule heating and recombination heating (Figure 19d). The Joule heating decreased due to decreasing electric field under the flat current region and eventually with the rapidly decreasing current when the voltage approached V_{OC}. The recombination increased with an accelerating rate toward V_{OC} where it equalled the total photogeneration. Increased recombination rate in higher temperatures was also the reason for the decreasing V_{OC}, see Figure 20. Peltier and heterojunction heats were smaller in magnitude and followed the behaviour of the current. Thermalization and parasitic absorption depend on the optics and were constant under the voltage scan with the fixed cell temperatures.

Figures 19e and 19f summarize the dependence of the total energy components on the cell temperature: power production decreased linearly while the total heat production and reflectance increased linearly as a function of the cell temperature. The change in the reflectance was due to the temperature dependent band gap and optical constants. The temperature dependence of PCE was further divided into its components. Because all IV parameters individually depended linearly on the temperature, it was possible to introduce linear temperature coefficients for each parameter

$$\beta_{\mathrm{x}} = \frac{100\%}{\mathrm{x}(25\,^{\circ}\mathrm{C})}\frac{d\mathrm{x}}{dT}, \tag{51}$$

where x is the chosen parameter (J_{SC}, V_{OC}, FF, or PCE), so that

$$\beta_{\mathrm{PCE}} = \beta_{J_{\mathrm{SC}}} + \beta_{V_{\mathrm{OC}}} + \beta_{\mathrm{FF}}. \tag{52}$$

The temperature coefficients of the IV parameters are given in Table 2.

Table 2. Temperature coefficients of the IV parameters. Adapted from **Publication II** under CC-BY 4.0 licence.

	J_{SC}	V_{OC}	FF	PCE
$\beta\,(\%/\mathrm{K})$	-0.03	-0.21	0.01	-0.23

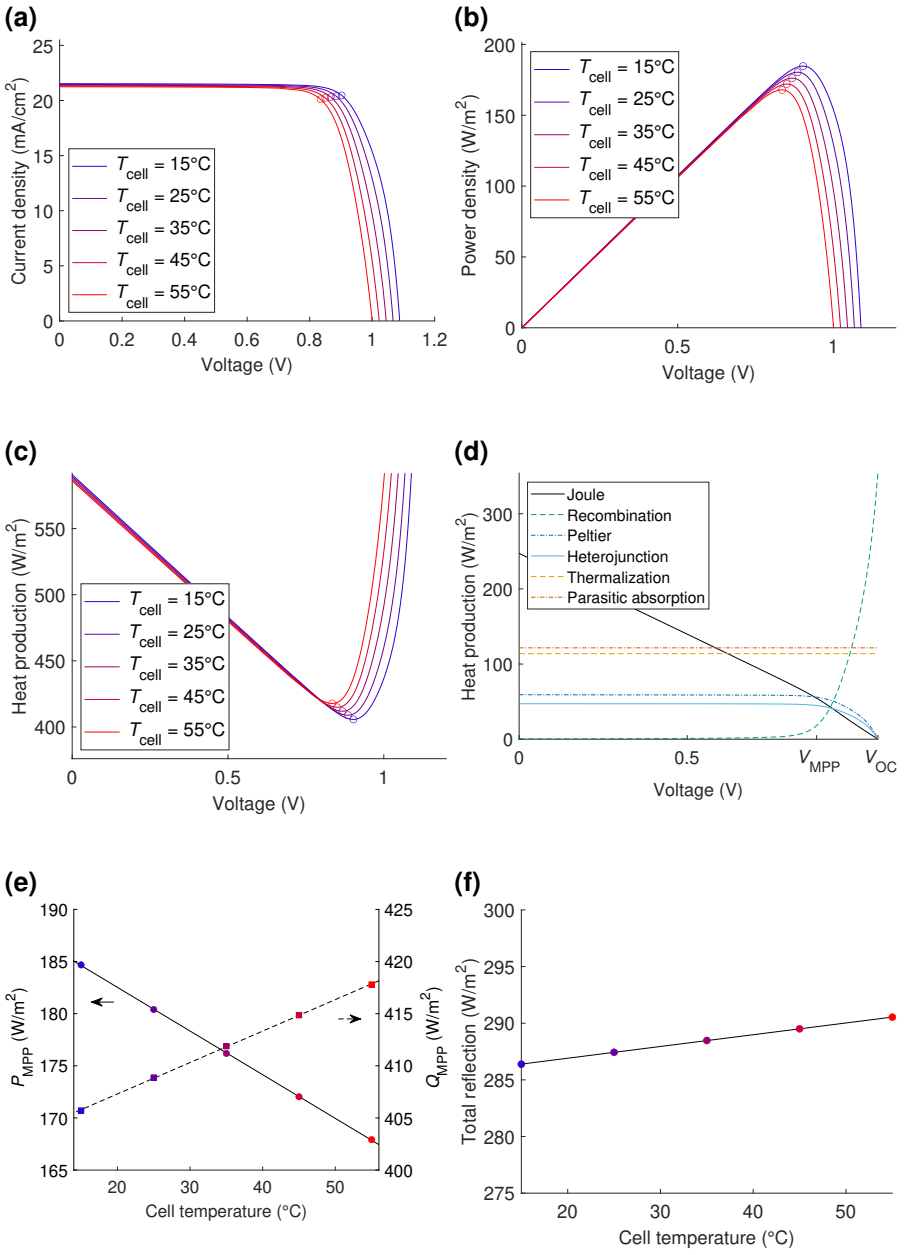

Figure 19. Effect of the temperature on device operation. (a) Current density, (b) power density, and (c) heat production as a function of voltage in varying pre-defined operation temperature. (d) Voltage dependence of the heat generation mechanisms. Temperature was set to $25\,^{\circ}\mathrm{C}$ for these data. (e) Power production, heat production, and (f) reflection at maximum power points as functions of cell temperature. Adapted from **Publication II** under CC-BY 4.0 licence.

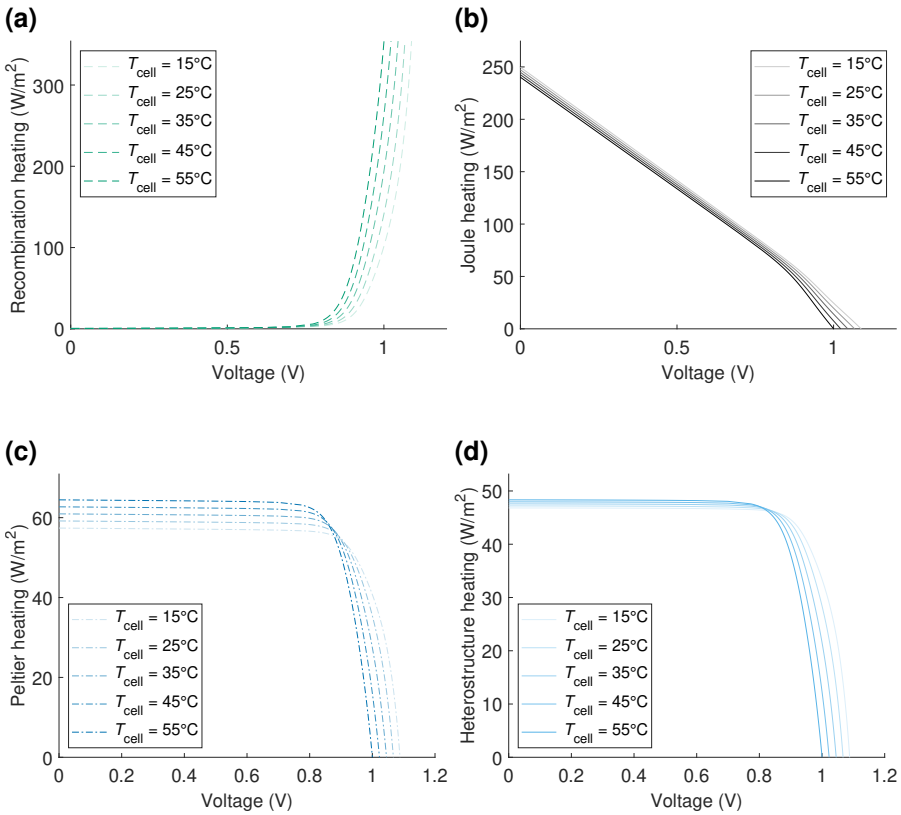

Figure 20. Voltage dependent heat generation mechanisms in different temperatures. (a) Recombination, (b) Joule, (c) Peltier, and (d) heterostructure heating. Data based on **Publication II**.

5.1.2 Absorber Properties Affect the Heat Generation

After gaining knowledge of the reference device operation and different heat mechanisms in varying cell temperature and electrical state, perovskite properties were artificially altered to find how they affect the heat generation. Perovskite band gap was varied from 1.2 to $2.2\,\mathrm{eV}$. HTL band gap was also varied accordingly to maintain the same band offset. The cell temperature was fixed to $25\,^{\circ}\mathrm{C}$. Comparison was conducted for the individual maximum power point of each device.

Heat generation decreased as the absorber band gap increased (Figure 21). The effect was almost linear until $E_\mathrm{g} = 1.8\,\mathrm{eV}$ (Figure 21a). For $E_\mathrm{g} \geq 1.8\,\mathrm{eV}$, the decline of the total heat generation started to saturate. Thermalization decreased most significantly (Figure 21b), which is logical because the band gap defines the upper limit for the extracted energy per each photon while the rest becomes heat. A narrower spectral range, that is, less photons, are also absorbed in the first place with the wider band gaps. Joule heat, recombination heat, Peltier heat, and heterostructure heat, all decreased moderately with the increasing band gap, which related to the decreasing current production. Parasitic absorption was the only heat generation term which increased with the band gap. The increase was due to the stronger absorption of near infrared (NIR) photons in other layers.

Overall, most of the NIR irradiance was reflected away, and an increasing share of the total incident irradiance was reflected as the band gap increased (Figure 21c). Power production as a function of the band gap behaved similarly to the commonly obtained result in the detailed balance calculations: PCE increased from the narrowest band gap towards the optimum after which it declined towards the widest band gaps. The optimum was reached at $1.52\,\mathrm{eV}$, which is larger than typical band gap optima presented in the literature. However, the optimal band gap is known to increase with the increasing share of non-radiative recombination [25].

The total power, which was well conserved in the simulations, was ca. $880\,\mathrm{W/m^2}$ instead of $1000\,\mathrm{W/m^2}$ because of the applied wavelength range of 300 to $1300\,\mathrm{nm}$. This spectral range contains $88\,\%$ of the total irradiance of the standard AM1.5G spectrum while the rest lies in the range of 1300 to $4000\,\mathrm{nm}$. The wavelength range restriction was due to the available optical constant data. The restriction does not affect the power production, but the heat production is likely to be slightly underestimated because a fraction of the infrared irradiation beyond $1300\,\mathrm{nm}$ is probably absorbed in the transport and contact layers as it is absorbed below $1300\,\mathrm{nm}$. A rough estimation of the order of magnitude would be that the parasitic absorption was underestimated by approximately $\gtrsim 20\,\mathrm{W/m^2}$ (ca. 20% of the $120\,\mathrm{W/m^2}$ irradiation that was left out of consideration).

Band gap also affected the temperature coefficients. Relatively smaller temperature coefficient of power production was obtained for larger band gap devices (Figure 21d). It means that larger band gap devices would be more tolerant to temperature

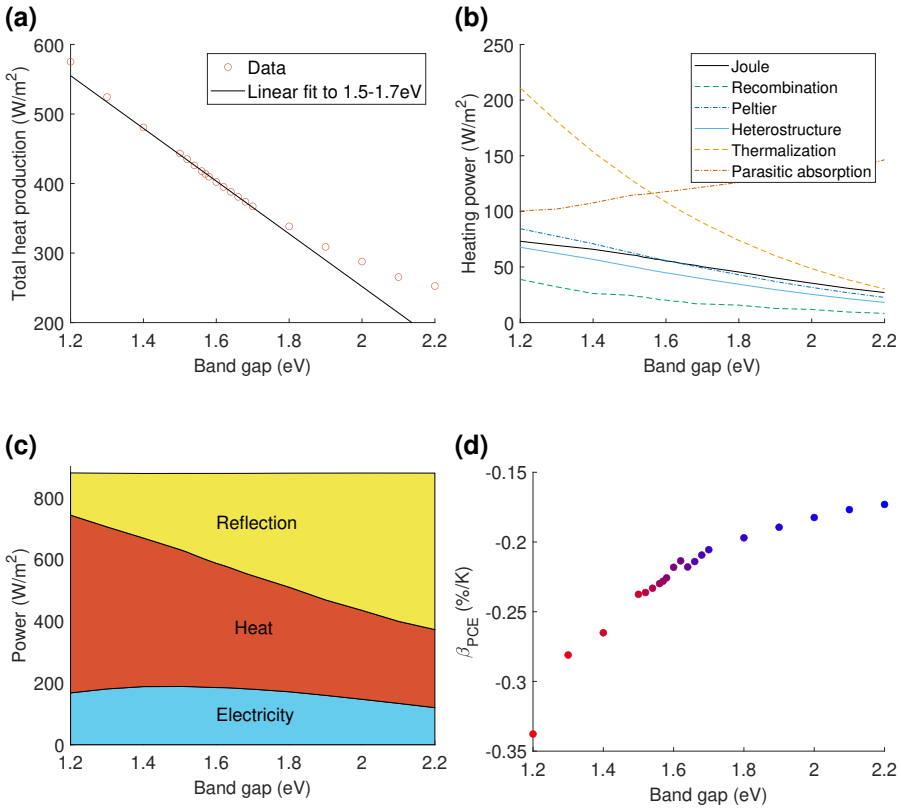

Figure 21. Effect of the band gap. (a) Total heat generation, (b) specific heat generation mechanisms, (c) energy balance and the different components, and (d) temperature coefficient of PCE as functions of the band gap. Adapted from **Publication II** under CC-BY 4.0 licence.

variations. The most important component was $\beta_{V_{\mathrm{OC}}}$, but small changes in $\beta_{J_{\mathrm{SC}}}$ and in β_{FF} were also noticed (**Publication II** Supporting Information).

Bulk trap density of perovskite was also varied. Bulk trap density relates to the transport properties, namely charge carrier lifetimes and subsequently diffusion length (L_{D}). Again, cell temperature was maintained at 25 °C and individual MPPs of each device were compared.

The heat production slightly decreased, and the power production slightly increased for the longer L_{D}, that is, smaller trap density (Figure 22a). The changes originated from smaller Joule heating and smaller recombination heating for the longer L_{D} (see Supporting Information of **Publication II**). Minor increases in Peltier and heterojunction heat were noticed.

The effect of L_{D} strongly links to the optimal perovskite layer thickness (Figure 22b). That is, the longer the diffusion length, the thicker the optimal perovskite thick-

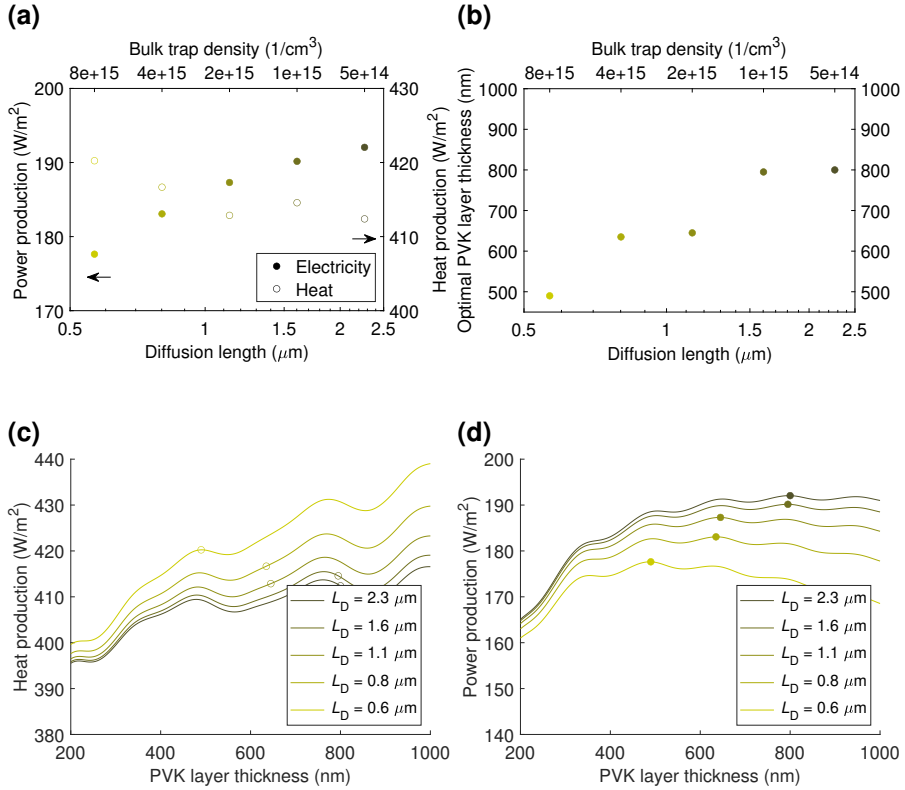

Figure 22. Effect of the bulk trap density and the diffusion length. (a) Power and heat generation as functions of the diffusion length controlled by varying the bulk trap density. (b) The dependence of the optimal perovskite layer thickness on the diffusion length. (c) Heat and (d) power production as a function of perovskite layer thickness with varying diffusion lengths. The diffusion length specific maximum power points are marked with the circles. Adapted from **Publication II** under CC-BY 4.0 licence.

ness. Therefore, the perovskite layer thickness also affects the dependence between the heat and power production and the diffusion length. With a thick perovskite layer, the heat generation would have increased more and the power production decreased more compared to the specific optimal thicknesses (Figures 22c and 22d). On the other hand, smaller effect would have been obtained with a very thin layer. The behaviour connects to the device performance being absorption limited with a thin absorber layer and extraction limited with a thick absorber layer.

The absorber properties (E_g, L_D, and layer thickness) were also varied concurrently (**Publication II** Supporting Information). The effects of the specific parameters were the same as presented above (Figures 21 and 22) independently of the other parameters. No coupled effects were observed.

5.1.3 Outdoor Operation Temperature

Thus far, the effect of the temperature on device operation and the effect of absorber properties on heat generation were studied independently. Both affect the device operation together in realistic outdoor conditions. Example conditions, an ambient temperature of $T_{\mathrm{amb}} = 20\,^{\circ}\mathrm{C}$, irradiance of $1000\,\mathrm{W/m^2}$, and mild wind of $1\,\mathrm{m/s}$, were applied to consider heat exchange with the environment and estimate the actual (steady-state) operation temperatures of PSCs of different band gaps.

The behaviour of the individual T_{cell}-V curves (Figure 23a) was familiar based on the previous QV curve of the reference device (Figure 19c). T_{cell} decreased from $0\,\mathrm{V}$ towards the MPP and increased from MPP to V_{OC} reaching the same level as at $0\,\mathrm{V}$ following the voltage dependence of the heat generation. Self-heating drives the temperature difference compared with T_{amb}, so the resemblance was to be expected. A couple of differences exist: 1) ambient conditions affect the cooling rate via radiative and convective heat exchange with the environment (without additional cooling mechanisms) and 2) the rate of heat transfer depend on the temperature (thermal radiation) and the temperature difference between the cell surface and surrounding air (convection). Therefore, conversion factor from Q to T_{cell} is not constant even for the same weather conditions, but it depends on the absolute cell temperature as well.

Heat generation dependence on the band gap translated to the operation temperature as well (Figures 23a and 23b). The dependence of the operation temperatures at the individual MPPs on the band gap followed from the heat generation (Figure 21a) and the different mechanisms (Figure 21b), which were largely unchanged by the second order effects of the freely varying cell temperature (**Publication II** Supporting Information). Due to the decrease of the total absorption with a wider band gap, the maximum temperature $T_{\mathrm{cell}}(0\,\mathrm{V}) = T_{\mathrm{cell}}(V_{\mathrm{OC}})$ decreased as well, in addition to T_{cell} at MPP (Figure 23a).

Power production at the device specific temperatures was also calculated (Figure 23c). Due to the stronger self-heating and subsequently higher operation temperatures, the maximum power production of the narrow band gap devices differed the most from the estimation at the fixed cell temperature of the STC conditions ($T_{\mathrm{cell}} = 25^{\circ}\mathrm{C}$), as shown in Figure 23d. Minor reduction was observed for wide band gap devices. Even higher difference in power production between T_{STC} and realistic T_{cell} would be expected in higher ambient temperatures because PCE depends on the absolute cell temperature. Altogether, the results highlight the need to consider thermal effects in energy yield modelling.

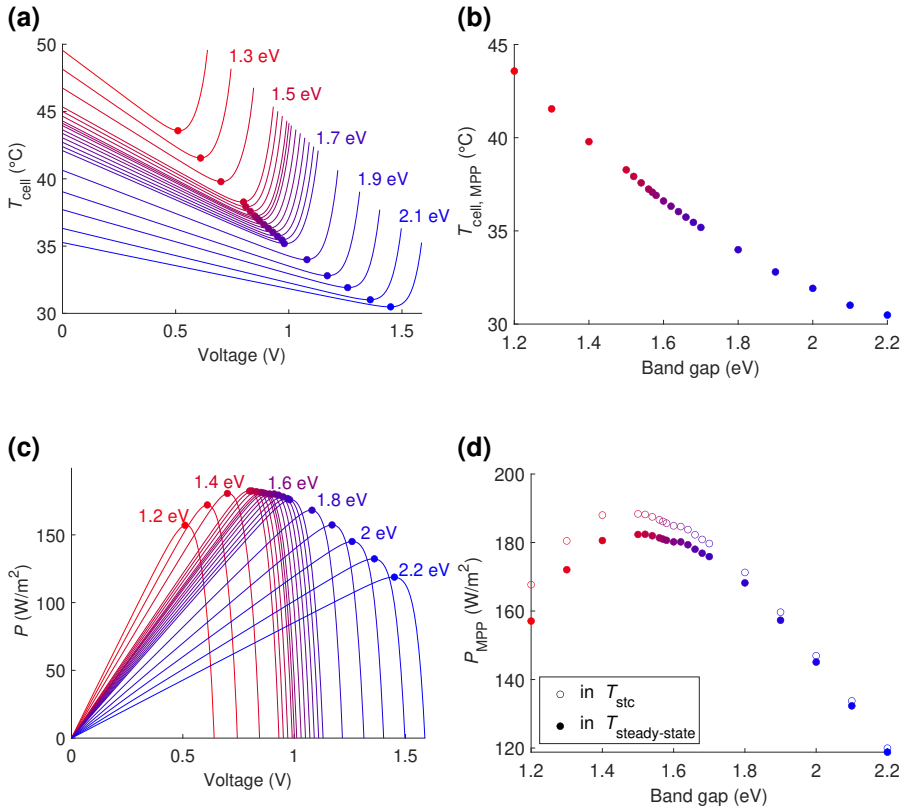

Figure 23. Operation temperature in example outdoor conditions. (a) Cell temperature as a function of the bias voltage for varying perovskite band gaps. The specific maximum power points (filled circles) are marked. (b) Steady-state temperature at the specific MPPs as a function of the band gap. (c) Power production as a function of the bias voltage for varying perovskite band gaps. (d) STC and steady-state power production at the specific MPPs as a function of the band gap. Adapted from **Publication II** under CC-BY 4.0 licence.

5.2 From an Individual Cell to a Panel

Publication III continued on the thermal modelling of PSCs. The size scale was increased from individual cells to a panel and the effect of different weather conditions was considered in more detail. The computationally more efficient energy balance model for heat generation and parametric PCE model for power production were applied. The cheaper models allowed the scale-up to the panel size and enabled studying more combinations of the different weather parameter values.

Comparison with a commercial silicon panel was also conducted, which was inspired by the difference between the band gaps. **Publication II** taught that the band gap is a key factor in heat production, and it was incorporated into the model as

described in Section 2.5.2. In addition, modelling commercial size silicon panels provided an opportunity to validate the model with experimental data and literature, which is much more common for a mature technology like Si-PV. Choices on the panel design and parametric values for the model were made to improve comparability between the panel types when possible. For example, the same number of cells of equal sizes and similar ethylene vinyl acetate (EVA) encapsulation were applied. Model parameters are given in Table 3.

Table 3. Applied model parameters for silicon and perovskite (PVK) panels. Adapted from **Publication III** under CC-BY 4.0 licence.

	$\mathrm{PCE_{ref}}$	$\alpha_{\lambda<\lambda_\mathrm{g}}$	$\alpha_{\lambda\geq\lambda_\mathrm{g}}$	$E_\mathrm{g}(T=25\,^\circ\mathrm{C})$	$V_\mathrm{OC,ref}$	n	β_PCE	$\beta_{E\mathrm{g}}$
Si	$20\,\%$	0.95	0.2	$1.12\,\mathrm{eV}$	0.6	1.3	$-0.35\,\%/\mathrm{K}$	$-0.273\,\mathrm{meV/K}$
PVK	$20\,\%$	0.95	0.2	$1.57\,\mathrm{eV}$	1.1	1.3	$-0.17\,\%/\mathrm{K}$	$0.25\,\mathrm{meV/K}$

Figure 24 illustrates the simulated panel structure and the temperature distributions under the reference conditions of the ambient temperature of $T_\mathrm{amb} = 20°\mathrm{C}$, irradiance of $G = 800\,\mathrm{W/m^2}$, and wind speed of $v_\mathrm{w} = 1\,\mathrm{m/s}$. Predicted line temperature distributions through the panels presented almost $7°\mathrm{C}$ lower temperature for the perovskite cells in operation compared with the silicon cells (Figure 24a). In addition, the heat distributions revealed temperature gradients within the cells (Figures 24a and 24b). Differences within cells were ca. $3°\mathrm{C}$ for PSCs and ca. $4°\mathrm{C}$ for silicon cells. The cells are the heat sources in a panel so it is logical that the temperature decreased in between the cells and towards the panel edges.

Sensitivity analysis was further conducted to study the difference between PVK and Si panel temperatures (Figure 25). As discussed, the different band gaps mean that typical PSCs (of ca. $1.6\,\mathrm{eV}$) absorb less but utilize the absorbed energy more efficiently compared with silicon leading to the lower self-heating and operation temperature. However, the assumption of 20% below band gap absorption in both panels (see equation (26) and Table 3) does not need to hold in general, despite being reasonable based on the literature. Therefore, $\alpha_{\lambda\geq\lambda_\mathrm{g}}$ was varied to study the dependence of the results on the assumption. $\alpha_{\lambda\geq\lambda_\mathrm{g}}$ indeed affected the temperature prediction notably, but it did not change the outcome that the perovskite panel was estimated to operate in a lower temperature.

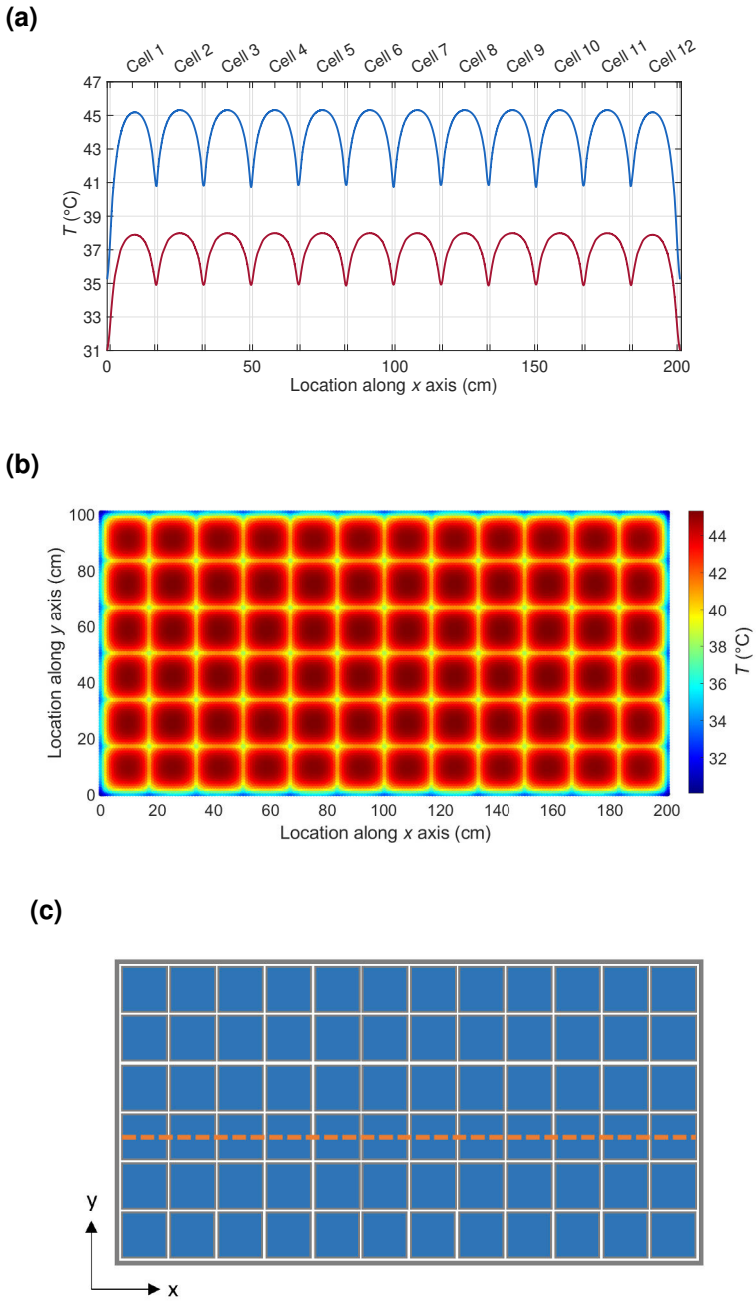

Figure 24. Temperature distribution over a panel area. (a) Temperature of silicon (blue) and perovskite (red) panels along a line cut (presented in panel c). (b) Temperature distribution of the silicon panel presented as a two-dimensional heat map. (c) Illustration of the panel geometry. Adapted from **Publication III** under CC-BY 4.0 licence.

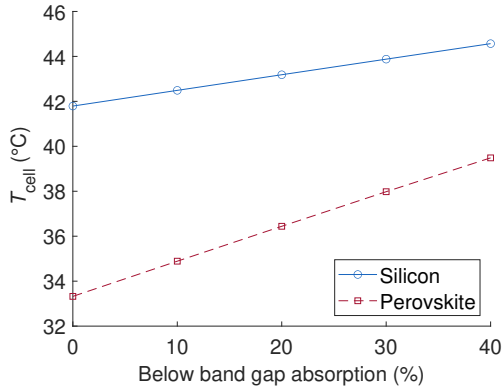

Figure 25. Sensitivity analysis of the model. Simulated cell temperatures as functions of the below band gap absorption coefficient. Adapted from **Publication III** under CC-BY 4.0 licence.

5.2.1 Effect of the Weather

Ambient temperature, irradiance and wind speed were computationally varied to study the panel temperatures in varying conditions. One parameter was altered at a time and others were kept constant ($T_{\mathrm{amb}} = 20°\mathrm{C}$, $G = 800\,\mathrm{W/m^2}$, $v_{\mathrm{w}} = 1\,\mathrm{m/s}$) unless mentioned otherwise. Quasi-linear dependence on the ambient temperature and irradiance, respectively, was observed for the panel temperature (Figures 26a and 26b). T_{amb} acts as the baseline from where the heat production within the cells increases the panel temperature. Irradiance, on the other hand, is the initial source of the energy. Device operation is not strictly linear causing non-linearity in the heat generation as well, but the non-linear effects were small under the modelled range. Wind speed affects the temperature via convective heat transfer. Convection coefficient increases linearly as a function of the wind speed. However, saturating temperature decay with the increasing wind speed was observed, which was due to the temperature difference component of the convection. That is, convection declines as the temperature difference between the panel surface and the ambient air decreases.

All condition parameters were varied at once to find the ”full” temperature range under normal operation. Especially, the upper limit of the cell temperature in a hot environment and under intense irradiance may be interesting due to the thermal stability concerns of perovskites. The maximum observed panel temperature (at $T_{\mathrm{amb}} = 40°\mathrm{C}$, $G = 1200\,\mathrm{W/m^2}$, $v_{\mathrm{w}} = 0\,\mathrm{m/s}$) was almost $70°\mathrm{C}$. Warmer ambient temperatures may occur, but the result gives an order of magnitude for the highest cell temperatures under normal operation. Even higher cell temperatures could be encountered under exceptional operation, which cause hot-spots.

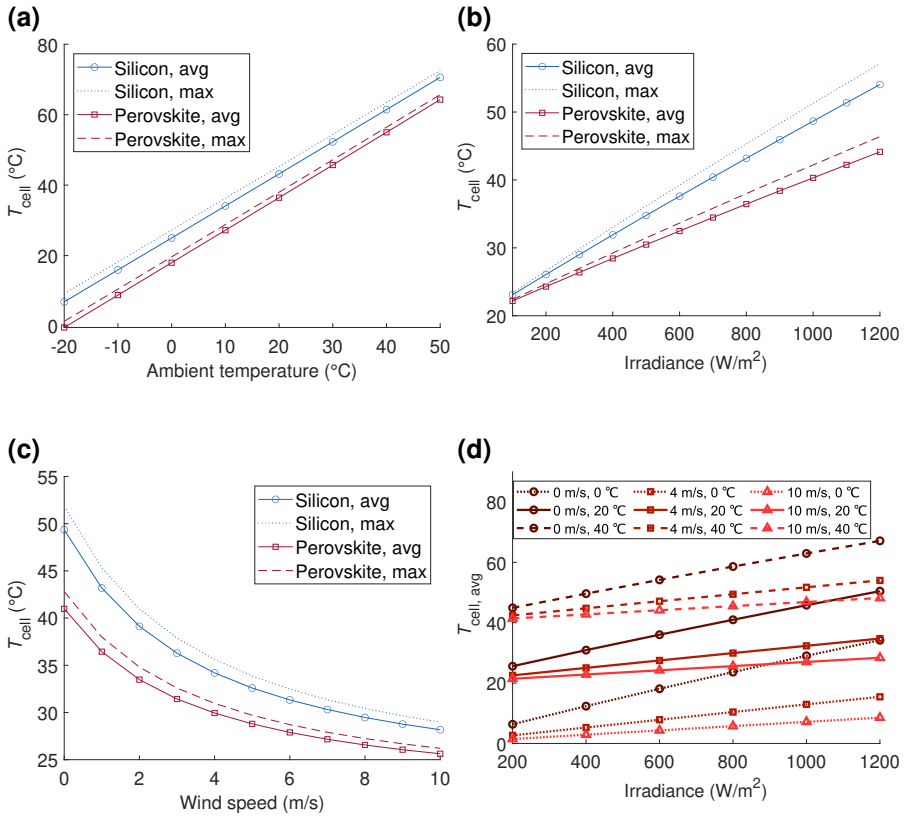

Figure 26. Effect of the ambient conditions on the operation temperature. Simulated operation temperatures as functions of varying (a) ambient temperature, (b) irradiance level, and (c) wind speed. One condition parameter was varied at a time. (d) Combined effects of the conditions on the average perovskite cell temperature. The average was taken over all the cells in a panel as illustrated in Figure 24c. Adapted from **Publication III** under CC-BY 4.0 licence.

5.2.2 Parameters for Fast Panel Temperature Modelling

The simulated panel temperatures in varying conditions allowed to fit semi-empirical module temperature models into the simulated data. The semi-empirical temperature models are simple mathematical formulae, which provide the module temperature based on the weather variables. All the processes of the internal heat production and heat transfer from the panel are represented as empirical model parameters. Several semi-empirical module temperature models exist, such as Sandia, Faiman, PVsyst, Mattei, and TRNSYS. They are commonly used for modelling the silicon panel temperatures in power production simulations thanks to the easy use and fast computation. However, the model parameters are specific to the panel characteristics. Therefore, a set of perovskite-specific model parameters was predicted based

on the simulations (Table 4) to enable the fast temperature and power prediction simulations for perovskite panels similar to those of commercial silicon solar panels.

Table 4. Panel temperature model parameters based on computationally simulated temperature data. Adapted from **Publication III** under CC-BY 4.0 licence.

	Sandia	Faiman	PVsyst	Mattei	TRNSYS
Slope	-0.129	$10.47\,\mathrm{Ws/m^3K}$	$5.27\,\mathrm{Ws/m^3K}$	$4.49\,\mathrm{Ws/m^3K}$	$4.54\,\mathrm{Ws/m^3K}$
Intercept	-3.77	$37.93\,\mathrm{W/m^2K}$	$19.29\,\mathrm{W/m^2K}$	$16.65\,\mathrm{W/m^2K}$	$16.38\,\mathrm{W/m^2K}$

5.3 Discussion on the Thermal Studies

Quantitative heat generation and operation temperature predictions for perovskite cells as a function of the absorber properties, namely band gap, diffusion length, and layer thickness, were computed. The study was extended to a commercial-sized panel, and the perovskite panel temperatures in varying conditions were compared with those of a silicon panel. The absorber band gap was found especially significant parameter for the device temperature when comparing well-functioning devices. Accurate prediction of operation temperatures is important for energy yield estimation.

The observed band gap dependence agrees with the literature [51; 53; 62; 198]. The novelty of the **Publication II** was the concrete thermal modelling of PSCs with strictly defined material properties and structure parameters, which allowed quantitative predictions on the operation temperature. **Publication III** further predicted perovskite-specific model parameters for common semi-empirical panel temperature models, which allow easy and fast temperature modelling for a wider user base.

Energy conservation is a mundane fact in classical physics, but it deserves some attention in the context of **Publication II**. All the different heat mechanisms, power production and optics, including absorption, reflection and transmission, were 'independently' defined, where independent means that all the applied equations were obtained from relevant theory instead of assuming the energy conservation. Therefore, the observed energy conservation serves to prove the self-consistency of the applied methods and the adequate numerical accuracy of the computations.

Despite the self-consistency, which is a merit on its own, the model however was not complete in the sense that it did not include all the physical phenomena in PSCs. One example is the radiative recombination. Radiative recombination does not produce heat, but it affects the energy balance. Indeed, radiative recombination reduces the self-heating because out-coupled emission would cool down the device similar to other radiative heat transfer. Because radiative (like non-radiative) recombination increases with the voltage, the effect would be seen especially close to V_{OC}. The magnitude of the effect of radiative recombination on the total heat generation depends on the ratio between the radiative and non-radiative recombination rates. However, the effect is already much smaller for MPP, which was the focus in

Publication II. As shown in Figure 19d concerning the voltage dependence of the specific heat generation mechanisms, (non-radiative) recombination is the smallest of the heating (/loss) mechanisms.

A related process is photon-recycling [199–202], which means the (re-)absorption of the emitted photons from radiative recombination. Interestingly, photon-recycling increases the open circuit voltage of PSCs [200] and reduces the effective (external) radiative recombination [201; 202]. Therefore, the effect on the heat generation is opposite than that of the radiative recombination. Photon-recycling counteracts the reduction in self-heating due to the radiative recombination because it decreases the out-coupling of emitted photons and effectively increases the ratio of non-radiative against the radiative recombination. However, it is good to note that these two processes are not only competing with each other, but they also have a combined effect on the optoelectronic operation of PSCs. It would be good to include both in the model for the possible future research.

Another deficiency in **Publication II** is that mobile ions were not included in the simulations. Ion mobility is a distinct feature of perovskites compared with, for example, elemental semiconductors like silicon, as described in Section 2.2. It means that ions in the bulk perovskite crystal can migrate within the crystal structure, and form a gradient in the ion density across the material layer. Temperature affects the ion mobility, and the ion migration may affect the temperature coefficients of PSCs, for example. However, the effects on the temperature coefficients are estimated to be relatively small because the observed temperature coefficients already agreed quite well with the experimental reports [60; 203–205]. The lack of mobile ions might explain the small difference between the predicted β_{PCE} and the experiments, and if so, the inclusion of mobile ions could further improve the prediction, but it should not significantly change it.

Considering the energy balance, that is, the interdependence of electricity and heat productions, all changes in the device model, which affect the simulation of electric operation, also affect the simulation of heat production. That includes the mobile ions. However, it should be noted that the focus was on the steady-state operation. Ion mobility especially affects the transient device operation, like hysteresis and temperature-dependent hysteresis [206; 207].

Long term effects, for example, degradation, on the other hand, would be a totally different case. However, all time evolution was out of the scope. The thermal effects of degradation would make an interesting research topic for the future.

Further improvement in **Publication II** could be to consider temperature dependence of $\sim$all material properties. Perovskite band gap and charge carrier mobility were modelled as functions of temperature, but in addition to those, many others, for example, transport layer energy levels, could depend on the cell temperature and affect the thermal effects in PSCs. In the case of ETL and HTL, the conduction (valence) band offset of ETL (HTL) and the perovskite is probably more interesting

than the exact transport layer band gap. Despite the fact that some temperature dependent properties may have been modelled as constants, the main characteristics of PSC temperature effects are considered to be well covered in **Publication II**. The effect of additional temperature dependencies would probably concern the temperature coefficient, which was close to the experiments as discussed above.

More focus on the interfacial trap density and recombination could also be placed. Local trap density was defined to consider the interfacial recombination, and the trap density increased toward the interfaces. However, the effect of the interface trap densities were not studied while the bulk trap density was varied. Interfacial recombination is typically more interesting than the bulk recombination in state of the art PSCs. Focusing on the interfacial trap density and interface passivation could also be interesting from the thermal point of view. This would expand the study, but not change the obtained results.

One aspect worth highlighting is the temperature coefficient of power production, which was modelled in **Publication II** and has also been measured in the literature [60; 203–205] to be much smaller for PSCs compared with the Si cells [160]. In practice, solar cells operate at elevated temperatures and the smaller temperature coefficient allows the cell to maintain a higher PCE in the increased operating temperatures. That means that there are two individual factors in favour of larger band gap devices from the thermal effect point of view: large band gap cells generate less heat, and they possess lower temperature coefficients. Indeed, large band gap devices, including PSCs, have been proposed to have advantage over Si cells in hot climates [208].

Interestingly, perovskites have also shown very low thermal conductivity [169]. The effect of the low thermal conductivity of MAPI on the effective thermal conductivity of a reference PSC and further on the panel temperature distribution was considered in **Publication III** (Supporting Information). Geometrically, there are two different cases to study: thermal conduction through the PSC in perpendicular and parallel directions with respect to the cell surface. Based on the supporting calculations, which were conducted for **Publication III**, it seemed that the effect of low thermal conductivity of the perovskite averaged out due to the thin layer (in the perpendicular case) and due to the high thermal conductivity of the contact materials (in the parallel case). That is, even if the temperature gradient is high within the perovskite layer, the absolute temperature difference between the top and bottom surfaces of the PVK layer is rather small due to the short distance. On the other hand, contact materials (especially Au, but also FTO) conduct heat so efficiently that they prevent the accumulation of heat along the larger dimensions of a cell or panel. This inference is based on the assumption of negligible thermal resistance at the interfaces. If the thermal resistance at interfaces would be significant, the low thermal conductivity would be expected to have a more important role in the temperature distribution within PSCs. Further, heat could accumulate in perovskite layer and the

operating temperature of perovskite itself could be elevated compared to the other panel materials.

Publication III showed that computational simulation offers a pathway to study the cell temperature of novel devices in varying outdoor conditions. Outdoor testing is valuable, but it is slow, and simulations can provide insights to support the experiments. System characteristics can also be changed to predict the effects. A possibility for future research may be to study exceptional operation, for example, formation of hot spots.

While the panel configuration was defined as presented to maximize comparability with the silicon panel, perovskite panels commonly consist of rectangular PSCs instead of the almost square-cells like silicon panels. The geometry may affect the cell temperature, although the effect is expected to be limited. However, the geometry would be expected to affect the temperature distribution: the temperature notably decreased toward the inactive areas in between the cells, as presented in Figure 24. A study of the panel geometry and the related thermal effects may be of interest for building integrated photovoltaics.

Future research, in addition to the suggested ones and apart from improving the model(s) and accuracy, can include, for example, application of the models to different cell types, such as multi-junction (or tandem) cells. Device optimization considering the ambient conditions may also be of interest. Overall, the temperature of the cells is typically a second order effect, which influences the performance, but it is a significant one, and it should be routinely considered.

6 Structure Optimization of Perovskite Solar Cells

In addition to the materials (and their properties), the device structure significantly affects the solar cell performance (both PCE and stability, in general, but only PCE is considered here). **Publication IV** conducted optical and optoelectronic simulations of a planar PSC with varying layer thicknesses. The focus was on the dependence of the optimal layer thickness of the perovskite absorber on other layer thicknesses.

6.1 Optimization of Layer Thicknesses in the Planar Device Structure Based on Interference

The applied optical figure of merit was the maximum achievable photocurrent (MAPC), which is obtained from the normalized absorption by multiplication and integration over an incident irradiance spectrum and the elementary charge. (Note that MAPC is the exactly same metric as the integrated maximum achievable photocurrent $\mathrm{Int.}\, J_{\mathrm{ph}}$ earlier in chapter 4, but MAPC is used here in this chapter to maintain the terminology of the original **Publication IV**). HTL thickness was observed to affect the local optima of absorber thickness, that is, the absorber thickness to provide the peak MAPC depended on the HTL thickness (Figure 27a). The global MAPC maximum was always obtained at the edge of the search space: absorption increases with the increasing thickness despite the absolute increment decreasing and becoming insignificant at the same time. The interesting correlation between layer thicknesses and the oscillating behaviour of MAPC as a function of the thicknesses originates from the interference of the forward propagating and backward propagating local optical electric fields. The backward propagation arises from the reflection of light from the material interfaces below the absorber. The HTL thickness affects the phase of the reflected optical electric field and the interference, which further affects MAPC and gives rise to the correlated layer thickness optima of the absorber and HTL.

Including the device electrics and considering the finite charge extraction naturally constrained the global PCE maximum in contrast to the persistent increase of MAPC with the increasing absorber thickness (Figures 27b and 27c). Only minor shift toward thinner absorber layers was noticed in the local thickness optima. However, the change in the global PCE optimum makes the consideration of electrical operation necessary.

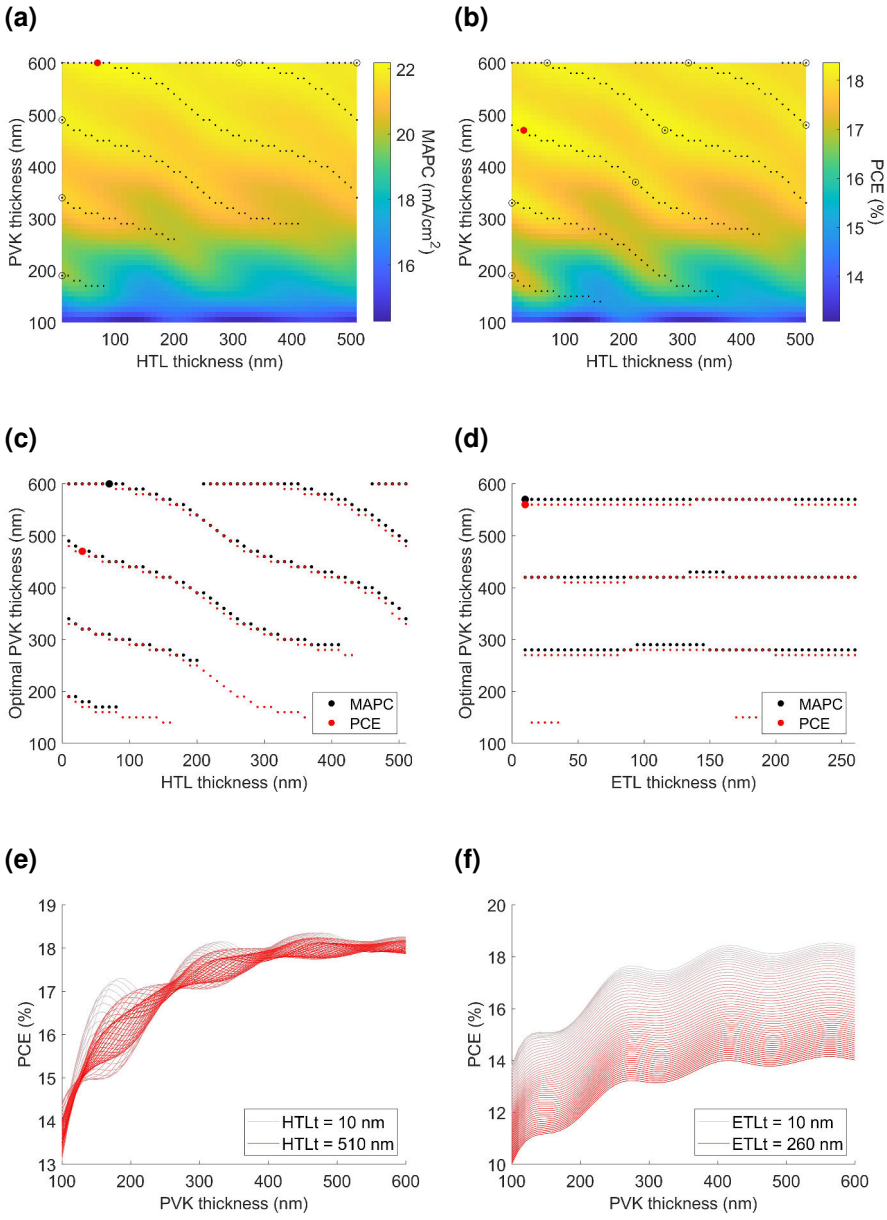

Figure 27. Optical and optoelectronic thickness optimization. (a) Maximum achievable photocurrent and (b) power conversion efficiency as a function of perovskite and hole transport layer thicknesses. Local maxima for each HTL thickness separately (dots) and for both, perovskite and HTL, thicknesses (circles) as well as the global maximum within the search space (red filled circle) are presented. (c,d) Optimal perovskite layer thicknesses as a function of HTL (panel c) and ETL (d) thickness. Local (dots) and global (filled circles) optima are presented. Figure parts (a-d) reproduced with permission (**Publication IV**), copyright WIP Renewable Energies. (e,f) PCE as a function of PVK thickness for varying HTL (e) and ETL (f) thicknesses. (e) ETL thickness of 35 nm and (f) HTL thickness of 160 nm were applied for this data. Data based on **Publication IV**.

ETL thickness was noticed insignificant for the local absorber thickness optima by both optical and optoelectronic approaches (Figure 27d). Local absorber optima were practically constant and the thinnest ETL provided the smallest parasitic absorption and subsequently the largest MAPC and PCE. In addition to the ETL thickness independent absorber thickness, the correlated behaviour between the absorber and HTL thickness optima was purely optical, and the recombination only depended on the absorber thickness.

Despite the focus on the optimal layer thicknesses and their correlation(s), it is good to note the order of magnitude in the actual performance (see Figures 27e and 27f). While HTL thickness affected the PVK thickness of peak performance, the effect on PCE was small (Figure 27e). On the other hand, despite the fact that ETL thickness did not affect the optimal PVK thickness, the effect of ETL thickness on the absolute PCE value was significant (Figure 27f). A thin ETL layer is important for minimizing parasitic absorption in the front transport layer.

6.2 Discussion on the Structure Optimization

Absorber and HTL thickness optima were found to correlate with each other. However, the correlation was found to originate entirely from the optical interference, which was affected by the back side transport layer thickness, HTL in this case. Because no electrical effect on the correlation was found, it was inferred that the type of the transport layer, HTL or ETL, would not matter for the correlation. Thus, similar effect should be observed between ETL and absorber layer thicknesses in a planar device with the inverted configuration.

The strength of the back propagation is expected to determine the level of the correlation. That is, if a transparent back electrode was applied, instead of a metallic one, the correlation may disappear. In addition, the interference depends on the coherence of light. Therefore, scattering, for example, due to rough interface morphology, may cause the correlation in the optimal thicknesses to vanish. Further, the optima are likely to depend on the incidence angle because the angle changes the optical path length within the layers as well as the layer thicknesses do. These aspects make it hard, in practice, to utilize the interference based thickness optimization in real device and outdoor conditions.

The concept of optimizing coupled variables is still considered very interesting. Device structure here was arguably the simplest one. However, different device structures may emerge, such as point contacts [76] as inspired by the PERC structure of silicon solar cells. With a more complex device design, structure optimization of coupled design parameters may provide more significant and practical benefits.

7 Conclusions

The objective of the thesis was to improve understanding of the perovskite solar cell operation in different realistic and application specific conditions, including indoor and varying outdoor conditions. Computational device level simulations, including optical, electrical, and thermal modelling, were conducted to study the questions. In addition, spectroscopic ellipsometry supported by atomic force microscopy was applied for the optical characterization of novel absorber materials for indoor photovoltaics.

In **Publication I**, the optical constant spectra of two bismuth-based perovskite-inspired materials were measured. The data were applied to calculate the optical photocurrent and radiative limit power conversion efficiency limits. High optical limits for the performance metrics (for example, over 40% PCE with CABI absorber) were obtained based on the simulations, which applied the experimentally determined optical properties. However, there is a large margin between the current experimental results (ca. 5-6% PCE) and the maximum theoretical efficiency of a corresponding ideal solar cell (approximately 50% PCE). The results indicate that the optics are not the limiting factor in the device operation because the calculated optical limit is close to the theoretical limit. Further, the produced optical constants enable to continue to the optoelectronic device simulations, which may explain the performance limitations and how to defeat them. In the broader context, IPV applications are a topical research line among emerging photovoltaics, and they present a highly promising pathway for the commercialization of perovskite and perovskite-inspired materials.

Publication II simulated PSCs with varying perovskite properties to study the related thermal effects. Quantitative predictions on the heat generation, operation temperature, and their effects on the power conversion efficiency of PSCs were produced. Band gap was found to affect the heat generation significantly. Heat generation within the cell decreases almost linearly with a slope of ca. $-0.4\,\mathrm{W/(m^2\,meV)}$ under the typical band gap range (below $1.7\,\mathrm{eV}$). Further application of the methods and results of **Publication II** enable thermal analysis of related technologies, for example, other thin film and multi-junction solar cells or even other perovskite-based optoelectronics in general.

Publication III continued the research by simulating the operation temperature of perovskite panels in varying weather conditions. The operation temperature of the modelled perovskite panel was found to be ca. $7\,^{\circ}\mathrm{C}$ lower than that of the compa-

rable silicon panel in the reference conditions. The simulated temperature data in varying conditions allowed to fit semi-empirical panel temperature models and find perovskite-specific model parameters for fast temperature estimation. The parameters enable a wider group of solar engineers to predict the operation temperature of perovskite panels with common energy yield simulation tools. Accurate power production prediction is important for the different stakeholders of energy systems, such as grid operators and investors, and temperature estimation improves the accuracy.

Publication IV presented optoelectronic simulations of a planar PSC. Local and global thickness optima for several functional layers, including the transport layers and the absorber, were obtained. While the practical benefit of the results may be limited due to the discussed reasons (for example, varying incidence angle and scattering at the interfaces), the concept of the structure optimization is envisioned to produce interesting insights in future research, that is, if more complex device structures are adopted.

Overall, perovskites and perovskite-inspired materials present a highly promising and versatile group of materials for optoelectronic applications, including solar cells. Future research can apply device level modelling to study different questions or combine the applied tools with experiments and/or different computational methods of smaller length and time scales. Especially the combination of multiscale modelling and experiments is considered highly intriguing. It is argued that the theoretical understanding and computational tools start to approach a level where device level operation can be simulated starting from and almost solely based on first principles, when different computational models are combined and applied to complement each other. In principle, DFT and ”beyond-DFT” methods can predict all the information (that is, material properties) required by continuum models, such as drift-diffusion model, which can further describe device level operation (nowadays also in more than one dimensions, which may be important in some cases). Further about combining the modelling and experiments, computational optimization can also be applied to fit the computational model(s) and the experiments together, in addition to the traditional optimization of device performance. For example, a computational model can be ”optimized” with respect to an unknown or uncertain parameter to find the value, which replicates an experimental observation by minimizing an object function that describes the difference between the modelled and measured data. The accuracy of the described multiscale modelling may still be low in some cases, but the accuracy continues to increase as the available computation power increases and computationally more efficient methods are developed. Such approach, if accurately realized, could find broad use in PSC research and development, and maybe even in some other applications as well.

List of References

[1] NASA, "Global temperature - earth indicator." https://science.nasa.gov/earth/explore/earth-indicators/global-temperature/, 2026. Accessed 2026-01-22.

[2] H. Ritchie and P. Rosado, "Fossil fuels," *Our World in Data*, 2017. https://ourworldindata.org/fossil-fuels. Accessed 2026-01-22.

[3] R. Perez and M. Perez, "A fundamental look at energy reserves for the planet," *The International Energy Agency SHC Programme Solar Update*, vol. 50, pp. 2–3, 2009.

[4] S. Hegedus and A. Luque, "Achievements and challenges of solar electricity from photovoltaics," in *Handbook of Photovoltaic Science and Engineering*, ch. 1, pp. 1–38, John Wiley & Sons, Ltd, 2010.

[5] IEA, "World energy outlook 2025." https://www.iea.org/reports/world-energy-outlook-2025, 2025. Accessed 2026-01-22.

[6] IEA, "Global energy review 2025." https://www.iea.org/reports/global-energy-review-2025, 2025. Accessed 2025-12-16.

[7] A. Kojima, K. Teshima, Y. Shirai, and T. Miyasaka, "Organometal halide perovskites as visible-light sensitizers for photovoltaic cells," *Journal of the American Chemical Society*, vol. 131, no. 17, pp. 6050–6051, 2009.

[8] M. M. Lee, J. Teuscher, T. Miyasaka, T. N. Murakami, and H. J. Snaith, "Efficient hybrid solar cells based on meso-superstructured organometal halide perovskites," *Science*, vol. 338, no. 6107, pp. 643–647, 2012.

[9] A. K. Jena, A. Kulkarni, and T. Miyasaka, "Halide perovskite photovoltaics: Background, status, and future prospects," *Chemical Reviews*, vol. 119, no. 5, pp. 3036–3103, 2019.

[10] J. Y. Kim, J.-W. Lee, H. S. Jung, H. Shin, and N.-G. Park, "High-efficiency perovskite solar cells," *Chemical Reviews*, vol. 120, no. 15, pp. 7867–7918, 2020.

[11] A. Rogalski, F. Wang, J. Wang, P. Martyniuk, and W. Hu, "The perovskite optoelectronic devices – a look at the future," *Small Methods*, vol. 9, no. 1, p. 2400709, 2025.

[12] E. L. Unger, L. Kegelmann, K. Suchan, D. Sörell, L. Korte, and S. Albrecht, "Roadmap and roadblocks for the band gap tunability of metal halide perovskites," *J. Mater. Chem. A*, vol. 5, pp. 11401–11409, 2017.

[13] A. Walsh, "Principles of chemical bonding and band gap engineering in hybrid organic–inorganic halide perovskites," *The Journal of Physical Chemistry C*, vol. 119, no. 11, pp. 5755–5760, 2015.

[14] L. D. Whalley, J. M. Frost, Y.-K. Jung, and A. Walsh, "Perspective: Theory and simulation of hybrid halide perovskites," *The Journal of Chemical Physics*, vol. 146, no. 22, p. 220901, 2017.

[15] P. Lopez-Varo, J. A. Jiménez-Tejada, M. García-Rosell, S. Ravishankar, G. Garcia-Belmonte, J. Bisquert, and O. Almora, "Device physics of hybrid perovskite solar cells: Theory and experiment," *Advanced Energy Materials*, vol. 8, no. 14, p. 1702772, 2018.

[16] Fraunhofer ISE, "Photovoltaics report." https://www.ise.fraunhofer.de/en/publications/studies/photovoltaics-report.html, 2025. updated: 31 October 2025, Accessed 2026-01-22.

[17] A. W. Blakers, A. Wang, A. M. Milne, J. Zhao, and M. A. Green, "22.8% efficient silicon solar cell," *Applied Physics Letters*, vol. 55, no. 13, pp. 1363–1365, 1989.

[18] T. Dullweber and J. Schmidt, "Industrial silicon solar cells applying the passivated emitter and rear cell (PERC) concept—a review," *IEEE Journal of Photovoltaics*, vol. 6, no. 5, pp. 1366–1381, 2016.

[19] M. Green, F. King, and J. Shewchun, "Minority carrier MIS tunnel diodes and their application to electron- and photo-voltaic energy conversion—I. Theory," *Solid-State Electronics*, vol. 17, no. 6, pp. 551–561, 1974.

[20] F. Feldmann, M. Simon, M. Bivour, C. Reichel, M. Hermle, and S. W. Glunz, "Carrier-selective contacts for Si solar cells," *Applied Physics Letters*, vol. 104, no. 18, p. 181105, 2014.

[21] M. Tanaka, M. Taguchi, T. Matsuyama, T. Sawada, S. Tsuda, S. Nakano, H. Hanafusa, and Y. Kuwano, "Development of new a-Si/c-Si heterojunction solar cells: ACJ-HIT (artificially constructed junction-heterojunction with intrinsic thin-layer)," *Japanese Journal of Applied Physics*, vol. 31, no. 11R, p. 3518, 1992.

[22] H. Lin, M. Yang, X. Ru, G. Wang, S. Yin, F. Peng, C. Hong, M. Qu, J. Lu, L. Fang, C. Han, P. Procel, O. Isabella, P. Gao, Z. Li, and X. Xu, "Silicon heterojunction solar cells with up to 26.81% efficiency achieved by electrically optimized nanocrystalline-silicon hole contact layers," *Nature Energy*, vol. 8, no. 8, pp. 789–799, 2023.

[23] IRENA, "Renewable power generation costs in 2024." https://www.irena.org/-/media/Files/IRENA/Agency/Publication/2025/Jul/IRENA_TEC_RPGC_in_2024_2025.pdf, 2025. Accessed 2026-01-22.

[24] Lazard, "Lazard's levelized cost of energy+ (lcoe+)." https://www.lazard.com/research-insights/levelized-cost-of-energyplus-lcoeplus/, 2025. Accessed 2026-01-27.

[25] W. Shockley and H. J. Queisser, "Detailed balance limit of efficiency of p-n junction solar cells," *Journal of Applied Physics*, vol. 32, no. 3, pp. 510–519, 1961.

[26] NREL, "Best research-cell efficiency chart." https://www.nrel.gov/pv/cell-efficiency, 2025. Accessed 2026-01-22.

[27] T. E. Kuhn, C. Erban, M. Heinrich, J. Eisenlohr, F. Ensslen, and D. H. Neuhaus, "Review of technological design options for building integrated photovoltaics (BIPV)," *Energy and Buildings*, vol. 231, p. 110381, 2021.

[28] Z. Li, T. Ma, H. Yang, L. Lu, and R. Wang, "Transparent and colored solar photovoltaics for building integration," *Solar RRL*, vol. 5, no. 3, p. 2000614, 2021.

[29] T. M. Koh, H. Wang, Y. F. Ng, A. Bruno, S. Mhaisalkar, and N. Mathews, "Halide perovskite solar cells for building integrated photovoltaics: Transforming building façades into power generators," *Advanced Materials*, vol. 34, no. 25, p. 2104661, 2022.

[30] M. Ben Said-Romdhane and S. Skander-Mustapha, "A review on vehicle-integrated photovoltaic panels," in *Advanced Technologies for Solar Photovoltaics Energy Systems* (S. Motahhir and A. M. Eltamaly, eds.), pp. 349–370, Cham: Springer International Publishing, 2021.

[31] M. Yamaguchi, K. Nakamura, R. Ozaki, N. Kojima, Y. Ohshita, T. Masuda, K. Okumura, A. Satou, T. Nakado, K. Yamada, T. Tanimoto, Y. Zushi, T. Takamoto, K. Araki, Y. Ota, and K. Nishioka, "Analysis for the potential of high-efficiency and low-cost vehicle-integrated photovoltaics," *Solar RRL*, vol. 7, no. 8, p. 2200556, 2023.

[32] A. S. R. Bati, Y. L. Zhong, P. L. Burn, M. K. Nazeeruddin, P. E. Shaw, and M. Batmunkh, "Next-generation applications for integrated perovskite solar cells," *Communications Materials*, vol. 4, no. 1, p. 2, 2023.

[33] S. G. Bailey and D. J. Flood, "Space photovoltaics," *Progress in Photovoltaics: Research and Applications*, vol. 6, no. 1, pp. 1–14, 1998.

[34] Y. Tu, J. Wu, G. Xu, X. Yang, R. Cai, Q. Gong, R. Zhu, and W. Huang, "Perovskite solar cells for space applications: Progress and challenges," *Advanced Materials*, vol. 33, no. 21, p. 2006545, 2021.

[35] I. Mathews, S. N. Kantareddy, T. Buonassisi, and I. M. Peters, "Technology and market perspective for indoor photovoltaic cells," *Joule*, vol. 3, no. 6, pp. 1415–1426, 2019.

[36] G. K. Grandhi, G. Koutsourakis, J. C. Blakesley, F. De Rossi, F. Brunetti, S. Öz, A. Sinicropi, M. L. Parisi, T. M. Brown, M. J. Carnie, R. L. Z. Hoye, and P. Vivo, "Promises and challenges of indoor photovoltaics," *Nature Reviews Clean Technology*, vol. 1, no. 2, pp. 132–147, 2025.

[37] H. S. Jung, G. S. Han, N.-G. Park, and M. J. Ko, "Flexible perovskite solar cells," *Joule*, vol. 3, no. 8, pp. 1850–1880, 2019.

[38] H. Lee and H.-J. Song, "Current status and perspective of colored photovoltaic modules," *WIREs Energy and Environment*, vol. 10, no. 6, p. e403, 2021.

[39] H. Wang, J. Li, H. A. Dewi, N. Mathews, S. Mhaisalkar, and A. Bruno, "Colorful perovskite solar cells: Progress, strategies, and potentials," *The Journal of Physical Chemistry Letters*, vol. 12, no. 4, pp. 1321–1329, 2021.

[40] M. Yamaguchi, F. Dimroth, J. F. Geisz, and N. J. Ekins-Daukes, "Multi-junction solar cells paving the way for super high-efficiency," *Journal of Applied Physics*, vol. 129, no. 24, p. 240901, 2021.

[41] V. Pecunia, L. G. Occhipinti, and R. L. Z. Hoye, "Emerging indoor photovoltaic technologies for sustainable internet of things," *Advanced Energy Materials*, vol. 11, no. 29, p. 2100698, 2021.

[42] M. F. Müller, "Indoor photovoltaics: Efficiencies, measurements and design," in *Solar Cell Nanotechnology*, ch. 8, pp. 203–222, John Wiley & Sons, Ltd, 2013.

[43] W. S. Wang, T. O'Donnell, L. Ribetto, B. O'Flynn, M. Hayes, and C. O'Mathuna, "Energy harvesting embedded wireless sensor system for building environment applications," in *2009 1st International Conference on Wireless Communication, Vehicular Technology, Information Theory and Aerospace & Electronic Systems Technology*, pp. 36–41, 2009.

[44] C. L. Cutting, M. Bag, and D. Venkataraman, "Indoor light recycling: a new home for organic photovoltaics," *J. Mater. Chem. C*, vol. 4, pp. 10367–10370, 2016.

[45] K. Rühle and M. Kasemann, "Approaching high efficiency wide range silicon solar cells," in *2013 IEEE 39th Photovoltaic Specialists Conference (PVSC)*, pp. 2651–2654, 2013.

[46] M. Freunek, M. Freunek, and L. M. Reindl, "Maximum efficiencies of indoor photovoltaic devices," *IEEE Journal of Photovoltaics*, vol. 3, no. 1, pp. 59–64, 2013.

[47] Y. Cui, L. Hong, and J. Hou, "Organic photovoltaic cells for indoor applications: Opportunities and challenges," *ACS Applied Materials & Interfaces*, vol. 12, no. 35, pp. 38815–38828, 2020.

[48] M. Freitag, J. Teuscher, Y. Saygili, X. Zhang, F. Giordano, P. Liska, J. Hua, S. M. Zakeeruddin, J.-E. Moser, M. Grätzel, and A. Hagfeldt, "Dye-sensitized solar cells for efficient power generation under ambient lighting," *Nature Photonics*, vol. 11, no. 6, pp. 372–378, 2017.

[49] Q. Ma, Y. Wang, L. Liu, P. Yang, W. He, X. Zhang, J. Zheng, M. Ma, M. Wan, Y. Yang, C. Zhang, T. Mahmoudi, S. Wu, C. Liu, Y.-B. Hahn, and Y. Mai, "One-step dual-additive passivated wide-bandgap perovskites to realize 44.72%-efficient indoor photovoltaics," *Energy Environ. Sci.*, vol. 17, pp. 1637–1644, 2024.

[50] R. Wang, H. Li, and H. Sun, "Bismuth: Environmental pollution and health effects," in *Encyclopedia of Environmental Health (Second Edition)* (J. Nriagu, ed.), pp. 415–423, Oxford: Elsevier, second edition ed., 2019.

[51] M. A. Green, "General temperature dependence of solar cell performance and implications for device modelling," *Progress in Photovoltaics: Research and Applications*, vol. 11, no. 5, pp. 333–340, 2003.

[52] K. Domanski, E. A. Alharbi, A. Hagfeldt, M. Grätzel, and W. Tress, "Systematic investigation of the impact of operation conditions on the degradation behaviour of perovskite solar cells," *Nature Energy*, vol. 3, no. 1, pp. 61–67, 2018.

[53] O. Dupré, R. Vaillon, and M. Green, "Physics of the temperature coefficients of solar cells," *Solar Energy Materials and Solar Cells*, vol. 140, pp. 92–100, 2015.

[54] I. Mesquita, L. Andrade, and A. Mendes, "Temperature impact on perovskite solar cells under operation," *ChemSusChem*, vol. 12, no. 10, pp. 2186–2194, 2019.

[55] A. Ndiaye, A. Charki, A. Kobi, C. M. Kébé, P. A. Ndiaye, and V. Sambou, "Degradations of silicon photovoltaic modules: A literature review," *Solar Energy*, vol. 96, pp. 140–151, 2013.

[56] G. Wachutka, "Rigorous thermodynamic treatment of heat generation and conduction in semiconductor device modeling," *IEEE Transactions on Computer-Aided Design of Integrated Circuits and Systems*, vol. 9, no. 11, pp. 1141–1149, 1990.

[57] U. Lindefelt, "Heat generation in semiconductor devices," *Journal of Applied Physics*, vol. 75, no. 2, pp. 942–957, 1994.

[58] A. Shang and X. Li, "Photovoltaic devices: Opto-electro-thermal physics and modeling," *Advanced Materials*, vol. 29, no. 8, p. 1603492, 2017.

[59] Y. An, C. Wang, G. Cao, and X. Li, "Heterojunction perovskite solar cells: Opto-electro-thermal physics, modeling, and experiment," *ACS Nano*, vol. 14, no. 4, pp. 5017–5026, 2020.

[60] M. Jošt, B. Lipovšek, B. Glažar, A. Al-Ashouri, K. Brecl, G. Matič, A. Magomedov, V. Getautis, M. Topič, and S. Albrecht, "Perovskite solar cells go outdoors: Field testing and temperature effects on energy yield," *Advanced Energy Materials*, vol. 10, no. 25, p. 2000454, 2020.

[61] P. Lopez-Varo, M. Amara, S. Cacovich, A. Julien, A. Yaïche, M. Jouhari, J. Rousset, P. Schulz, J.-F. Guillemoles, and J.-B. Puel, "Dynamic temperature effects in perovskite solar cells and energy yield," *Sustainable Energy & Fuels*, vol. 5, pp. 5523–5534, 2021.

[62] Y. An, T. Ma, and X. Li, "Energy tracing of photovoltaic cells," *Solar RRL*, vol. 5, no. 7, p. 2100199, 2021.

[63] R. Gehlhaar, T. Merckx, W. Qiu, and T. Aernouts, "Outdoor measurement and modeling of perovskite module temperatures," *Global Challenges*, vol. 2, no. 7, p. 1800008, 2018.

[64] E. Skoplaki and J. Palyvos, "On the temperature dependence of photovoltaic module electrical performance: A review of efficiency/power correlations," *Solar Energy*, vol. 83, no. 5, pp. 614–624, 2009.

[65] D. L. King, W. E. Boyson, and J. A. Kratochvil, "Photovoltaic array performance model," tech. rep., Sandia National Laboratories, 2004.

[66] D. Faiman, "Assessing the outdoor operating temperature of photovoltaic modules," *Progress in Photovoltaics: Research and Applications*, vol. 16, no. 4, pp. 307–315, 2008.

[67] Sandia National Laboratories, "PVsyst cell temperature model." `https://pvpmc.sandia.gov/modeling-guide/2-dc-module-iv/cell-temperature/pvsyst-cell-temperature-model/`. Accessed 2025-3-8.

[68] M. Mattei, G. Notton, C. Cristofari, M. Muselli, and P. Poggi, "Calculation of the polycrystalline PV module temperature using a simple method of energy balance," *Renewable Energy*, vol. 31, no. 4, pp. 553–567, 2006.

[69] E. Skoplaki, A. Boudouvis, and J. Palyvos, "A simple correlation for the operating temperature of photovoltaic modules of arbitrary mounting," *Solar Energy Materials and Solar Cells*, vol. 92, no. 11, pp. 1393–1402, 2008.

[70] E. Skoplaki and J. Palyvos, "Operating temperature of photovoltaic modules: A survey of pertinent correlations," *Renewable Energy*, vol. 34, no. 1, pp. 23–29, 2009.

[71] T. Townsend, "A method for estimating the long-term performance of direct-coupled photovoltaic systems," Master's thesis, University of Wisconsin-Madison, 1989.

[72] M. Koehl, M. Heck, S. Wiesmeier, and J. Wirth, "Modeling of the nominal operating cell temperature based on outdoor weathering," *Solar Energy Materials and Solar Cells*, vol. 95, no. 7, pp. 1638–1646, 2011.

[73] T. Webb, S. J. Sweeney, and W. Zhang, "Device architecture engineering: Progress toward next generation perovskite solar cells," *Advanced Functional Materials*, vol. 31, no. 35, p. 2103121, 2021.

[74] Y. Wu, X. Yang, W. Chen, Y. Yue, M. Cai, F. Xie, E. Bi, A. Islam, and L. Han, "Perovskite solar cells with 18.21% efficiency and area over 1 cm^2 fabricated by heterojunction engineering," *Nature Energy*, vol. 1, no. 11, p. 16148, 2016.

[75] J. Peng, D. Walter, Y. Ren, M. Tebyetekerwa, Y. Wu, T. Duong, Q. Lin, J. Li, T. Lu, M. A. Mahmud, O. L. C. Lem, S. Zhao, W. Liu, Y. Liu, H. Shen, L. Li, F. Kremer, H. T. Nguyen, D.-Y. Choi, K. J. Weber, K. R. Catchpole, and T. P. White, "Nanoscale localized contacts for high fill

factors in polymer-passivated perovskite solar cells," *Science*, vol. 371, no. 6527, pp. 390–395, 2021.

[76] G. He, A.-F. Castro-Méndez, J. Diekmann, G. J. W. Aalbers, P. Forozi Sowmeeh, A. Singh, S. V. Quiroz Monnens, F. Peña-Camargo, M. Stolterfoht, B. Stannowski, H. C. Neitzert, R. A. J. Janssen, C. M. Wolff, D. Neher, and F. Lang, "Point contacts in halide perovskite solar cells: from reduced interfacial recombination to increased ionic field screening," *EES Sol.*, vol. 1, pp. 775–785, 2025.

[77] M. Koç, W. Soltanpoor, G. Bektaş, H. J. Bolink, and S. Yerci, "Guideline for optical optimization of planar perovskite solar cells," *Advanced Optical Materials*, vol. 7, no. 23, p. 1900944, 2019.

[78] International Electrotechnical Commission (IEC), *Solar photovoltaic energy systems - Terms, definitions and symbols*, 2016. IEC TS 61836:2016, ed. 3.0.

[79] R. H. Mitchell, M. D. Welch, and A. R. Chakhmouradian, "Nomenclature of the perovskite supergroup: A hierarchical system of classification based on crystal structure and composition," *Mineralogical Magazine*, vol. 81, no. 3, p. 411–461, 2017.

[80] T. Baikie, Y. Fang, J. M. Kadro, M. Schreyer, F. Wei, S. G. Mhaisalkar, M. Graetzel, and T. J. White, "Synthesis and crystal chemistry of the hybrid perovskite (CH3NH3)PbI3 for solid-state sensitised solar cell applications," *J. Mater. Chem. A*, vol. 1, pp. 5628–5641, 2013.

[81] N. Onoda-Yamamuro, T. Matsuo, and H. Suga, "Calorimetric and IR spectroscopic studies of phase transitions in methylammonium trihalogenoplumbates (II)†," *Journal of Physics and Chemistry of Solids*, vol. 51, no. 12, pp. 1383–1395, 1990.

[82] A. Poglitsch and D. Weber, "Dynamic disorder in methylammoniumtrihalogenoplumbates (II) observed by millimeter-wave spectroscopy," *The Journal of Chemical Physics*, vol. 87, no. 11, pp. 6373–6378, 1987.

[83] "Materials data on CaTiO3 by Materials Project." `https://doi.org/10.17188/1272675`. Accessed 2026-4-23.

[84] Materials Design Group, "CH3NH3PbI3_cubic.cif." `https://github.com/WMD-group/hybrid-perovskites/blob/master/2015_ch3nh3pbi3_phonons_PBEsol/CH3NH3PbI3_cubic.cif`. Accessed 2025-10-21.

[85] K. Momma and F. Izumi, "*VESTA3* for three-dimensional visualization of crystal, volumetric and morphology data," *Journal of Applied Crystallography*, vol. 44, no. 6, pp. 1272–1276, 2011.

[86] M. H. Miah, M. U. Khandaker, M. B. Rahman, M. Nur-E-Alam, and M. A. Islam, "Band gap tuning of perovskite solar cells for enhancing the efficiency and stability: issues and prospects," *RSC Adv.*, vol. 14, pp. 15876–15906, 2024.

[87] M. A. Green, A. Ho-Baillie, and H. J. Snaith, "The emergence of perovskite solar cells," *Nature Photonics*, vol. 8, no. 7, pp. 506–514, 2014.

[88] A. Fakharuddin, M. K. Gangishetty, M. Abdi-Jalebi, S.-H. Chin, A. R. bin Mohd Yusoff, D. N. Congreve, W. Tress, F. Deschler, M. Vasilopoulou, and H. J. Bolink, "Perovskite light-emitting diodes," *Nature Electronics*, vol. 5, no. 4, pp. 203–216, 2022.

[89] X. Xiao, J. Hu, S. Tang, K. Yan, B. Gao, H. Chen, and D. Zou, "Recent advances in halide perovskite memristors: Materials, structures, mechanisms, and applications," *Advanced Materials Technologies*, vol. 5, no. 6, p. 1900914, 2020.

[90] R. Chen, J. Wang, Z. Liu, F. Ren, S. Liu, J. Zhou, H. Wang, X. Meng, Z. Zhang, X. Guan, W. Liang, P. A. Troshin, Y. Qi, L. Han, and W. Chen, "Reduction of bulk and surface defects in inverted methylammonium- and bromide-free formamidinium perovskite solar cells," *Nature Energy*, vol. 8, no. 8, pp. 839–849, 2023.

[91] A. Miyata, A. Mitioglu, P. Plochocka, O. Portugall, J. T.-W. Wang, S. D. Stranks, H. J. Snaith, and R. J. Nicholas, "Direct measurement of the exciton binding energy and effective masses for charge carriers in organic–inorganic tri-halide perovskites," *Nature Physics*, vol. 11, no. 7, pp. 582–587, 2015.

[92] A. M. Glazer, "The classification of tilted octahedra in perovskites," *Acta Crystallographica Section B*, vol. 28, no. 11, pp. 3384–3392, 1972.

[93] Y. Chang, C. H. Park, and K. Matsuishi, "First-principles study of the structural and the electronic properties of the lead-halide-based inorganic-organic perovskites (CH3NH3)PbX3 and CsPbX3 (X= Cl, Br, I)," *Journal of the Korean Physical Society*, vol. 44, pp. 889–893, 2004.

[94] F. Brivio, A. B. Walker, and A. Walsh, "Structural and electronic properties of hybrid perovskites for high-efficiency thin-film photovoltaics from first-principles," *APL Materials*, vol. 1, no. 4, p. 042111, 2013.

[95] J. M. Frost, K. T. Butler, F. Brivio, C. H. Hendon, M. van Schilfgaarde, and A. Walsh, "Atomistic origins of high-performance in hybrid halide perovskite solar cells," *Nano Letters*, vol. 14, no. 5, pp. 2584–2590, 2014.

[96] R. X. Yang, J. M. Skelton, E. L. da Silva, J. M. Frost, and A. Walsh, "Spontaneous octahedral tilting in the cubic inorganic cesium halide perovskites CsSnX3 and CsPbX3 (X = F, Cl, Br, I)," *The Journal of Physical Chemistry Letters*, vol. 8, no. 19, pp. 4720–4726, 2017.

[97] N. J. Weadock, T. C. Sterling, J. A. Vigil, A. Gold-Parker, I. C. Smith, B. Ahammed, M. J. Krogstad, F. Ye, D. Voneshen, P. M. Gehring, A. M. Rappe, H.-G. Steinrück, E. Ertekin, H. I. Karunadasa, D. Reznik, and M. F. Toney, "The nature of dynamic local order in CH3NH3PbI3 and CH3NH3PbBr3," *Joule*, vol. 7, no. 5, pp. 1051–1066, 2023.

[98] M. Dubajic, J. R. Neilson, J. Klarbring, X. Liang, S. A. Bird, K. C. Rule, J. E. Auckett, T. A. Selby, G. Tumen-Ulzii, Y. Lu, Y.-K. Jung, C. Chosy, Z. Wei, Y. Boeije, M. v. Zimmermann, A. Pusch, L. Gu, X. Jia, Q. Wu, J. C. Trowbridge, E. M. Mozur, A. Minelli, N. Roth, K. W. P. Orr, A. Mahboubi Soufiani, S. Kahmann, I. Kabakova, J. Ding, T. Wu, G. J. Conibeer, S. P. Bremner, M. P. Nielsen, A. Walsh, and S. D. Stranks, "Dynamic nanodomains dictate macroscopic properties in lead halide perovskites," *Nature Nanotechnology*, vol. 20, no. 6, pp. 755–763, 2025.

[99] J. M. Frost and A. Walsh, "What is moving in hybrid halide perovskite solar cells?," *Accounts of Chemical Research*, vol. 49, no. 3, pp. 528–535, 2016.

[100] J. Mizusaki, K. Arai, and K. Fueki, "Ionic conduction of the perovskite-type halides," *Solid State Ionics*, vol. 11, no. 3, pp. 203–211, 1983.

[101] C. Eames, J. M. Frost, P. R. F. Barnes, B. C. O'Regan, A. Walsh, and M. S. Islam, "Ionic transport in hybrid lead iodide perovskite solar cells," *Nature Communications*, vol. 6, no. 1, p. 7497, 2015.

[102] W. Tress, "Metal halide perovskites as mixed electronic–ionic conductors: Challenges and opportunities—from hysteresis to memristivity," *The Journal of Physical Chemistry Letters*, vol. 8, no. 13, pp. 3106–3114, 2017.

[103] W. Tress, N. Marinova, T. Moehl, S. M. Zakeeruddin, M. K. Nazeeruddin, and M. Grätzel, "Understanding the rate-dependent J–V hysteresis, slow time component, and aging in CH3NH3PbI3 perovskite solar cells: the role of a compensated electric field," *Energy Environ. Sci.*, vol. 8, pp. 995–1004, 2015.

[104] P. Calado, A. M. Telford, D. Bryant, X. Li, J. Nelson, B. C. O'Regan, and P. R. Barnes, "Evidence for ion migration in hybrid perovskite solar cells with minimal hysteresis," *Nature Communications*, vol. 7, no. 1, p. 13831, 2016.

[105] J. Thiesbrummel, S. Shah, E. Gutierrez-Partida, F. Zu, F. Peña-Camargo, S. Zeiske, J. Diekmann, F. Ye, K. P. Peters, K. O. Brinkmann, P. Caprioglio, A. Dasgupta, S. Seo, F. A. Adeleye, J. Warby, Q. Jeangros, F. Lang, S. Zhang, S. Albrecht, T. Riedl, A. Armin, D. Neher, N. Koch, Y. Wu, V. M. Le Corre, H. Snaith, and M. Stolterfoht, "Ion-induced field screening as a dominant factor in perovskite solar cell operational stability," *Nature Energy*, vol. 9, no. 6, pp. 664–676, 2024.

[106] W.-J. Yin, T. Shi, and Y. Yan, "Unusual defect physics in CH3NH3PbI3 perovskite solar cell absorber," *Applied Physics Letters*, vol. 104, no. 6, p. 063903, 2014.

[107] K. X. Steirer, P. Schulz, G. Teeter, V. Stevanovic, M. Yang, K. Zhu, and J. J. Berry, "Defect tolerance in methylammonium lead triiodide perovskite," *ACS Energy Letters*, vol. 1, no. 2, pp. 360–366, 2016.

[108] J. Schmidt, B. Lim, D. Walter, K. Bothe, S. Gatz, T. Dullweber, and P. P. Altermatt, "Impurity-related limitations of next-generation industrial silicon solar cells," *IEEE Journal of Photovoltaics*, vol. 3, no. 1, pp. 114–118, 2013.

[109] J. Hofstetter, C. del Cañizo, H. Wagner, S. Castellanos, and T. Buonassisi, "Material requirements for the adoption of unconventional silicon crystal and wafer growth techniques for high-efficiency solar cells," *Progress in Photovoltaics: Research and Applications*, vol. 24, no. 1, pp. 122–132, 2016.

[110] Z. Ni, C. Bao, Y. Liu, Q. Jiang, W.-Q. Wu, S. Chen, X. Dai, B. Chen, B. Hartweg, Z. Yu, Z. Holman, and J. Huang, "Resolving spatial and energetic distributions of trap states in metal halide perovskite solar cells," *Science*, vol. 367, no. 6484, pp. 1352–1358, 2020.

[111] S. Singh, C. Li, F. Panzer, K. L. Narasimhan, A. Graeser, T. P. Gujar, A. Köhler, M. Thelakkat, S. Huettner, and D. Kabra, "Effect of thermal and structural disorder on the electronic structure of hybrid perovskite semiconductor CH3NH3PbI3," *The Journal of Physical Chemistry Letters*, vol. 7, no. 15, pp. 3014–3021, 2016.

[112] Y.-T. Huang, S. R. Kavanagh, D. O. Scanlon, A. Walsh, and R. L. Z. Hoye, "Perovskite-inspired materials for photovoltaics and beyond—from design to devices," *Nanotechnology*, vol. 32, no. 13, p. 132004, 2021.

[113] Z. Xiao, W. Meng, J. Wang, D. B. Mitzi, and Y. Yan, "Searching for promising new perovskite-based photovoltaic absorbers: the importance of electronic dimensionality," *Mater. Horiz.*, vol. 4, pp. 206–216, 2017.

[114] M. Born and E. Wolf, *Principles of Optics*. Oxford: Pergamon Press, 4. ed., 1970.

[115] T. G. Mayerhöfer, S. Pahlow, and J. Popp, "The Bouguer-Beer-Lambert law: Shining light on the obscure," *ChemPhysChem*, vol. 21, no. 18, pp. 2029–2046, 2020.

[116] L. A. A. Pettersson, L. S. Roman, and O. Inganäs, "Modeling photocurrent action spectra of photovoltaic devices based on organic thin films," *Journal of Applied Physics*, vol. 86, no. 1, pp. 487–496, 1999.

[117] C. C. Katsidis and D. I. Siapkas, "General transfer-matrix method for optical multilayer systems with coherent, partially coherent, and incoherent interference," *Appl. Opt.*, vol. 41, no. 19, pp. 3978–3987, 2002.

[118] G. F. Burkhard, E. T. Hoke, and M. D. McGehee, "Accounting for interference, scattering, and electrode absorption to make accurate internal quantum efficiency measurements in organic and other thin solar cells," *Advanced Materials*, vol. 22, no. 30, pp. 3293–3297, 2010.

[119] R. Santbergen, A. H. Smets, and M. Zeman, "Optical model for multilayer structures with coherent, partly coherent and incoherent layers," *Opt. Express*, vol. 21, no. S2, pp. A262–A267, 2013.

[120] A. Lipson, S. G. Lipson, and H. Lipson, *Optical Physics*. Cambridge University Press, 4. ed., 2010.

[121] M. C. Troparevsky, A. S. Sabau, A. R. Lupini, and Z. Zhang, "Transfer-matrix formalism for the calculation of optical response in multilayer systems: from coherent to incoherent interference," *Opt. Express*, vol. 18, no. 24, pp. 24715–24721, 2010.

[122] R. Pérez-Álvarez, R. Pernas-Salomón, and V. R. Velasco, "Relations between transfer matrices and numerical stability analysis to avoid the Ωd problem," *SIAM Journal on Applied Mathematics*, vol. 75, no. 4, pp. 1403–1423, 2015.

[123] W. Raja, T. G. Allen, A. A. Said, O. Alharbi, E. Aydin, M. De Bastiani, and S. De Wolf, "Temperature-dependent optical modeling of perovskite solar cells," *The Journal of Physical Chemistry C*, vol. 126, no. 33, pp. 14366–14374, 2022.

[124] Y. Jiang, A. M. Soufiani, A. Gentle, F. Huang, A. Ho-Baillie, and M. A. Green, "Temperature dependent optical properties of CH3NH3PbI3 perovskite by spectroscopic ellipsometry," *Applied Physics Letters*, vol. 108, no. 6, p. 061905, 2016.

[125] S. Manzoor, J. Häusele, K. A. Bush, A. F. Palmstrom, J. Carpenter, Z. J. Yu, S. F. Bent, M. D. Mcgehee, and Z. C. Holman, "Optical modeling of wide-bandgap perovskite and perovskite/silicon tandem solar cells using complex refractive indices for arbitrary-bandgap perovskite absorbers," *Opt. Express*, vol. 26, no. 21, pp. 27441–27460, 2018.

[126] J. Werner, G. Nogay, F. Sahli, T. C.-J. Yang, M. Bräuninger, G. Christmann, A. Walter, B. A. Kamino, P. Fiala, P. Löper, S. Nicolay, Q. Jeangros, B. Niesen, and C. Ballif, "Complex refractive

indices of cesium–formamidinium-based mixed-halide perovskites with optical band gaps from 1.5 to 1.8 eV," *ACS Energy Letters*, vol. 3, no. 3, pp. 742–747, 2018.

[127] M. Anaya, J. P. Correa-Baena, G. Lozano, M. Saliba, P. Anguita, B. Roose, A. Abate, U. Steiner, M. Grätzel, M. E. Calvo, A. Hagfeldt, and H. Míguez, "Optical analysis of CH3NH3SnxPb(1-x)I3 absorbers: a roadmap for perovskite-on-perovskite tandem solar cells," *J. Mater. Chem. A*, vol. 4, pp. 11214–11221, 2016.

[128] R. Santbergen, J. Goud, M. Zeman, J. van Roosmalen, and R. van Zolingen, "The AM1.5 absorption factor of thin-film solar cells," *Solar Energy Materials and Solar Cells*, vol. 94, no. 5, pp. 715–723, 2010.

[129] T. Trupke, E. Daub, and P. Würfel, "Absorptivity of silicon solar cells obtained from luminescence," *Solar Energy Materials and Solar Cells*, vol. 53, no. 1, pp. 103–114, 1998.

[130] T. Trupke, M. A. Green, and P. Würfel, "Improving solar cell efficiencies by down-conversion of high-energy photons," *Journal of Applied Physics*, vol. 92, no. 3, pp. 1668–1674, 2002.

[131] S. M. Sze, *Physics of Semiconductor Devices*. New York: Wiley, 2. ed., 1981.

[132] COMSOL, *Semiconductor Module User's Guide (6.2)*, 2024.

[133] J. M. Richter, F. Branchi, F. Valduga de Almeida Camargo, B. Zhao, R. H. Friend, G. Cerullo, and F. Deschler, "Ultrafast carrier thermalization in lead iodide perovskite probed with two-dimensional electronic spectroscopy," *Nature Communications*, vol. 8, no. 1, p. 376, 2017.

[134] M. B. Price, J. Butkus, T. C. Jellicoe, A. Sadhanala, A. Briane, J. E. Halpert, K. Broch, J. M. Hodgkiss, R. H. Friend, and F. Deschler, "Hot-carrier cooling and photoinduced refractive index changes in organic–inorganic lead halide perovskites," *Nature Communications*, vol. 6, no. 1, p. 8420, 2015.

[135] Y. Yang, D. P. Ostrowski, R. M. France, K. Zhu, J. van de Lagemaat, J. M. Luther, and M. C. Beard, "Observation of a hot-phonon bottleneck in lead-iodide perovskites," *Nature Photonics*, vol. 10, no. 1, pp. 53–59, 2016.

[136] S. J. Blundell and K. M. Blundell, *Concepts in Thermal Physics*. Oxford University Press, 2 ed., 2010.

[137] M. R. Vogt, *Development of physical models for the simulation of optical properties of solar cell modules*. PhD thesis, Leibniz Universität Hannover, 2016.

[138] E. Raoult, "Dataset." `https://opticapublishing.figshare.com/articles/dataset/Dataset_xlsx/16738531`, 2022.

[139] E. Raoult, R. Bodeux, S. Jutteau, S. Rives, A. Yaiche, A. Blaizot, D. Coutancier, J. Rousset, and S. Collin, "Iterative method for optical modelling of perovskite-based tandem solar cells," *Opt. Express*, vol. 30, no. 6, pp. 9604–9622, 2022.

[140] R. L. Olmon, B. Slovick, T. W. Johnson, D. Shelton, S.-H. Oh, G. D. Boreman, and M. B. Raschke, "Optical dielectric function of gold," *Phys. Rev. B*, vol. 86, p. 235147, 2012.

[141] M. N. Polyanskiy, "Refractiveindex.info database of optical constants," *Scientific Data*, vol. 11, no. 1, p. 94, 2024.

[142] H. H. Li, "Refractive index of alkaline earth halides and its wavelength and temperature derivatives," *Journal of Physical and Chemical Reference Data*, vol. 9, no. 1, pp. 161–290, 1980.

[143] J. P. Correa Baena, L. Steier, W. Tress, M. Saliba, S. Neutzner, T. Matsui, F. Giordano, T. J. Jacobsson, A. R. Srimath Kandada, S. M. Zakeeruddin, A. Petrozza, A. Abate, M. K. Nazeeruddin, M. Grätzel, and A. Hagfeldt, "Highly efficient planar perovskite solar cells through band alignment engineering," *Energy Environ. Sci.*, vol. 8, pp. 2928–2934, 2015.

[144] J. A. Spencer, A. L. Mock, A. G. Jacobs, M. Schubert, Y. Zhang, and M. J. Tadjer, "A review of band structure and material properties of transparent conducting and semiconducting oxides: Ga2O3, Al2O3, In2O3, ZnO, SnO2, CdO, NiO, CuO, and Sc2O3," *Applied Physics Reviews*, vol. 9, no. 1, 2022.

[145] T. Minemoto and M. Murata, "Device modeling of perovskite solar cells based on structural similarity with thin film inorganic semiconductor solar cells," *Journal of Applied Physics*, vol. 116, no. 5, 2014.

[146] Z. Hawash, L. K. Ono, and Y. Qi, "Recent advances in spiro-meotad hole transport material and its applications in organic–inorganic halide perovskite solar cells," *Advanced Materials Interfaces*, vol. 5, no. 1, p. 1700623, 2018.
[147] H. Van Daal, "The static dielectric constant of SnO2," *Journal of Applied Physics*, vol. 39, no. 9, pp. 4467–4469, 1968.
[148] D. Poplavskyy and J. Nelson, "Nondispersive hole transport in amorphous films of methoxy-spirofluorene-arylamine organic compound," *Journal of Applied Physics*, vol. 93, no. 1, pp. 341–346, 2002.
[149] P. Zhao, Z. Lin, J. Wang, M. Yue, J. Su, J. Zhang, J. Chang, and Y. Hao, "Numerical simulation of planar heterojunction perovskite solar cells based on SnO2 electron transport layer," *ACS Applied Energy Materials*, vol. 2, no. 6, pp. 4504–4512, 2019.
[150] G. Sanon, R. Rup, and A. Mansingh, "Band-gap narrowing and band structure in degenerate tin oxide (SnO2) films," *Phys. Rev. B*, vol. 44, pp. 5672–5680, 1991.
[151] Q. Zhou, D. Jiao, K. Fu, X. Wu, Y. Chen, J. Lu, and S. e Yang, "Two-dimensional device modeling of CH3NH3PbI3 based planar heterojunction perovskite solar cells," *Solar Energy*, vol. 123, pp. 51–56, 2016.
[152] K. Wijeratne, J. Akilavasan, M. Thelakkat, and J. Bandara, "Enhancing the solar cell efficiency through pristine 1-dimentional SnO2 nanostructures: Comparison of charge transport and carrier lifetime of SnO2 particles vs. nanorods," *Electrochimica Acta*, vol. 72, pp. 192–198, 2012.
[153] M. Feneberg, C. Lidig, K. Lange, M. E. White, M. Y. Tsai, J. S. Speck, O. Bierwagen, and R. Goldhahn, "Anisotropy of the electron effective mass in rutile SnO2 determined by infrared ellipsometry," *physica status solidi (a)*, vol. 211, no. 1, pp. 82–86, 2014.
[154] R. L. Milot, G. E. Eperon, H. J. Snaith, M. B. Johnston, and L. M. Herz, "Temperature-dependent charge-carrier dynamics in CH3NH3PbI3 perovskite thin films," *Advanced Functional Materials*, vol. 25, no. 39, pp. 6218–6227, 2015.
[155] L. M. Herz, "Charge-carrier mobilities in metal halide perovskites: Fundamental mechanisms and limits," *ACS Energy Letters*, vol. 2, no. 7, pp. 1539–1548, 2017.
[156] H. J. Snaith and M. Grätzel, "Enhanced charge mobility in a molecular hole transporter via addition of redox inactive ionic dopant: Implication to dye-sensitized solar cells," *Applied Physics Letters*, vol. 89, no. 26, p. 262114, 2006.
[157] I. Subedi, T. J. Silverman, M. G. Deceglie, and N. J. Podraza, "PERC silicon PV infrared to ultraviolet optical model," *Solar Energy Materials and Solar Cells*, vol. 215, p. 110655, 2020.
[158] C. Berthod, R. Strandberg, G. H. Yordanov, H. G. Beyer, and J. O. Odden, "On the variability of the temperature coefficients of mc-Si solar cells with irradiance," *Energy Procedia*, vol. 92, pp. 2–9, 2016.
[159] F. Muhammadsharif and S. Hashim, "A simple and efficient determination of the ideality factor of solar cells and modules from the knee point of the shunt resistance curve," *Arab J Sci Eng*, vol. 48, pp. 8217–8225, 2023.
[160] J. Haschke, J. P. Seif, Y. Riesen, A. Tomasi, J. Cattin, L. Tous, P. Choulat, M. Aleman, E. Cornagliotti, A. Uruena, R. Russell, F. Duerinckx, J. Champliaud, J. Levrat, A. A. Abdallah, B. Aïssa, N. Tabet, N. Wyrsch, M. Despeisse, J. Szlufcik, S. De Wolf, and C. Ballif, "The impact of silicon solar cell architecture and cell interconnection on energy yield in hot & sunny climates," *Energy Environ. Sci.*, vol. 10, pp. 1196–1206, 2017.
[161] M. A. Green, "Intrinsic concentration, effective densities of states, and effective mass in silicon," *Journal of Applied Physics*, vol. 67, no. 6, pp. 2944–2954, 1990.
[162] J. M. Ball, S. D. Stranks, M. T. Hörantner, S. Hüttner, W. Zhang, E. J. W. Crossland, I. Ramirez, M. Riede, M. B. Johnston, R. H. Friend, and H. J. Snaith, "Optical properties and limiting photocurrent of thin-film perovskite solar cells," *Energy Environ. Sci.*, vol. 8, pp. 602–609, 2015.
[163] W. Zhang, L. He, Y. Meng, H. Kanda, D. Tang, B. Ding, Y. Ding, M. K. Nazeeruddin, and X. Li, "Dual-site synergistic passivation for highly efficient and stable perovskite solar cells," *Advanced Energy Materials*, vol. 12, no. 46, p. 2202189, 2022.

[164] L. Migliorini, L. Molinaroli, R. Simonetti, and G. Manzolini, "Development and experimental validation of a comprehensive thermoelectric dynamic model of photovoltaic modules," *Solar Energy*, vol. 144, pp. 489–501, 2017.

[165] L. Wang, J. Wen, C. Yang, and B. Xiong, "Potential of ITO thin film for electrical probe memory applications," *Science and Technology of Advanced Materials*, vol. 19, no. 1, pp. 791–801, 2018.

[166] P. Saxena and N. E. Gorji, "COMSOL simulation of heat distribution in perovskite solar cells: Coupled optical–electrical–thermal 3-D analysis," *IEEE Journal of Photovoltaics*, vol. 9, no. 6, pp. 1693–1698, 2019.

[167] J. Zhou, Q. Yi, Y. Wang, and Z. Ye, "Temperature distribution of photovoltaic module based on finite element simulation," *Solar Energy*, vol. 111, pp. 97–103, 2015.

[168] T. Ashida, A. Miyamura, N. Oka, Y. Sato, T. Yagi, N. Taketoshi, T. Baba, and Y. Shigesato, "Thermal transport properties of polycrystalline tin-doped indium oxide films," *Journal of Applied Physics*, vol. 105, no. 7, 2009.

[169] A. Pisoni, J. Jaćimović, O. S. Barišić, M. Spina, R. Gaál, L. Forró, and E. Horváth, "Ultra-low thermal conductivity in organic–inorganic hybrid perovskite CH3NH3PbI3," *The Journal of Physical Chemistry Letters*, vol. 5, no. 14, pp. 2488–2492, 2014.

[170] T. Haeger, R. Heiderhoff, and T. Riedl, "Thermal properties of metal-halide perovskites," *J. Mater. Chem. C*, vol. 8, pp. 14289–14311, 2020.

[171] M. I. Alonso and M. Garriga, "Optical properties of semiconductors," in *Spectroscopic Ellipsometry for Photovoltaics: Volume 1: Fundamental Principles and Solar Cell Characterization* (H. Fujiwara and R. W. Collins, eds.), pp. 89–113, Cham: Springer International Publishing, 2018.

[172] J. A. Karhu and A. V. Lindfors, "PV production data with ancillary PV and meteorological data including solar radiation measurements from FMI's outdoor solar laboratories in Helsinki, Kuopio and Sodankylä (Finland) starting from August 2015 and ending Dec 2021 [Data set]." https://doi.org/10.57707/FMI-B2SHARE.FBE73C1D7C144CE787DB3785302DD1E1, 2025.

[173] J. A. Karhu, A. V. Lindfors, W. Wandji Nyamsi, T. Salola, A. Poikonen, M. R. A. Pitkänen, T. Mielonen, and O. Mantikka, "Photovoltaic power and meteorological datasets with snow detection from the outdoor solar power laboratories of the Finnish Meteorological Institute," *Geoscience Data Journal*, vol. 13, no. 1, p. e70039, 2026.

[174] H. Fujiwara and R. W. Collins, eds., *Spectroscopic ellipsometry for photovoltaics*, vol. 1. Springer, 2018.

[175] D. Lehmann, F. Seidel, and D. R. Zahn, "Thin films with high surface roughness: thickness and dielectric function analysis using spectroscopic ellipsometry," *SpringerPlus*, vol. 3, no. 1, p. 82, 2014.

[176] H. Fujiwara, "Introduction," in *Spectroscopic Ellipsometry for Photovoltaics: Volume 1: Fundamental Principles and Solar Cell Characterization* (H. Fujiwara and R. W. Collins, eds.), pp. 1–16, Cham: Springer International Publishing, 2018.

[177] P. Eaton and P. West, "Chapter 1 introduction," in *Atomic Force Microscopy*, Oxford University Press, 2010.

[178] D. Nečas and P. Klapetek, "Gwyddion: an open-source software for SPM data analysis," *Central European Journal of Physics*, vol. 10, pp. 181–188, 2012.

[179] "Gwyddion." https://gwyddion.net/. Accessed 2025-12-15.

[180] H. Fujiwara, "Effect of roughness on ellipsometry analysis," in *Spectroscopic Ellipsometry for Photovoltaics: Volume 1: Fundamental Principles and Solar Cell Characterization* (H. Fujiwara and R. W. Collins, eds.), pp. 155–172, Cham: Springer International Publishing, 2018.

[181] S. N. Savenkov, "Jones and mueller matrices: structure, symmetry relations and information content," in *Light Scattering Reviews 4: Single Light Scattering and Radiative Transfer* (A. A. Kokhanovsky, ed.), pp. 71–119, Berlin, Heidelberg: Springer Berlin Heidelberg, 2009.

[182] G. K. Grandhi, S. Toikkonen, B. Al-Anesi, V. Pecunia, and P. Vivo, "Perovskite-inspired Cu2AgBiI6 for mesoscopic indoor photovoltaics under realistic low-light intensity conditions," *Sustainable Energy & Fuels*, vol. 7, pp. 66–73, 2023.

[183] G. Burwell, S. Zeiske, P. Caprioglio, O. J. Sandberg, A. M. Kay, M. D. Farrar, Y. R. Kim, H. J. Snaith, P. Meredith, and A. Armin, "Wide-gap perovskites for indoor photovoltaics," *Solar RRL*, vol. 8, no. 11, p. 2400180, 2024.

[184] H. Fujiwara, S. Fujimoto, M. Tamakoshi, M. Kato, H. Kadowaki, T. Miyadera, H. Tampo, M. Chikamatsu, and H. Shibata, "Determination and interpretation of the optical constants for solar cell materials," *Applied Surface Science*, vol. 421, pp. 276–282, 2017.

[185] P. Löper, M. Stuckelberger, B. Niesen, J. Werner, M. Filipič, S.-J. Moon, J.-H. Yum, M. Topič, S. De Wolf, and C. Ballif, "Complex refractive index spectra of CH3NH3PbI3 perovskite thin films determined by spectroscopic ellipsometry and spectrophotometry," *The Journal of Physical Chemistry Letters*, vol. 6, no. 1, pp. 66–71, 2015.

[186] M. Shirayama, H. Kadowaki, T. Miyadera, T. Sugita, M. Tamakoshi, M. Kato, T. Fujiseki, D. Murata, S. Hara, T. N. Murakami, S. Fujimoto, M. Chikamatsu, and H. Fujiwara, "Optical transitions in hybrid perovskite solar cells: Ellipsometry, density functional theory, and quantum efficiency analyses for CH3NH3PbI3," *Phys. Rev. Appl.*, vol. 5, p. 014012, 2016.

[187] B.-W. Park, B. Philippe, X. Zhang, H. Rensmo, G. Boschloo, and E. M. J. Johansson, "Bismuth based hybrid perovskites A3Bi2I9 (A: methylammonium or cesium) for solar cell application," *Advanced Materials*, vol. 27, no. 43, pp. 6806–6813, 2015.

[188] C. Wu, Q. Zhang, Y. Liu, W. Luo, X. Guo, Z. Huang, H. Ting, W. Sun, X. Zhong, S. Wei, S. Wang, Z. Chen, and L. Xiao, "The dawn of lead-free perovskite solar cell: Highly stable double perovskite Cs2AgBiBr6 film," *Advanced Science*, vol. 5, no. 3, p. 1700759, 2018.

[189] G. Longo, S. Mahesh, L. R. V. Buizza, A. D. Wright, A. J. Ramadan, M. Abdi-Jalebi, P. K. Nayak, L. M. Herz, and H. J. Snaith, "Understanding the performance-limiting factors of Cs2AgBiBr6 double-perovskite solar cells," *ACS Energy Letters*, vol. 5, no. 7, pp. 2200–2207, 2020.

[190] G. K. Grandhi, B. Al-Anesi, H. Pasanen, H. Ali-Löytty, K. Lahtonen, S. Granroth, N. Christian, A. Matuhina, M. Liu, A. Berdin, V. Pecunia, and P. Vivo, "Enhancing the microstructure of perovskite-inspired Cu-Ag-Bi-I absorber for efficient indoor photovoltaics," *Small*, vol. 18, no. 35, p. 2203768, 2022.

[191] H. C. Sansom, G. Longo, A. D. Wright, L. R. V. Buizza, S. Mahesh, B. Wenger, M. Zanella, M. Abdi-Jalebi, M. J. Pitcher, M. S. Dyer, T. D. Manning, R. H. Friend, L. M. Herz, H. J. Snaith, J. B. Claridge, and M. J. Rosseinsky, "Highly absorbing lead-free semiconductor Cu2AgBiI6 for photovoltaic applications from the quaternary CuI–AgI–BiI3 phase space," *Journal of the American Chemical Society*, vol. 143, no. 10, pp. 3983–3992, 2021.

[192] L. R. V. Buizza, A. D. Wright, G. Longo, H. C. Sansom, C. Q. Xia, M. J. Rosseinsky, M. B. Johnston, H. J. Snaith, and L. M. Herz, "Charge-carrier mobility and localization in semiconducting Cu2AgBiI6 for photovoltaic applications," *ACS Energy Letters*, vol. 6, no. 5, pp. 1729–1739, 2021.

[193] V. Sugathan, M. Liu, A. Pecoraro, T. K. Das, T.-P. Ruoko, G. K. Grandhi, D. Manna, H. Ali-Löytty, K. Lahtonen, A. B. Muñoz-García, M. Pavone, and P. Vivo, "Halide engineering in mixed halide perovskite-inspired Cu2AgBiI6 for solar cells with enhanced performance," *ACS Applied Materials & Interfaces*, vol. 16, no. 15, pp. 19026–19038, 2024.

[194] S. Valastro, S. Gavranovic, I. Deretzis, M. Vala, E. Smecca, A. La Magna, A. Alberti, K. Castkova, and G. Mannino, "Temperature-dependent excitonic band gap in lead-free bismuth halide low-dimensional perovskite single crystals," *Advanced Optical Materials*, vol. 12, no. 11, p. 2302397, 2024.

[195] B. Al-Anesi, G. K. Grandhi, A. Pecoraro, V. Sugathan, N. S. M. Viswanath, H. Ali-Löytty, M. Liu, T.-P. Ruoko, K. Lahtonen, D. Manna, S. Toikkonen, A. B. Muñoz-García, M. Pavone, and P. Vivo, "Antimony-bismuth alloying: The key to a major boost in the efficiency of lead-free perovskite-inspired photovoltaics," *Small*, vol. 19, no. 46, p. 2303575, 2023.

[196] J. P. Perdew, W. Yang, K. Burke, Z. Yang, E. K. U. Gross, M. Scheffler, G. E. Scuseria, T. M. Henderson, I. Y. Zhang, A. Ruzsinszky, H. Peng, J. Sun, E. Trushin, and A. Görling, "Understanding band gaps of solids in generalized Kohn–Sham theory," *Proceedings of the National Academy of Sciences*, vol. 114, no. 11, pp. 2801–2806, 2017.

[197] Q. H. Chen, Y. Zhang, P. Huang, Q. Chen, Z. Yang, and Y. Jiang, "Optical, electrical, thermal, stress, and energy yield simulations enhance the performance and stability of perovskite photovoltaics," *Advanced Materials*, vol. 38, no. 1, p. e14184, 2026.

[198] L. C. Hirst and N. J. Ekins-Daukes, "Fundamental losses in solar cells," *Progress in Photovoltaics: Research and Applications*, vol. 19, no. 3, pp. 286–293, 2011.

[199] L. M. Pazos-Outón, M. Szumilo, R. Lamboll, J. M. Richter, M. Crespo-Quesada, M. Abdi-Jalebi, H. J. Beeson, M. Vrućinić, M. Alsari, H. J. Snaith, B. Ehrler, R. H. Friend, and F. Deschler, "Photon recycling in lead iodide perovskite solar cells," *Science*, vol. 351, no. 6280, pp. 1430–1433, 2016.

[200] T. Kirchartz, F. Staub, and U. Rau, "Impact of photon recycling on the open-circuit voltage of metal halide perovskite solar cells," *ACS Energy Letters*, vol. 1, no. 4, pp. 731–739, 2016.

[201] F. Staub, T. Kirchartz, K. Bittkau, and U. Rau, "Manipulating the net radiative recombination rate in lead halide perovskite films by modification of light outcoupling," *The Journal of Physical Chemistry Letters*, vol. 8, no. 20, pp. 5084–5090, 2017.

[202] S. Zeder, B. Ruhstaller, and U. Aeberhard, "Assessment of photon recycling in perovskite solar cells by fully coupled optoelectronic simulation," *Phys. Rev. Appl.*, vol. 17, p. 014023, 2022.

[203] F. Fu, T. Feurer, T. P. Weiss, S. Pisoni, E. Avancini, C. Andres, S. Buecheler, and A. N. Tiwari, "High-efficiency inverted semi-transparent planar perovskite solar cells in substrate configuration," *Nature Energy*, vol. 2, no. 1, p. 16190, 2016.

[204] Y. Deng, C. H. V. Brackle, X. Dai, J. Zhao, B. Chen, and J. Huang, "Tailoring solvent coordination for high-speed, room-temperature blading of perovskite photovoltaic films," *Science Advances*, vol. 5, no. 12, p. eaax7537, 2019.

[205] T. Moot, J. B. Patel, G. McAndrews, E. J. Wolf, D. Morales, I. E. Gould, B. A. Rosales, C. C. Boyd, L. M. Wheeler, P. A. Parilla, S. W. Johnston, L. T. Schelhas, M. D. McGehee, and J. M. Luther, "Temperature coefficients of perovskite photovoltaics for energy yield calculations," *ACS Energy Letters*, vol. 6, no. 5, pp. 2038–2047, 2021.

[206] L. K. Ono, S. R. Raga, S. Wang, Y. Kato, and Y. Qi, "Temperature-dependent hysteresis effects in perovskite-based solar cells," *J. Mater. Chem. A*, vol. 3, pp. 9074–9080, 2015.

[207] H. Rostamzadeh and H. Montazeri, "On the role of thermo-electro-ionic dynamics in hysteresis and transient performance of perovskite solar cells," *Energy Environ. Sci.*, vol. 19, pp. 1250–1265, 2026.

[208] I. M. Peters, H. Liu, T. Reindl, and T. Buonassisi, "Global prediction of photovoltaic field performance differences using open-source satellite data," *Joule*, vol. 2, no. 2, pp. 307–322, 2018.

TURUN
YLIOPISTO
UNIVERSITY
OF TURKU

Painosalama, Turku, Finland 2026

ISBN 978-952-02-0699-4 (PRINT)
ISBN 978-952-02-0700-7 (PDF)
ISSN 2736-9390 (Painettu/Print)
ISSN 2736-9684 (Sähköinen/Online)